Dissertation
submitted to the
Combined Faculty of Mathematics, Engineering and Natural Sciences
of Heidelberg University, Germany
for the degree of
Doctor of Natural Sciences

Put forward by
M.Sc. Michael Karl Rosner
born in Marktredwitz
Oral examination: 24.10.2024

Electronic energy level determination in the 4f-subshell in highly charged lead and the 5d-subshell in highly charged bismuth by atomic structure calculation-assisted optical spectroscopy

Referees: Apl. Prof. Dr. José R. Crespo López-Urrutia
Priv. Doz. Dr. Wolfgang Quint

Dedication

To the extensive curiosity that proved a loyal companion and steady impetus. May we preserve you by inspiring future generations, for the quest for knowledge will surely never end.

"Probably the last sound heard before the Universe folded up like a paper hat would be someone saying, 'What happens if I do this?"'

—*Terry Pratchett*

Electronic energy level determination in the 4f-subshell in highly charged lead and the 5d-subshell in highly charged bismuth by atomic structure calculation-assisted optical spectroscopy

In semi-filled subshells of highly charged ions (HCIs), intra-configuration fine-structure transitions shift from the infrared to the optical range. The electronic states in nd and nf subshells cover a variety of different total angular momenta, potentially featuring higher-order multipole clock transitions.

By utilising laser-induced ablation inside an electron beam ion trap (EBIT), restrictions on elements applicable as HCIs for optical spectroscopy have been lifted. Optical spectra of Pb^{21+} to Pb^{33+} and Bi^{9+} to Bi^{14+} were recorded with high resolution thanks to a newly developed algorithm to correct for thermal drifts. These were compared to dedicated atomic structure calculations. Information about the level structure of $4f^3$ to $5s^24f^{13}$ in lead and $5d^1$ to $5d^6$ in bismuth were inferred.

The presented level structure determinations are valuable as a benchmark for atomic structure calculations and are an essential step towards vacuum-ultraviolet spectroscopy in the search for higher-order optical clock transitions in the examined ions.

Bestimmung elektronischer Energieniveaus der 4f-Unterschale hochgeladenen Bleis und der 5d-Unterschale hoch geladenen Bismuts mit optischer Spektroskopie unterstützt durch Atomstrukturberechnungen

In halbgefüllten Unterschalen hochgeladener Ionen (HCI) verschieben sich Feinstrukturübergänge der selben Konfiguration vom infraroten in den optische Bereich. Die elektronischen Zustände der nd und nf Unterschale decken eine Vielzahl veschiedener Gesamtdrehimpulse ab, möglicherweise mit Uhrenübergängen höherer Multipolordnung.

Durch laserinduzierte Ablation innerhalb einer Elektronenstrahlionenfalle (EBIT) wurden Beschränkungen auf die Elemente, die als HCI für optische Spektroskopie zur Verfügung stehen, aufgehoben. Optische Spektren von Pb^{21+} bis Pb^{33+} sowie Bi^{9+} bis Bi^{14+} wurden, dank eines neu entwickelten Algorithmus zur Korrektur thermischer Verschiebungen, mit hoher Auflösung aufgenommen und mit dafür vorgesehen Atomstrukturberechnungen verglichen. Informationen über die Levelstruktur von $4f^3$ bis $5s^2\ 4f^{13}$ in Blei, sowie $5d^1$ bis $5d^6$ in Bismuth, wurden gewonnen.

Die vorgelegten Levelstrukturbestimmungen sind nützliche Vergleichsgrößen für Atomstrukturberechnungen und sinde in wichtiger Schritt in Richtung Spektroskopie der Vakuumultraviolettstrahlung der untersuchten Ionen auf der Suche nach optischen Uhrenübergängen.

Contents

Acronyms

BESSY

Berlin electron storage ring society for synchrotron radiation.

BSM

Physics Beyond the Standard Model.

CAS RN

chemical abstracts service registry number.

CCD

charge-coupled device.

CE

collisional excitation.

CHX

charge exchange.

CI

configuration interaction.

CRM

collisonal radiative model.

DE

deexcitation.

DT

drift tube.

EBIT

electron beam ion trap.

EII

electron impact ionisation.

ER

electronic recombination.

`FAC`

flexible atomic code.

FLASH

free electron laser in Hamburg.

FLASH-EBIT

free electron laser Hamburg EBIT.

FS

fine structure.

***g*-factor**

Landé g-factor.

GI

gaseous injection.

HC-EBIT

Heidelberg compact EBIT.

HCI

highly charged ion.

HD-EBIT

Heidelberg EBIT.

HFS

hyperfine structure.

LI

laser injection.

MBPT

many-body perturbation theory.

NIST data

National Institute of Standards and Technologies standard reference data.

NNMF

non-negative matrix factorisation.

PLA

polylactic acid.

QLS

quantum logic spectroscopy.

QPN

quantum projection noise.

RR

radiative recombination.

SHV

safe high voltage.

SM

Standard Model of physics.

SNR

signal-to-noise ratio.

UHV

ultra-high vacuum.

UPS

uninterruptible power supply.

UV

ultraviolet.

VUV

vacuum ultraviolet.

XUV

extreme ultraviolet.

XUV-EBIT

extreme ultraviolet EBIT.

Symbols

$A \approx B$

A is approximately B.

$A \sim 10^B$

A is of the order of magnitude B.

$A \propto B$

A is proportional to B.

$*$

placeholder.

$*_{\mathrm{i}}$

$*$ value of the initial state.

$*_{\mathrm{A}}$

$*$ value calculated by AMBiT.

$*_{\mathrm{f}}$

$*$ value of the final state.

$*_{\mathrm{F}}$

$*$ value calculated by `FAC`.

φ_*

Potential of electrode $*$,
$\varphi = 0$ at laboratory ground unless stated otherwise.

E_{Beam}

Electron beam energy considering voltages and space charge effect.

E_e

Kinetic energy of an electron, commonly equal to E_Beam.

E_ion

Ionisation energy of an ion or atom.

λ

Wavelength.

Q

Charge of an ion.

q

Unitless charge state of an ion.

t_ac

Aquisition time of a spectral image.

U_acc

Acceleration voltage, typically between cathode and central drift tube.

U_SC

Space charge potential U_SC, caused by electrons $U_\mathrm{SC,e}$ and ions $U_\mathrm{SC,i}$.

g

Landé g-factor.

μ_B

Bohr magneton.

R_y

Rydberg energy.

J

Total angular momentum quantum number.

m

Magnetic quantum number.

n

Principal quantum number.

Chapter 1

Introduction

"Never measure anything but frequency!"

—*Arthur Schawlow* [1]

The advancement of fundamental physics relies more and more on highly accurate measurements. While increasing it certainly pushes the boundaries further, refining the methods in other ways may prove even more beneficial. In the present case, the adaptation of highly charged ion (HCI) into optical clocks is examined, to increase the *sensitivity* of "new physics" effects, increasing the significance of results for the same experimental measurement accuracy.

1.1 Physics beyond the Standard Model

The majority of particles and most of their interactions detected are readily described by the Standard Model of physics (SM). Since the Higgs boson's existence has been confirmed, the model is complete in itself and generally accepted. While it is exceptionally useful in its scope, examples of effects and properties not included in the SM exist: Gravity, one of the four fundamental forces, is not represented, as a conclusive link between quantum mechanics and general relativity has not yet been found. While the graviton is postulated as a mediating particle, the actual nature of quantum gravity remains unknown. Dark matter and dark energy, both initially predicted to

explain astrophysical phenomena, are not included in any form, nor is another explanation of said phenomena [2]. An example is a possible variation of the fine structure constant αor the proton-to-electron mass ration [3–8]. The discovered existence and oscillation of neutrino masses are incompatible with the SM as well [9–11].

For the SM to perform as well as it does, all of these effects have to be extremely minute on the particle scale. For example, the gravitational interaction between two protons in a nucleus is 10^{-36} times weaker than their electromagnetic repulsion. Therefore, initial observations typically occur at astrophysical scales, where sensitivity is enhanced by mere size. Unfortunately, many details about our universe, even those in the closer vicinity of our planet, are still unknown, leading to major uncertainties in the nature and reliability of those predictions. Accordingly, the necessity of recreating those phenomena in a laboratory environment emerges. Due to the aforementioned minute nature, this needs to be done in high-precision experiments. One of the highest precision attainable today is reached by studying optical clock transitions.

1.2 Optical clocks

Since the invention of the first accurate pendulum clock in the 17th century, frequency and, therefore, time is the quantity that can be measured most accurately [1]. In the second half of the 20^{th} century, atomic clocks rapidly advanced, with caesium clocks improving from a relative uncertainty of 10^{-10} to about 5×10^{-15} by the beginning of the new century [12–14]. The innovation of caesium fountain clocks - essentially removing the first-order Doppler effect by laser cooling the atoms instead of using a thermal beam - reduced uncertainties to 10^{-16} [15–17]. The accuracy of microwave fountain clocks is limited by quantum projection noise (QPN) [18]. The fractional instability of a clock locked to an atomic transition can be quantified by the Allan deviation

$$\sigma_y(\tau) \propto \frac{\Delta\nu}{\pi\nu_0}\sqrt{\frac{T}{\tau N}} \tag{1.1}$$

for a transition of frequency ν_0 and linewidth $\Delta\nu$, averaging time τ, number of interrogated atoms N and interrogation duration T [19]. In many modern set-ups, the interrogation time is a practical, not a principal, limitation, so the Allen deviation is given time-dependent as x $/\sqrt{\tau}$, like in refs. [20–22]. It can be lowered by increasing the interrogated frequency ν_0, leading to the rise of optical clocks [23, 24]. [25]

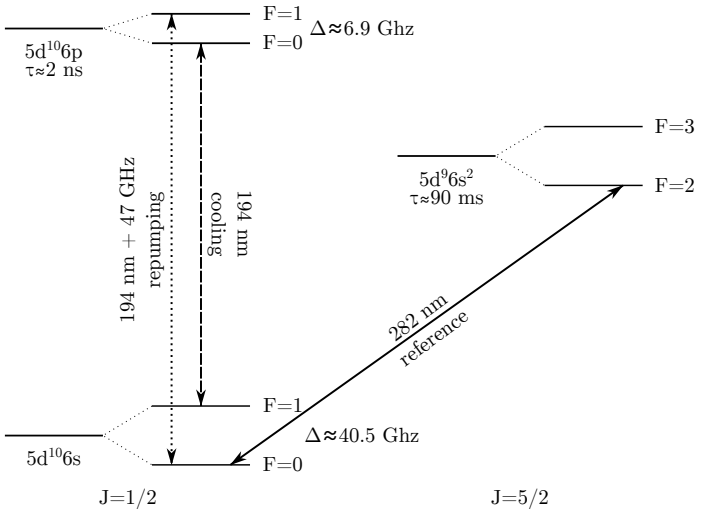

Figure 1.1: Partial level scheme of $^{199}Hg^{+}$. The employed cooling (dashed), repumping (dotted), and clock (solid) lasers are shown as double-sided arrows between their resonant levels. The hyperfine splitting shown is exaggerated for visibility and not to scale. J is the total angular momentum of the core, and F is the total angular momentum of the ion. τ is the lifetime of the respective state, Δ the hyperfine splitting. Recreated with data from refs. [26, 27].

Single ion clock To utilise the low QPN of optical clock transitions, all other sources of uncertainty need to be minimised as well. One possibility is to isolate a single ion in a radio-frequency trap, where it is laser-cooled and emits resonant fluorescence radiation [28]. Cooling transitions require fast transitions - i.e. short lifetimes of the upper state - while natural line broadening demands long lifetimes for an accurate clock transitions.

Suitable ions feature at least two transitions, e.g. $199\,Hg^{+}$ features the 194 nm, 2 ns fast cooling transition and the 282 nm, 90 ms long-lived clock transition, as displayed in fig. 1.1. The additional 194 nm, 47 GHz detuned repumping laser is necessary due to the hyperfine splitting that gets populated off resonantly. Choosing an isotope with zero nuclear spin is not beneficial, as they lack magnetic field insensitive transitions employed in this scheme, which are less susceptible to external influences. [26]

The general measurement procedure is as follows: The ion is cooled near the Doppler limit, in this case to about 1.9 mK. By measuring the fluorescence light, the electronic state of the ion can be deducted: Absorption of a 282 nm photon transfers the ion to a metastable $5d^{10}6s^2$ state, preventing the 194 nm fluorescence. Accordingly, this is called a *dark state* of the ion. This technique, called "electron shelving", and a quantum efficiency of $\approx 5\,\%$

at 194 nm combined ensures the detection of (nearly) every 282 nm photon absorption event. A relative uncertainty of 1.5×10^{-15} was achieved this way. [26]

Eventually reaching a fractional uncertainty of 7.2×10^{-17}, this single-ion mercury clock surpassed the best caesium fountain clocks by an order of magnitude [29]. As this technique merely depends on a suitable level structure, single ion clocks with different ion species emerged, including $^{40}Ca^{+}$ [30], $^{171}Yb^{+}$ [31], $^{88}Sr^{+}$ [32] and sympathetically cooled $^{115}In^{+}$ [33]. With ytterbium $^{171}Yb^{+}$, a fractional frequency instability of $5 \times 10^{-15}/\sqrt{\tau}$ and a total systematic uncertainty of 3.2×10^{-18} could be achieved [20].

Optical lattice atomic clock A so-called *optical lattice* is a different way to achieve a cold, isolated environment. Instead of the frequency trap mentioned above, which can only trap charged particles, an optical lattice stores neutral atoms, enabling different optical clock candidates. The optical lattice emerges by the interference of two counter-propagating laser beams. In the maxima of the resulting standing wave, neutral particles are trapped by the Stark shift [34]. The atoms can be confined in the Lamb-Dicke regime, allowing for Doppler-free spectroscopy [35]. [36]

Interrogation of millions of strontium atoms trapped this way achieves low Allan deviations $\sigma_y(\tau) \approx 10^{-18}$ for interaction times as low as $\tau = 1\,\mathrm{s}$ [36]. Optical lattice clocks using ^{171}Yb reached a stability of $3.2 \times 10^{-16}\ /\sqrt{\tau}$ [37]. Absolute uncertainties down to 3×10^{-17} have been achieved this way using ^{87}Sr [38]. Extension of the strontium lattice into three dimensions allowed an improvement of the fractional stability to $3.1 \times 10^{-17}/\sqrt{\tau}$ and a systematic uncertainty of 3.5×10^{-19} [21].

Quantum logic spectroscopy With the techniques as mentioned earlier, the range of available systems is fairly limited: Optical lattices only work for neutral atoms, and single-ion clocks require a suitable combination of a fast cooling-and-readout transition and a long-lived high-precision clock transition. Fortunately, quantum mechanics allows for splitting these two transitions between two different ions coupled by their joint vibrational state. This is used in a technique known as *quantum logic spectroscopy (QLS)*. The ion with the fast transition, used for cooling and read-out, is called the logic ion, while the other with the precise transition is called the spectroscopy ion. This is achieved by preparing them in the same radio frequency trap, where they thermalise due to their coulomb interaction, and cooling them via the logic ion. The system is cooled down to its motional ground state by resolved sideband cooling, effectively forming a two-ion quantum computer [39].

The following explanation of this "quantum computer" is adapted from ref. [40]. Treating the transition in logic and spectroscopy ion as respective two-level systems, its total wave function Ψ can be defined by multiplying the following three factors:

i $|\downarrow\rangle_{\mathrm{S}}$ and $|\uparrow\rangle_{\mathrm{S}}$ for the spectroscopy ion

ii $|\downarrow\rangle_{\mathrm{L}}$ and $|\uparrow\rangle_{\mathrm{L}}$ for the logic ion

iii $|n\rangle_{\mathrm{m}}$ for the motional state with $n \in \mathbb{N}$ quanta

The initial state prepared by cooling is the ground state

$$\Psi_0 = |\downarrow\rangle_{\mathrm{S}} |\downarrow\rangle_{\mathrm{L}} |0\rangle_{\mathrm{m}} . \tag{1.2}$$

Coherent radiation near the transition of the spectroscopy ion changes its state

$$|\downarrow\rangle_{\mathrm{S}} \rightarrow \alpha |\downarrow\rangle_{\mathrm{S}} + \beta |\uparrow\rangle_{\mathrm{S}} , \tag{1.3}$$

where $|\alpha|^2 + |\beta|^2 = 1$, with the factors α and β depending on how far off resonance the radiation is. The combined state thus changes to

$$\Psi_0 \rightarrow \Psi_1 = (\alpha |\downarrow\rangle_{\mathrm{S}} + \beta |\uparrow\rangle_{\mathrm{S}}) |\downarrow\rangle_{\mathrm{L}} |0\rangle_{\mathrm{m}} \tag{1.4}$$

$$= (\alpha |\downarrow\rangle_{\mathrm{S}} |0\rangle_{\mathrm{m}} + \beta |\uparrow\rangle_{\mathrm{S}} |0\rangle_{\mathrm{m}}) |\downarrow\rangle_{\mathrm{L}} . \tag{1.5}$$

A red side-banded π pulse translates any upper spectroscopy state into a motional state $|\uparrow\rangle_{\mathrm{S}} |0\rangle_{\mathrm{m}} \rightarrow |\downarrow\rangle_{\mathrm{S}} |1\rangle_{\mathrm{m}}$, changing the system into:

$$\Psi_1 \rightarrow \Psi_2 = (\alpha |\downarrow\rangle_{\mathrm{S}} |0\rangle_{\mathrm{m}} + \beta |\downarrow\rangle_{\mathrm{S}} |1\rangle_{\mathrm{m}}) |\downarrow\rangle_{\mathrm{L}} \tag{1.6}$$

$$= |\downarrow\rangle_{\mathrm{S}} |\downarrow\rangle_{\mathrm{L}} (\alpha |0\rangle_{\mathrm{m}} + \beta |1\rangle_{\mathrm{m}}) , \tag{1.7}$$

where the information about the excitation of the spectroscopy transition has been moved to the joint motional state of both ions. The red side-banded $\pi-$pulse tries to drive the $|\downarrow\rangle_{\mathrm{S}} |0\rangle_{\mathrm{m}} \rightarrow |\uparrow\rangle_{\mathrm{S}} |-1\rangle_{\mathrm{m}}$, transition, which ends up in the non-existent $|-1\rangle_{\mathrm{m}}$ state and therefore doesn't take place, leaving $|\downarrow\rangle_{\mathrm{S}} |0\rangle_{\mathrm{m}}$ unaffected. An additional red side-banded π pulse, now on the logic ion, results in:

$$\Psi_2 \rightarrow \Psi_{\mathrm{final}} = |\downarrow\rangle_{\mathrm{S}} (\alpha |\downarrow\rangle_{\mathrm{L}} + \beta |\uparrow\rangle_{\mathrm{L}}) |0\rangle_{\mathrm{m}} \tag{1.8}$$

transporting the quantum information α, β from the spectroscopy ion into the logic ion, where it can be detected by fluorescence of the cooling transition.

A quantum logic clock based on an $^{27}Al^{+}$ ion reached a systematic uncertainty of 9.4×10^{-19} with a frequency stability of $1.2 \times 10^{-15}/\sqrt{\tau}$ [22]. The

application is possible for diverse types of ions, like molecular ions [41] and HCIs [42]. Clocks featuring HCIs are presented in more detail in section 1.4.

1.3 Clock comparisons

Typically, optical clocks are utilised by comparing them to another frequency standard, most notably Caesium and Rubidium clocks or hydrogen masers, or by comparing different optical clocks. The comparison to microwave standards became immensely simpler and more accurate by the invention of the frequency comb [43, 44]. This way, accepted theories can be validated thoroughly, and new physics, e.g., introduced in section 1.1, can be constrained or corroborated. Independence of a specific unit system is beneficial, leading to a preference to probe dimensionless quantities, like the fine-structure constant α or the proton-to-electron mass ratio $\frac{m_p}{m_e}$. Furthermore, additional assumptions of underlying properties, like unknown nuclear characteristics, are preferably avoided or cancelled out. In the following, the use of optical clocks to evaluate will be discussed in more detail.

Temporal variation of the Fine Structure Constant α The first model-independent way to limit the temporal variation of the fine structure constant α has been achieved by independently and repeatedly comparing $^{171}Yb^+$ and $^{199}Hg^+$ single ion clocks to caesium fountain clocks over the course of a few years. In order to do so, ref. [45] expresses measured electronic transition frequencies f as

$$f = \mathrm{Ry}\, C F(\alpha) \tag{1.9}$$

split into the Rydberg constant Ry, a numerical constant C, depending on the quantum numbers of the transition, and a dimensionless function $F(\alpha)$, describing relativistic level shifts depending on α. As the same transition is probed, the quantum numbers and, therefore, C can be assumed to be constant, allowing the relative temporal derivative of the frequency to be written as

$$\frac{\partial \ln f}{\partial t} = \frac{\partial \ln \mathrm{Ry}}{\partial t} + \frac{\partial \ln F}{\partial \ln \alpha}\frac{\partial \ln \alpha}{\partial t}. \tag{1.10}$$

With the comparison of different transitions to the ^{133}Cs hyperfine splitting of a fountain clock, the variation $\frac{\partial \ln \mathrm{Ry}}{\partial t}$ is common to all comparisons. By contrast, $\frac{\partial \ln F}{\partial \ln \alpha}\frac{\partial \ln \alpha}{\partial t}$ is directly linked to the specific optical clock used. It is separated in the drift rate $\frac{\partial \ln \alpha}{\partial t}$ that is ultimately of interest and the individ-

ual transitions sensitivity factor

$$A := \frac{\partial \ln F}{\partial \ln \alpha}. \tag{1.11}$$

A plot of frequency variations $\frac{\partial \ln f}{\partial t}$ of different transitions over their respective sensitivity A is thus expected to yield a straight line with the intercept $\frac{\partial \ln \mathrm{Ry}}{\partial t}$ and the slope $\frac{\partial \ln \alpha}{\partial t}$. Results consistent with zero, and therefore, upper bounds for the time variation of α and Ry have been found [45]:

$$\frac{\partial \ln \mathrm{Ry}}{\partial t} = -0.3(20) \times 10^{-15}\,\mathrm{yr}^{-1} \tag{1.12}$$

$$\frac{\partial \ln \alpha}{\partial t} = -1.6(32) \times 10^{-15}\,\mathrm{yr}^{-1} \tag{1.13}$$

As discussed in section 1.2, the Caesium standard is less accurate than the modern optical clocks and limits those results. Thus, improvement came from the direct comparison of optical clocks, first realised by comparing $^{27}\mathrm{Al}^+$ and $^{199}\mathrm{Hg}^+$ [46]:

$$\frac{\partial \ln \alpha}{\partial t} = -1.6(23) \times 10^{-17}\,\mathrm{yr}^{-1}. \tag{1.14}$$

Constraints on dark matter While these results strictly limit a possible long-term drift of α, those comparisons are insensitive to changes at a short time scale. Such changes are expected to emerge from certain types of dark matter our earth traverses on its way through the universe. This way, measurements can be used to give constraints on dark matter candidates. To do so, the anomalies are detected within a single optical clock: The relativistic atomic transitions scale with $\propto \alpha^2$, while a laser cavity, e.g. of the reference laser used, scales with $\propto \alpha$ [47]. Multiple optical clocks around the globe are used for that measurement. They do not need to be linked directly by optical fibres in real time; merely, their locally recorded measurements need to be accurate to about 1 ms to correlate possible dark matte events retroactively [48].

Also, the temporal variation of the proton-to-electron mass ratio $\mu = m_\mathrm{p} m_\mathrm{e}^{-1}$ can be constrained by optical clocks. A comparison of an optical Yb^+ and a Cs atomic clock gave that limit as

$$\frac{\dot{\mu}}{\mu} = -0.5(16) \times 10^{-16}\,\mathrm{yr}^{-1}, \tag{1.15}$$

consistent with zero [49].

1.4 Highly charged ion as optical clock

To push the limits for temporal variations of fundamental constants even further, spectroscopy of HCI has been proposed. Their use in QLS schemes is well established [42, 50, 51]. Due to the nature of HCI, their electronic structure is less sensitive to external influences. Narrow optical ground state transitions, as needed for QLS, are proposed for several of them. A multitude of effects leads to suitable transitions, leading to enhanced sensitivity to the discussed Physics Beyond the Standard Model (BSM) in some of them. A few are even among the most sensitive ones known to date. [52]

Another application of HCI is the so-called *electronic bridge excitation* proposed in thorium ^{299}Th. Measurements of internal conversion electrons result in an energy $E_m = 8.28(17)\,\mathrm{eV}$ for the nuclear-excited state ^{299m}Th [53]. Using this transition as a frequency standard, a "nuclear clock" could be built. A possibility to excite this transition is via a matching electronic transition in the shell. Especially the 4f-subshell is of interest due to the availability of diverse electronic transitions in the fine structure of the ground state configuration. In particular, the Cs-like Thorium Th^{35+} is promising in this regard. Electronic energy level determination through optical and vacuum ultraviolet (VUV) spectroscopy in combination with extensive analysis based on atomic structure calculation is called for to employ the proposed measurement scheme successfully. [54]

1.5 Thesis outline

The application of QLS depends on the knowledge of narrow ground state transitions [40, 55]. It is necessary to investigate the level structure and transitions of candidate ions to find species suitable for QLS. Typically, initial suggestions are made by advanced atomic structure calculations [52, 56–58]. Then, spectroscopy on the ions in question is performed to refine the level structure and determine the transition energy more precisely [59, 60].

The work done for this thesis aims to support this process in two ways: Firstly, the presented advancements in experimental techniques directly pave the way for the spectroscopy of previously inaccessible elements. Through the combination of superconducting electron beam ion traps (EBITs), featuring strong magnetic fields, with a laser injection source, virtually any element of interest becomes available for the high-precision spectroscopy presented in this work. They include but are not limited to the proposed ions of interest, Th^{35+} [54] and Cf^{16+} [61]. Up to this point, the absence of suitable volatile compounds, essential for the previous setup, prevented experiments with

these elements.

Secondly, it delivers a comprehensive overview of the f- and d-subshells for elements with high atomic numbers. In lead, atomic number $Z_{\mathrm{Pb}} = 82$, the 4f-subshell and in bismuth, $Z_{\mathrm{Bi}} = 83$, the 5d-subshell is analysed. The two resulting spectral series of heavy, isonuclear, moderately charged HCIs exceed previous studies of such ions in resolution and extent. As a consequence, they form a benchmark reference for atomic structure calculation codes catered for these types of ions, improving future predictions.

Additionally, the measurements conducted for this work bear some scientific value in itself. The chosen elements and ionisation stages deliver many ground-state transitions. Due to its variety of isotopes, the ground state transitions in lead may be advantageous in the application of King-plot analysis [58, 60, 62–65]. Furthermore, clock ions based on the candidates found in this work may find meaningful applications, as they may be more feasible than intra-configuration level crossing transitions that are currently preferred for their large dependency on α.

Chapter 2

Underlying physical principles

"It is by mathematical formulation of its observations and measurements that a science is able to form mathematically expressed hypotheses, and it is through its hypotheses that a natural science is able to make predictions"

—*David Greenwood* [66]

A comprehensive introduction to the underlying atomic physics processes that lay the foundation for the calculations presented in later chapters goes beyond the scope of this work but is readily available in numerous textbooks. Instead, derived equations and correlations corresponding to the experiment are presented in the following chapter. Hence, the focus lies on highly charged ions, their properties, production, storage, interactions with an electron beam, their electronic and transition properties and the means used to calculate those *ab initio*. The physics underlying the element delivery methods in use are also presented briefly.

2.1 Highly charged ions

The definition of the term highly charged ion (HCI) is rather vague. While there is consensus about most cases – an ion of charge $Q \in \{e, 2e\}$ is certainly not highly charged, while with $Q \geq 10e$ it is – a clear division remains absent. An idea was to draw the line at half the nuclear charge Z, i.e. $Z/2$. However, that excludes many, if not most, HCI currently of interest. A premier example is Fe^{13+}, which has strong astrophysical implications and was the subject

of a prolonged dispute between theory and different experiments [67, 68]. Therefore, though not as precise, a more inclusive and technical definition will underline this work: *An ion is considered highly charged once it reaches a charge state unobtainable by traditional means due to a high ionisation energy* $E_{\mathrm{ion}} \gtrsim 50\,\mathrm{eV}$. To rephrase this, if an effect specialised to produce HCI is needed to produce an ion, it is considered highly charged for the scope of this work.

The particular properties of HCI will be presented in section 2.1.1 The effects utilised to generate them are presented in section 2.1.2. The description of HCIs interactions with their surroundings in section 2.1.5 concludes the discussion of their fundamental characteristics.

2.1.1 Ion properties

In the most rudimentary approximation, any atom or HCI with nuclear charge Z and electron number N_{e} is treated as a hydrogen atom. One electron is treated as 'free' to change level, while the others are in a 'frozen core'. This 'frozen core' shields the nuclear charge Z, leaving an effective nuclear charge

$$Z_{\mathrm{eff}} = Z - N_{\mathrm{e}} + 1 \tag{2.1}$$

to be 'seen' by the 'free' electron.

While modern atomic calculations are more precise than this, ball-park considerations can be based on this model. Since this work is concerned with optical spectroscopy, a focus is placed on wavelengths $\lambda \sim 10^2\,\mathrm{nm}$. First of all, the main energy levels E_n, with the principal quantum number n, depend quadratically on Z and thus scale with Z_{eff}^2. This increases the energy of transitions between different n, elevating the spectrum from the optical range in hydrogen to the X-ray range for most HCI. On the other hand, fine structure (FS) and hyperfine structure (HFS) contributions are affected even more, $\Delta E_{\mathrm{FS}} \propto Z_{\mathrm{eff}}^4$ and $\Delta E_{\mathrm{HFS}} \propto Z_{\mathrm{eff}}^3$. With increasing Z_{eff}, this first lifts the radio frequency FS splitting and later the microwave HFS splitting into then optical. For even higher Z_{eff}, they consequently continue towards vacuum ultraviolet (VUV) and soft X-ray. Additionally, at some point, the rising ΔE_{FS} nearly cancels out the lower rising level separation E_n, resulting in optical transitions, an effect coined *level crossing* [56, 69]. The different nature of these optical transitions leads to a varied dependence on fundamental physical properties, e.g. the FS constant α. Optical spectroscopy on different HCI is thus of particular interest for fundamental physics [52]. Furthermore, the electron's proximity to the nucleus featured in HCI and the associated strong fields lead to a reduced influence of the environment.

2.1.2 Generation principles

Generating HCIs evidently requires many subsequent ionisation steps. Therefore, methods insensitive to the detailed electronic structure and ionisation energies are vital. This mainly includes impact ionisation, with electrons or atoms, and electron-cyclotron-resonance ionisation. For this work, electron beam ion traps (EBITs) are used, where sequential electron impact ionisation (EII) is leveraged.

Specifically, an electron beam is generated by a hot cathode, supplying the required Fermi energy thermally and thus freeing electrons that are then accelerated by a static potential difference. A static, inhomogeneous magnetic field is traversed by the electron beam. It is nearly 0 at both ends but very strong in the centre. This so-called magnetic bottle compresses the electron beam, vastly increasing the electron density.

Thus, any matter present in this reason strongly interacts with the electron beam. The high electron beam energies $E_{\mathrm{beam}} \sim 10^4\,\mathrm{eV}$ ensure dissociation of molecules and ionisation of atoms. Subsequently, to analyse the inner workings of an EBIT, the focus lies on the interaction of the electron beam with ions, as discussed in the following section.

2.1.3 Storage

According to Earnshaw's theorem, point charges cannot be stored in an electrostatic equilibrium. This restriction is commonly circumvented by using alternating fields, such as in a radio-frequency trap, or by superimposing electric and magnetic fields, such as in Penning traps. A less common solution is the utilisation of an electrostatic space charge of the opposite sign as a source term. This can be achieved, e.g., by a cylindrical electron beam, confining the ions electrostatically in two spatial directions. The third direction can be covered repulsively by end caps, e.g., as a pair of ring electrodes. As a consequence, the particles maintaining the space charge and the trapped ions interact. While this is often contradictory to the purposes of trapping to isolate particles, the traps used for this work leverage those interactions, maintaining the desired particles by carefully tuning the trap parameters.

2.1.4 Electron beam properties

Many interactions occurring in the trap depend on the energy of the electron beam E_{beam}, specifically at the interaction region inside the central drift tube (DT). The main contribution stems from the acceleration voltage U_{acc}

between the cathode potential φ_{cathode} and this drift tube $\varphi_{\text{DTcentral}}$:

$$U_{\text{acc}} = \varphi_{\text{cathode}} - \varphi_{\text{DTcentral}}. \tag{2.2}$$

As stated above, the electron beam features a substantial negative space charge potential $\varphi_{\text{SC,e}} < 0$. Additionally, the trapped ions form a positive space charge potential $\varphi_{\text{SC,i}} > 0$. Since the ions have to be trapped by the total space charge potential, the negative space charge prevails,

$$\left|\varphi_{\text{SC,e}}\right| > \left|\varphi_{\text{SC,i}}\right|. \tag{2.3}$$

This gives a total space charge potential of

$$\varphi_{\text{SC}} = \varphi_{\text{SC,e}} + \varphi_{\text{SC,i}} < 0. \tag{2.4}$$

The complete electron beam energy is thereby composed of

$$E_{beam} = \big(U_{\text{acc}} + \varphi_{\text{SC}}\big)e = \big(\varphi_{\text{cathode}} - \varphi_{\text{DTcentral}} + \varphi_{\text{SC,e}} + \varphi_{\text{SC,i}}\big)e \tag{2.5}$$

Unfortunately, the space charges are difficult, if not impossible, to exactly determine. The acceleration potential, on the other hand, can be controlled directly. Therefore, the electron beam energy

$$E_{\text{beam}} < U_{\text{acc}}e. \tag{2.6}$$

is lower than the acceleration potential.

2.1.5 Electronic processes

Since the negative space charge of the electron beam ensures the overlap of ions and electrons, they constantly interact with each other. Furthermore, neutral atoms – from the injection or residual gases – reach the trap as well. Additionally, once excited, electronic processes within the ion also occur. The main electronic processes taking place are

- Electron impact ionisation (EII) – $\mathrm{A}^{\mathrm{q}} + \mathrm{e}^{-} \rightarrow \mathrm{A}^{\mathrm{q}+1} + 2\,\mathrm{e}^{-}$
- Radiative recombination (RR) – $\mathrm{A}^{\mathrm{q}} + \mathrm{e}^{-} \rightarrow \mathrm{A}^{\mathrm{q}-1} + \gamma$
- Electronic recombination (ER) – $\mathrm{A}^{\mathrm{q}} + \mathrm{e}^{-} \rightarrow [\mathrm{A}^{\mathrm{q}-1}]^{*}$
- Charge exchange (CHX) – $\mathrm{A}^{\mathrm{q}} + \mathrm{B} \rightarrow \mathrm{A}^{\mathrm{q}-1} + \mathrm{B}^{+} + \gamma$
- Collisional excitation (CE) – $\mathrm{A}^{\mathrm{q}} + e^{-} \rightarrow [\mathrm{A}^{\mathrm{q}}]^{*} + e^{-}$

- Deexcitation (DE) – $[\mathrm{A}^{\mathrm{q}-1}]^* \rightarrow \mathrm{A}^{\mathrm{q}-1} + \gamma$

where the partaking particles are given as ion A^{q} of charge state $\mathrm{q} = Q/e$, electron e^-, photons γ and atom B^0. Excited electronic states are indicated by $[\quad]^*$

Electron impact ionisation

The ionisation energy E_{ion} of an atom or ion needs to be provided to increase its charge state from q to q + 1. In this case, neutral atoms are treated as ions of charge $Q = 0$. If the energy E_{Beam} of the electrons e^- in the beam surpasses E_{ion}, ionisation may take place:

$$\mathrm{A}^{\mathrm{q}} + \mathrm{e}^- \rightarrow \mathrm{A}^{\mathrm{q}+1} + 2\,\mathrm{e}^-, \qquad E_{\mathrm{ion}} < E_{\mathrm{Beam}} \tag{2.7}$$

The cross-section of this process is given in ref. [70] as:

$$\sigma^{\mathrm{EII}}_{\mathrm{q}\rightarrow\mathrm{q}+1} \approx \sum_{i=1}^{N} a_i q \frac{\ln\left(\mathrm{E_e}/\mathrm{E_{ion}}\right)}{E_{\mathrm{e}} E_{\mathrm{ion}}} \left(1 - b_i \exp\left[-c_i \left(\frac{E_{\mathrm{e}}}{E_{\mathrm{ion}}} - 1\right)\right]\right), \tag{2.8}$$

summing over all N sub-shells i, the removed electron may originate from. The constants a_i, b_i, c_i have to be measured or calculated.

The qualitative dependency of the cross-section dependency of the ratio of electron energy to ionisation energy $E_{\mathrm{Beam}}/E_{\mathrm{ion}}$ is given in ref. [71]: Starting from $\sigma = 0$ at $E_{\mathrm{Beam}} = E_{\mathrm{ion}}$, the cross-section increases, reaching a maximum around $E_{\mathrm{Beam}} \approx 3\,E_{\mathrm{ion}}$. Then it slowly decays, approaching 0 for $E_{\mathrm{Beam}} \rightarrow \infty$, where the electrons are too fast to interact.

Radiative recombination

The ions A^{q} may also recombine with an electron e^- from the beam with the energy E_{beam}, to the ion $\mathrm{A}^{\mathrm{q}-1}$, providing the ionisation energy $E_{\mathrm{i,A^{q-1}}}$. Typically, this excess energy gets radiated by a photon:

$$\mathrm{A}^{\mathrm{q}} + \mathrm{e}^- \rightarrow \mathrm{A}^{\mathrm{q}-1} + \gamma, \quad E_\gamma = E_{\mathrm{Beam}} + E_{\mathrm{i,A^{q-1}}}. \tag{2.9}$$

Ref. [72] gives the cross-section of this process semi-empirically as

$$\sigma^{\mathrm{RR}}_{\mathrm{q}\rightarrow\mathrm{q}-1} = \frac{8\pi}{3\sqrt{3}} \alpha \lambda\!\!\!^{-2}_{\mathrm{C}} \chi \ln\left(1 + \frac{\chi}{2n^2_{0,\mathrm{eff}}}\right),\ \chi = 2Z^2_{\mathrm{eff}} \frac{R_{\mathrm{y}}}{E_{\mathrm{e}}}, \tag{2.10}$$

with the fine structure constant α, the reduced Compton wavelength $\lambda\!\!\!^{-}_{\mathrm{C}}$, an

effective nuclear charge Z_{eff}, the Rydberg energy R_{y} and an effective principal quantum number $n_{0,\text{eff}} = n_0 + 1 - w_0$, depending on the ratio of occupied states w_0 in n_0.

Electronic recombination

If an appropriate electronic transition is available in the recombined ion, the excess energy may stay in the ion instead of radiating of, delivering an excited ion:

$$\mathrm{A}^{\mathrm{q}} + \mathrm{e}^- \rightarrow \left[\mathrm{A}^{\mathrm{q}-1}\right]^*, \quad \Delta E_{\mathrm{A}^{\mathrm{q}-1}} = E_{\mathrm{e}} + E_{\text{ion}}, \tag{2.11}$$

This process only occurs resonantly, not at most electron beam energies. It is thus suppressed in this work: Experiments at fixed beam energy E_{Beam} are chosen to be off resonantly. Measurements with electron beam scans naturally cannot avoid resonance. Since they are absent at most data points, they are indistinguishable from noise in our case, especially due to low energy resolutions, and are treated accordingly. A cross-section consideration is hence omitted here.

Charge exchange

Any neutral atom B reaching the trap may, instead of undergoing EII, transfer an electron to a HCI A^{q}. This is possible due to the difference in ionisation energies between atom $E_{\text{i,B}}$ and resulting ion $E_{\text{i,A}^{\mathrm{q}-1}}$. Any excess energy is radiated by a photon:

$$\mathrm{A}^{\mathrm{q}} + \mathrm{B} \rightarrow \mathrm{A}^{\mathrm{q}-1} + \mathrm{B}^+ + \gamma, \quad E_\gamma = E_{\text{i,A}^{\mathrm{q}-1}} - E_{\text{i,B}}. \tag{2.12}$$

Ref. [73] gives the cross-section

$$\sigma^{\text{CHX}}_{\mathrm{q}\rightarrow\mathrm{q}-1} = \pi a_0^2 \mathrm{q}^2 \left(\frac{R_{\text{y}}}{E_{\text{i,B}}}\right)^2, \tag{2.13}$$

with the Bohr radius a_0 and the Rydberg energy R_{y}. Among positive ions, CHX is suppressed by their coulomb repulsion.

Collisional excitation

Not all electron-ion interactions lead to a change in the charge state. The electron can give the energy ΔE_{e} to the ion, bringing it to an excited state:

$$\mathrm{A}^{\mathrm{q}} + e^- \rightarrow [\mathrm{A}^{\mathrm{q}}]^* + e^-, \quad \Delta E_{\mathrm{A}^{\mathrm{q}}} = \Delta E_{\text{e}}. \tag{2.14}$$

The cross-section for this process is given in ref. [74] as

$$\sigma_{i\to j}^{\mathrm{CD}} = \pi a_0^2 \frac{8\pi f_{\mathrm{ij}}}{\sqrt{3}} \frac{R_{\mathrm{y}}^2}{E_{\mathrm{ij}}^2} \frac{G(E_{\mathrm{e}}/E_{\mathrm{ij}})}{E_{\mathrm{e}}/E_{\mathrm{ij}}}, \tag{2.15}$$

with the transitions oscillator strength f_{ij} and the energy E_{ij} and a fitting function, the so-called *Gaunt factor* $G(x) \sim 1$. It can be approximated by

$$G(x) = 0.349\ln(x) + 0.455x^{-1} + 0.0988. \tag{2.16}$$

Deexcitation

Any excited ion can spontaneously decay to a lower state by emitting a photon

$$\left[\mathrm{A}^{\mathrm{q}-1}\right]^* \to \mathrm{A}^{\mathrm{q}-1} + \gamma, \quad E_\gamma = \Delta E_{\mathrm{A}^{\mathrm{q}-1}} \tag{2.17}$$

or, if it has enough energy, an electron in an auto-ionisation process,

$$\left[\mathrm{A}^{\mathrm{q}-1}\right]^* \to \mathrm{A}^{\mathrm{q}} + e^-, \quad E_{\mathrm{e}} = \Delta E_{\mathrm{A}^{\mathrm{q}-1}} - E_{\mathrm{i,A^q}} > 0. \tag{2.18}$$

For a spontaneous process, a cross-section is not applicable. Instead, branching ratios and atomic state lifetimes govern the dynamics here, depending closely on the electronic structure. Additionally, collision de-excitation may be present.

Charge state distribution

In ref. [75] the major terms contributing to temporal changes in the number of ions N_{q} in charge state q are considered

$$\dot{N}_{\mathrm{q}} = R^{\mathrm{EII}}_{\mathrm{q-1\to q}} - R^{\mathrm{EII}}_{\mathrm{q\to q+1}} + R^{\mathrm{RR}}_{\mathrm{q+1\to q}} - R^{\mathrm{RR}}_{\mathrm{q\to q-1}} + R^{\mathrm{CHX}}_{\mathrm{q+1\to q}} - R^{\mathrm{CHX}}_{\mathrm{q\to q-1}} + R^{\mathrm{INF}}_{\mathrm{q}} - R^{\mathrm{ESC}}_{\mathrm{q}}. \tag{2.19}$$

Additionally to the rates R^{EII}, R^{RR} and R^{CHX} stemming from the aforementioned processes, an injection term $R^{\mathrm{INF}}_{\mathrm{q}}$ and an escape term $R^{\mathrm{ESC}}_{\mathrm{q}}$ have been added. Qualitative simulations based on this model, e.g. done for ref. [76] and confirmed experimentally therein, show the following general behaviour: Starting with an empty trap, the charge states evolve from mainly singly charged to a steady state distribution on a time-scale $t_{\mathrm{filling}} \sim 1\,\mathrm{s}$. At any time, three main charge states coexist simultaneously, with the other states remaining in trace amounts.

2.2 Delivery of elements

The ions of interest need to be delivered into the trap. As discussed in the previous section, once the substance reaches it, the interaction with the electron beam generates the ions. In this work, either an atomic or molecular beam or a laser-induced plasma is used to do so. Thus, the theoretical considerations of those two concepts are given hereafter.

2.2.1 Atomic and molecular beam

To form an atomic or molecular beam, our substance is first brought into a gaseous phase; details are below. As a gas, their thermodynamic behaviour can be readily described by the kinetic theory of gases: Individual particles scatter elastically with each other and the surroundings, travelling undisturbed otherwise. The *mean free path* l_{mfp} is the distance a particle, on average, could cover between two collisions with another particle, e.g., 'free' as in the absence of surroundings. It is given by

$$l_{\mathrm{mfp}} = \frac{k_{\mathrm{B}}T}{\sqrt{2}\sigma p}, \tag{2.20}$$

with the Boltzmann constant k_{B}, the pressure p, the temperature T and the particles cross-section σ.

An important distinction is whether particle-particle or particle-surrounding collisions dominate. To form a beam, we need to have so-called *free molecular flow*, where the free mean path is much larger than the size of our experiments l_{e}:

$$l_{\mathrm{mfp}} \gg l_{\mathrm{e}}.$$

The experiments are typically of the size $l_{\mathrm{e}} \sim 1\,\mathrm{m}$. For typical particle sizes, the mean free path at room temperature for ultra-high vacuum (UHV), with $p < 10^{-7}\,\mathrm{mbar}$, is

$$l_{\mathrm{mfp}} \gtrsim 10^{3}\,\mathrm{m} \gg l_{\mathrm{e}}.$$

Thus, any gaseous particles entering into UHV behave ray-like. Geometric constraints on their movement, e.g., with multiple aperture or narrow tubes, thus ensure the movement of multiple particles in the same direction, forming a beam. The first geometric constraints may separate a higher pressure area A from the UHV region B, as free molecular flow is only necessary once the beam forms.

Gaseous sources

The simplest way to supply such a beam is with a gaseous source. The limitation here is to maintain the vacuum in B: The inflow into A has to be regulated to control the strength of the beam. Otherwise, divergent portions of the beam that are backscattered into B instead of staying in the beam may increase the pressure in B, preventing free molecular flow. Additionally, the control of particle influx is beneficial experimentally. Gas-flow regulation with a suitable valve is sufficient to do so.

Evaporation and Sublimation

Not all matter used for this injection method need to be gaseous at standard temperature and pressure. Instead, they have to become gaseous under conditions in A. In phase diagrams, the gas phase is in the low-pressure, high-temperature corner. That means we can inject all matter as a beam that is gaseous at the lowest achievable pressure and highest achievable temperature in our trap.

There are three different phase transition pathways for becoming gaseous:

- Evaporation, a liquid sample changing to the gaseous phase
- Sublimation, a solid sample changing into the gaseous phase
- Melting of a solid sample into the liquid phase, with subsequent evaporation

It is important to keep those effects in mind for technical reasons, e.g. the handling of samples. Maintaining a very low pressure *before* heating generally prevents the melting by ensuring sublimation.

Metal-organic compounds

Since temperature and pressure set limits on the properties of the injected matter, it is important to choose the correct chemical compounds for injection. As most elements are metals, an important class of compounds in this context are *metal-organic compounds*. Here, the desired metal, or semimetal, element is bound with various hydrocarbons. While they are chosen, as many are volatile, there are several caveats. Firstly, many are highly toxic, requiring additional care during handling and posing limitations on the experimental setup. Secondly, they often feature a high reactivity, requiring the handling under a protective atmosphere to prevent sample corrosion. Thirdly, they might be susceptible to thermal decomposition, requiring extra care, especially when heated to aid the transition into the gaseous phase.

2.2.2 Injection by laser ablation

Laser ablation can be utilised instead to overcome the limitations of gaseous injection. The sample is prepared in a solid state, from which a laser plasma is produced. A focused, pulsed laser beam rapidly increases the temperature on a small spot on the target, leading to evaporation or sublimation, a process called *ablation* The resulting ablation plume accrues in the laser's pathway, further absorbing it to form a highly opaque plasma, taking in the remaining pulse energy. This effect depends on the laser pulse length and power density. As a result, increasing the pulse energy does not necessarily yield more ions – an additional defocusing may be required.

2.3 Electronic transition properties

2.3.1 Quantum numbers

To completely describe the energy levels of a hydrogen-like atom, i.e. with only a single electron, four quantum numbers suffice:

- principal quantum number $n \in \mathbb{N}$
- azimuthal quantum number $l \in \mathbb{N}_0, l < n$
- magnetic quantum number $m \in \mathbb{Z}, |m| \leq l$
- spin quantum number $s \in \left\{\frac{1}{2}, -\frac{1}{2}\right\}$

For many electron systems, the angular momenta l and s of the individual electrons are less descriptive, as they do not behave independently but couple to each other. The nature of the coupling changes with the number of electrons. Until about thirty electrons, the so-called *L-S-coupling* dominates. The electrons' individual orbital angular momenta couple to a mutual orbital angular momentum $L = \sum_i l_i$, with the individual orbital angular momentum l_i of the i^{th} electron. Similarly, the spin angular momenta couple to a mutual spin momentum $S = \sum_i l_i$, with the individual spin s_i. Those, in turn, couple together, yielding the total angular momentum $J = L + S$

The so-called *j-j-coupling* prevails for systems with even more electrons. For each electron, spin, and orbit couple to the total angular momenta $j_i = l_i + s_i$. This yields the total angular momentum of the system as $J = \sum_i j_i$.

In every real multi-electron system, both coupling mechanisms occur to a varying degree. While the atomic structure programs consider this, this work is not concerned with this distinction in greater detail. Instead, we

use the total angular momentum J to classify the electronic states of an ion. The magnetic quantum number m is used in reference to J accordingly, $m \equiv m_J$. Any quantum numbers describing spin coupling with the nucleus can be omitted, as our resolution is generally too low to resolve hyperfine structure.

2.3.2 Einstein coefficients

The *Einstein coefficients* are properties intrinsic to a specific transition in a particular ion. They describe the probability of the transitions occurring. Since there are two concurrent processes associated with each transition – spontaneous emission as opposed to stimulated emission/absorption– there are two Einstein coefficients: A_{ij}, concerning the spontaneous process and B_{ij}, concerning the stimulated processes.

As the experiments for this work are kept nearly completely dark, these stimulated processes are suppressed due to the low occurrence of matching photons. Subsequently, A_{ij} is of main interest here.

2.3.3 Zeeman

The *Zeeman* effect splits a transition into multiple components with individual energy shifts

$$\Delta E = \mu_\mathrm{B} B_\mathrm{ext}(m_{J,\mathrm{i}} g_{J,\mathrm{i}} - m_{J,\mathrm{f}} g_{J,\mathrm{f}}) \tag{2.21}$$

depending on the Landé g-factor (g-factor) for the total angular momentum J of initial $g_{J,\mathrm{i}}$ and final state $g_{J,\mathrm{f}}$ respectively, the z-projection of the total angular momentum of initial $m_{J,\mathrm{i}}$ and final state $m_{J,\mathrm{f}}$, and the Bohr magneton μ_B.

These components feature a known intensity correlation. The transitions are grouped together according to $\Delta m = m_{J,\mathrm{i}} - m_{J,\mathrm{f}}$. Since the $\Delta m = 0$ components are polarised differently than $\Delta m = \pm 1$ components, the reflection efficiencies along the optical path are different. This difference, however, is not generally wavelength-independent and is hence generally unknown. It is left as a free-fitting parameter. There are no observable transitions for other values of Δm. This leaves two intensity fitting parameters: I_0 for the central peaks with $\Delta m = 0$, and $I_\pm$ for the peripheral peaks with $\Delta m = \pm 1$.

The other intensities can be calculated from the *Clebsch-Gordan coefficients* with

$$I_k = I_{0/\pm} \langle j_\mathrm{i}, m_\mathrm{i} | j_\mathrm{f}, m_\mathrm{f} \rangle^2, \tag{2.22}$$

where $I_{0/\pm}$ refers to either I_0 or $I_\pm$, depending on Δm.

2.3.4 Rydberg–Ritz combination principle

The *Rydberg–Ritz combination principle* describes the relationship of spectral lines of any ion. It originally stated that spectral lines of an ion include lines that are either the sum or the difference of another line. Translating that from frequencies ν into photon energies, $E_{\text{photon}} = h\nu$, with Planck-constant h, it says that lines exist with an energy relation

$$\Delta E_1 = \Delta E_2 + \Delta E_3 \tag{2.23}$$

Regarding those transitions as connecting energy levels, the origin of this effect becomes clear. Let ΔE_1 connect the energy levels E_a and E_c,

$$\Delta E_1 = E_\text{c} - E_\text{a}, \tag{2.24}$$

and let there be an intermediate level E_b. If there are transitions between E_a and E_b, as well as E_b and E_c,

$$\Delta E = E_\text{b} - E_\text{a} \equiv \Delta E_2, \qquad \Delta E = E_\text{c} - E_\text{b} \equiv \Delta E_3 \tag{2.25}$$

must hold true for the transition's respective energy. Adding those yields

$$\Delta E_2 + \Delta E_3 = E_\text{b} - E_\text{a} + E_\text{c} - E_\text{b} = E_\text{c} - E_\text{a} = \Delta E_1 \tag{2.26}$$

the postulated relation.

With more information about the internal atomic states, this can be generalised and extended. This includes the knowledge of how the energy levels are connected, e.g. obtained from selection rules or transition rates. Instead of three lines and states, more complicated transition chains can be built to determine the exact energy of an unknown transition from multiple measured lines. With no loss of generality, we can also think of measuring the precise energy of levels, with respect to the ground state, by measuring the energy of transitions connecting the level with the ground state. From this point of view, new lines are predicted from the energy difference of thus determined levels.

2.4 Calculation of atomic properties

Atomic properties are calculated to obtain the principal electronic structure of the ions of interest. These results are used to contribute our line measurements to the corresponding electrical transitions. Two different codes were used in the course of this work: the *flexible atomic code (**FAC**)* and AMBiT.

Both perform *ab initio* calculations, delivering energy levels and transition rates. Furthermore, FAC contains a *collisonal radiative model (CRM)*, where plasma properties are considered to approximate relative line strengths in a given environment. AMBiT, on the other hand, calculates the g-factor, and thus the Zeeman splitting.

2.4.1 Flexible atomic code

The first code used for atomic calculations is the FAC. It features a strong focus on radiative collisional processes, as those present in EBIT plasmas. Its implementation of the configuration interaction (CI) method, combined with Dirac-Hartree-Fock iterations, yields fully relativistic results. The addition of distorted-wave approximations enables cross-section calculations of EII, CE, and collisional DE. [77]

FAC calculations require the specification of the electronic configurations to be included. Those are divided into three separate parts: The *core* configuration consists of the innermost electrons. They are assumed to remain unperturbed for the purposes of the calculations. Then, the *shell* of the *ground state* is added, including all electrons of the ion in question. This configuration is then used for the radial optimisation. The addition of more *shell* configurations completes the input. All given *shell* configurations are then used for the following CI iterations.

2.4.2 Collisonal radiative model

An important tool for linking measured lines to calculated levels is the CRM. It is part of the FAC software suite and pre-requires complete atomic structure calculations, including the CE and DE cross-sections mentioned above.

A Gaussian electron energy distribution, with a spread of 5 eV, is assumed for an EBIT. The set energy of the experiments is used as mean energy, with a cut-off 15 eV above and below. For ion-photon interaction, only spontaneous decay is taken into account. The ion-electron interaction covers collisional excitation and de-excitation. An electron density of $1 \times 10^{10}\,\mathrm{cm}^{-3}$ is assumed. For this work, the maximum number of iterations was set to 2048, the stabiliser to 0.5, and the accuracy to 10^{-6}.

The calculations are done for individual charge states, yielding synthetic spectra and relative line strengths for atomic transitions. These line strengths differ from the transition rates. As implementation of the electronic processes given in section 2.1.5, they are only valid for certain plasma conditions, while the transition rates are inherent atomic properties independent of experimental parameters. A calculation of the charge state distribution is not included.

It may be done separately and combined with the synthetic spectrum or, as in our case, inferred from the experimental results.

2.4.3 Ambit

The other program for atomic calculations used is AMBiT. It combines CI with many-body perturbation theory (MBPT). It treats inner *core* and the outer *shell/valence* electrons differently as well. Thus, a ground state configuration with a Fermi level ':' needs to be specified, separating fully occupied core-states from the shell-states, featuring of interest. The notation is relativistic for the valence states, with the higher subshell indicated by a '+' between the azimuthal quantum number indicating the subshell and the corresponding occupation number. The declaration of leading configurations, which is expected to influence the outcome the most, is necessary as well. Valence-valence interactions are subject to CI, while the treatment of core-valence is done by MBPT, as this reduces the computational cost, keeping them reasonable. This CI+MBPT method is used to produce fully relativistic calculations of atomic energy levels, allowing a direct link with the `FAC`-results, as well as g-factor, used for the prediction of Zeeman splittings. [78]

Chapter 3

Trapping highly charged ions

"Numquam ponenda est pluralitas sine necessitate"
"Plurality must never be posited without necessity"
—*William of Ockham* [79]

Optical spectroscopy needs long integration times and, therefore, an enduring fluorescence. To ensure that, it is beneficial to accumulate and store the matter of interest – in our case highly charged ions (HCIs). Ions are most commonly stored in Paul and Penning traps, storage rings, multi-reflection time-of-flight spectrometers and electron beam ion traps (EBITs). In principle, they are all capable of storing HCI once they are generated. On the other hand, only a couple of methods can be used to produce HCI: Charge stripping by thin foils or gases of fast ions, leveraging the electron-cyclotron-resonance in microwave cavities and ionisation by electron impact. It is preferable to use the same device for production and storage, as this ensures a steady supply and eliminates transfer losses, increasing the ion number and, thus, the signal strength. Both, storage rings using stripper foils/gases or electron impact ionisation (EII), and, EBITs, capitalising on EII, are able to do so. Due to the sheer size of storage rings, linked to high cost and complexity, EBITs are used for this work due to viability and practicability.

Their main working principles will be explained in this chapter. After that, the individual machines that played a role in the course of this work will be introduced in more detail. Naturally, the focus will be on their differences to one another.

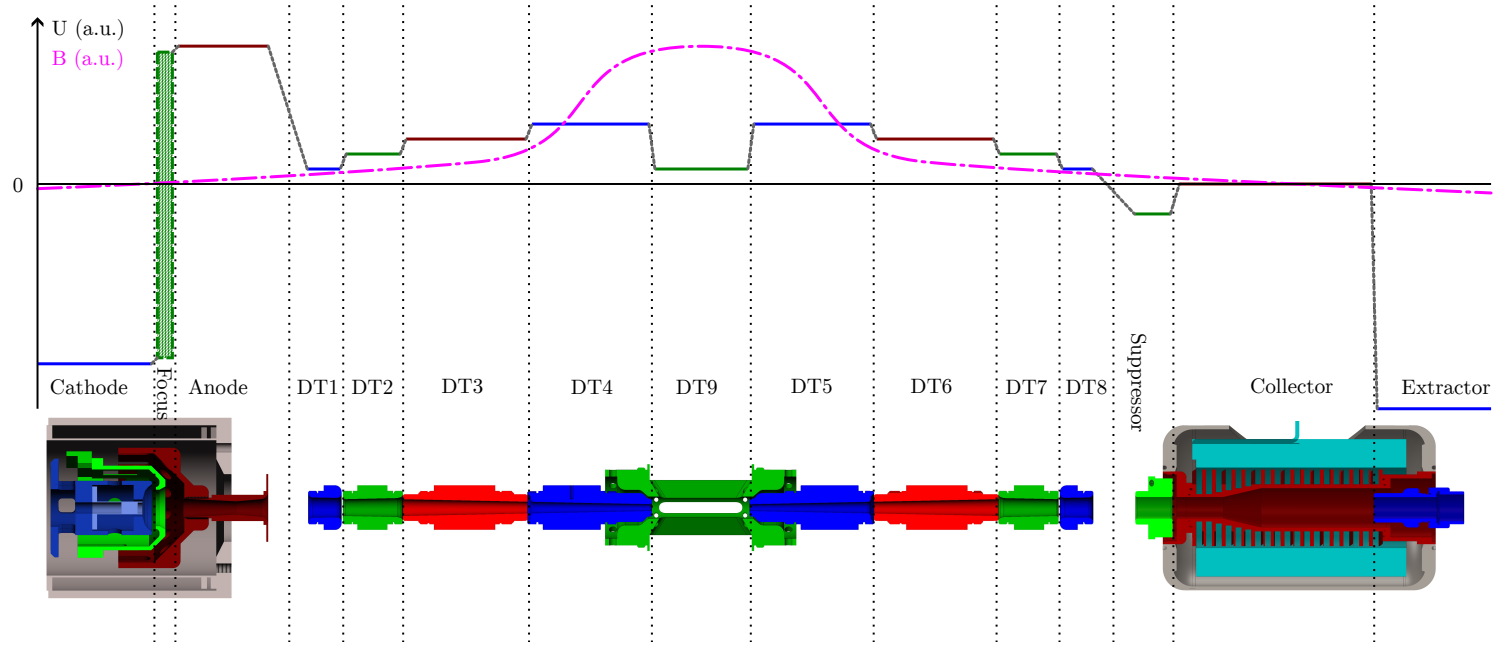

Figure 3.1: Illustration of a typical EBIT with indicated electric and magnetic fields along the z-axis. Neither parts, distances, nor field strengths are to scale. The solid and dashed lines show the electric field, and the dash-dotted line is the magnetic field. The electrical field's coloured segments correspond to the electrode of the same colour at this position; grey segments at dashed separation lines are the transition between electrodes. The suitable voltage range for the focus electrode is shown as a shaded area. Magnetic coils are shown in cyan. The main pair in the centre is superconducting and forms the overall shape of the magnetic field. The smaller ones trim the magnetic field to 0 at the cathode and collector. A combination of permanent magnets and ferromagnetic yokes can achieve a similar magnetic field.

3.1 Electron beam ion traps (EBIT)

The principle set-up of an EBIT is depicted in fig. 3.1. As the name suggests, its main feature is the electron beam originating in the gun, traversing the drift tubes and dissipating into the collector. It is maintained by electrons leaving a negative cathode ($\varphi_{\text{cathode}} \sim -1 \times 10^3\,\text{V}$), either by thermionic or field electron emission. In our case, only thermionic cathodes are used. They are accelerated by a positive anode ($\varphi_{\text{anode}} \sim 1 \times 10^2\,\text{V}$) through the interaction region inside the drift tubes towards the collector. A focus electrode – $\varphi_{\text{anode}} > \varphi_{\text{focus}} > \varphi_{\text{cathode}}$ – is used to regulate the current and pre-focus the beam.

A strong inhomogeneous magnetic field increases the current density above $\text{kA}\,\text{cm}^{-2}$ in the interaction region. The resulting negative space charge potential traps positively charged ions in the radial direction. With an appropriate potential landscape the so called drift tube (DT) – typically numbered, e.g. DT1, DT2, DT3, DT4, DT9, DT5, DT6, DT7, DT8 – work as end caps around the central DT9, completing the ion trap. Typically $\varphi_{\text{DT}} \sim 1 \times 10^1\,\text{V}$, with the central trap build by $\varphi_{\text{DT4}} = \varphi_{\text{DT5}} > \varphi_{\text{DT9}}$. Often, DT1-4 and DT5-8 are tuned symmetric, either flat or, as depicted, with a slight incline outward to efficiently expel evaporated ions. Hence, a reliable overlap between desired ions and the electron beam is ensured so that the interactions described in section 2.1.5 take place.

After the interaction region, the electron beam is collected by the grounded collector electrode. The resulting heating power makes actively cooling the collector mandatory. The extractor behind in the collector – $\varphi_{\text{extractor}} < \varphi_{\text{cathode}} < 0$ – prevents electrons from leaving the apparatus. The suppressor electrode – $\varphi_{\text{cathode}} < \varphi_{\text{supressor}} < 0$ – lets electrons enter the collector but prevents secondary electrons from deflecting back into the trap.

Loading an EBIT with the desired elements is called *injection*. It is sufficient to insert the element into the electron beam in any compound, for example, as an atomic beam, molecular beam, plasma, or already ionised. Once the electron beam is reached, dissociation and ionisation resulting in trapping take place. The injection methods used for this work are explained in detail in chapter 4.

This work refers to three dissimilar EBITs, discerned predominantly by their magnetic system. While they share the fundamental functional principles discussed above, their differences and peculiarities will be presented in the following sections. They are presented chronologically in respect to their development.

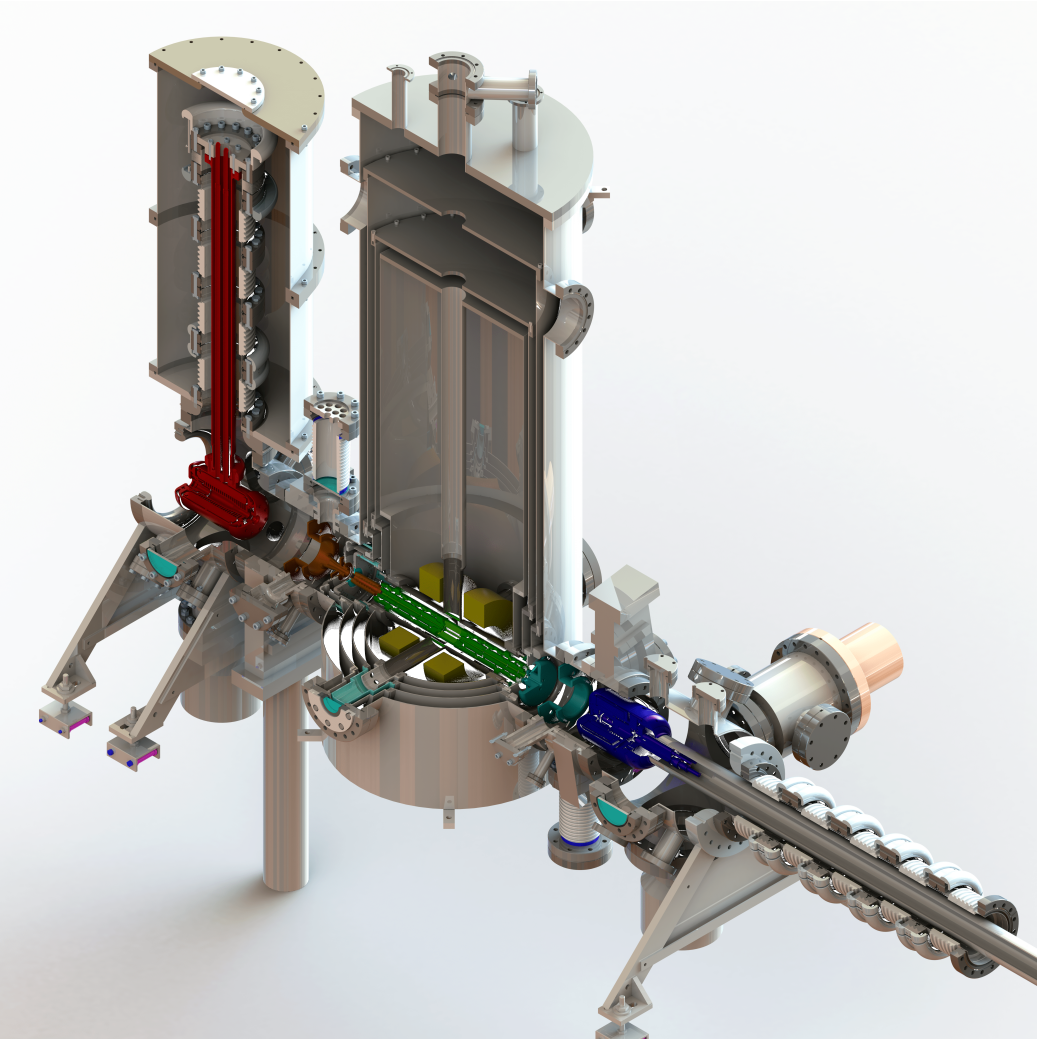

Figure 3.2: Overview of the HD-EBIT in cross-sectional view. The main components are, from bottom right to top left: The electron gun assembly is in blue, where electrons are freed and accelerated. Transitional electrodes to shape and transport the beam in teal. The DT assembly in green forms the trap region. It is surrounded by the coils of the superconducting magnet in yellow. This is followed by another set of transitional electrodes in orange. Finally, the electron beam reaches the collector (red), where the electrons are de-accelerated and reabsorbed. The coil and electrode assembly of this EBIT was already featured in fig. 3.1. Additionally, the two-stage thermal shielding encapsulating the helium dewar, housing the coils (yellow) and trap (green), can be seen. Also not the multiple ceramic insulators around the gun and collector tube (top left and bottom right, respectively), which allow for high acceleration voltages towards the trap center.

3.2 The Heidelberg(HD)-EBIT

The HD-EBIT is, in a way, the basis of EBIT development and experiments in Heidelberg. Initially conceived as Freebit (Freiburg EBIT), it was soon transported to Heidelberg, where it remains to this day. An overview of this setup is shown in fig. 3.2. The main components – gun, drift tubes and collector – are exactly the ones used for the general explanation above.

In contrast to fig. 3.1, which is not to scale, there is some distance between those three parts that also contain transitional electrodes. These electrodes are mounted into a unit with the drift tubes, albeit they are not used for ion trapping but rather to tune the electron beam. Additionally, if one extracts ions from the trap, they may be used to optimise the extraction efficiency. This clearance is needed to allow for high voltages between the drift tubes and the gun and collector assembly respectively. Electron beam energies E_e in the $E_\mathrm{e} \sim 10^2\,\mathrm{keV}$ range have been proposed initially, with $E_\mathrm{e} \approx 70\,\mathrm{keV}$ in actuality achievable in stable operation. To allow that voltage difference between gun and collector, on high potential, and the main vacuum chamber, which is grounded, an array of ceramic insulators is used. In fig. 3.2, they are seen in white around the red collector pipe, as well as around the grey gun pipe (right bottom of the blue gun), respectively. This allows the uppermost flange of the collector chamber and the bottom right flange of the gun chamber to be about 100 kV above ground. To prevent short circuits on the outside, these flanges are surrounded by Faraday cages. In the case of the collector, that cage is a tank of insulating SF_6, and can be seen in fig. 3.2 surrounding the insulation around the red collector pipe. In the case of the gun, it is an actual high-voltage cage made of an aluminium grille. It surrounds a whole miniature 19-inch equipment rack which operates both gun and collector, to which it is connected by a cable duct inside the tubing, insulated by SF_6.

Inside this duct run several high voltage cables, for all collector electrodes, as well as two hoses need for water-cooling the collector. The duct and the gun rack are electrically isolated. Therefore, non-conducting distilled water is used as a coolant. This insulation is used to determine the electron current reaching the collector by measuring the current between collector ground, i.e. the duct, and gun ground, i.e. the rack. This is realised by measuring the voltage drop over a high power resistance. Additionally to a multitude of power-supplies the rack features a water-air heat exchanger, dissipating the cooling power into the ambient air, and a control server to operate all the power-supplies. The server is connected to the network via fibre optics, while the electrical power supply is realised by a motor-generator pair connected by a glass-fibre pole, backed up by an uninterruptible power supply (UPS).

The UPS is mainly used for starting and ending high voltage operations, as for normal operation, a direct power line between the laboratory and gun rack is used.

Apart from high voltage insulation, high beam energies call for high beam compression and, therefore, a high magnetic field at the trap centre. To achieve this, the HD-EBIT is equipped with a superconducting magnet. It runs currents up to 76.24 A, achieving a maximum field of 8 T at its centre. The magnet consists of two coils suspended in a bath of liquid helium. It is thus thermalised to $T_{\mathrm{LHe}} \approx 4.2\,\mathrm{K}$ by evaporative cooling, ensuring superconductivity. Once the magnet is charged, the coils are short-circuited to achieve persistent and consistent current and, thereby, a magnetic field. The magnetic field does not change measurably in our operation times of a week - after that, the helium needs to be refilled. The refilling is done with an uncharged magnet to avoid quenching caused by disturbances in the helium dewar.

To decrease the evaporation rate, the helium tank is surrounded by two heat shields, mounted by low cross-section spokes and wires, and separated by vacuum from each other, the dewar and the outer chamber. These are the four concentric cylinders in the centre of fig. 3.2, from inside to outside: Helium dewar at $T_{LHe} \approx 4.2\,\mathrm{K}$ (containing the green drift tube and the yellow magnetic coils), heat shield one at $T_1 \approx 20\,\mathrm{K}$, heat shield two at $T_2 \approx 40\,\mathrm{K}$, and the vacuum chamber at the room temperature $T_{\mathrm{Room}} \approx 295\,\mathrm{K}$. To reduce radiation heating, a line of sight, especially in the infrared range, between the outer chamber and the helium dewar is prevented wherever possible through lenses, apertures, or windows. The heat shields are cooled by a cryocooler, mounted on top of the chamber, and driven by a closed-cycle helium compressor, which is located outside the laboratory. It is a two-stage, with the first stage between T_{Room} and T_2, and the second stage between T_2 and T_1. Typically the cryocooler is used to cool the whole apparatus, with the helium dewar thermalizing by radiation, taking about two weeks, before liquid helium is filled to make the magnet superconducting. A positive side effect of cryogenic temperatures is the improved vacuum. The cold surfaces of the shields and dewar act as a large cryopump, condensing and freezing residual. This guarantees an overall ultra-high vacuum (UHV) below $1 \times 10^{-9}\,\mathrm{mbar}$, and even lower in the trap centre, which incidentally is also the centre of the 4 K region. Reducing residual gas is most critical there to prevent charge exchange and minimize the inflow of undesired elements into the trap. Four ports in the principal spatial axes ensure access to the trap. The top one is currently unused, the right one connects to the optical spectrometer, the bottom one allows the gas injection and the one to the left leads to a beryllium window and to an x-ray spectrometer.

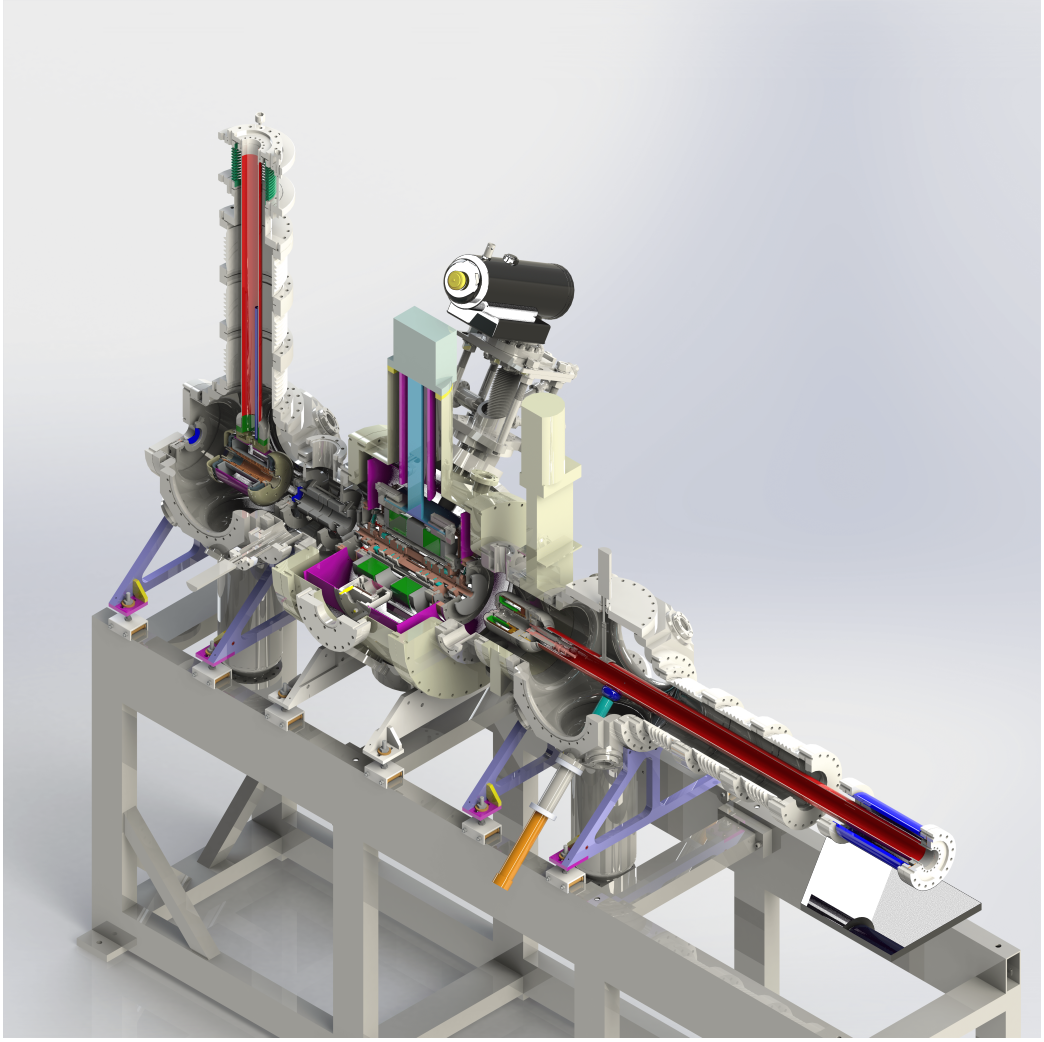

Figure 3.3: FLASH-EBIT overview in cross-sectional depiction. Analogues to the HD-EBIT in fig. 3.2, from bottom right to top left: Gun, hold by the carrier tube (red), around it three ceramic insulation rings (white) between gun chamber and gun mounting (blue) can be seen. Magnet and drift tube assembly, surrounded by the heat shield (magenta). On top, the cold head is depicted with a coaxial heat transfer connection (magenta/light blue). Next comes a Sikler lens (grey) to aid in ion extraction. The last part is the collector, suspended by a tube (red) from above. The three insulation rings (white) between its mounting (green) and chamber can also be seen. More details can be found in the main text.

3.3 The “free electron laser Hamburg”(FLASH)-EBIT

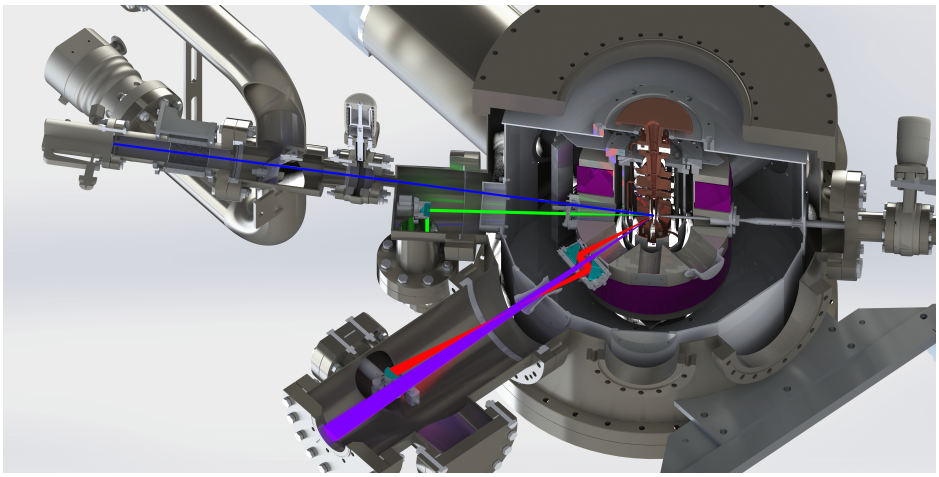

Figure 3.4: Illustration of the access-port usage of the FLASH-EBIT. Counter-clockwise from the top: Concentric connection to the cryocooler, compare fig. 3.5. Differentially pumped gas injection system, including needle valve, turbo molecular pumps, aperture and hand valve. Gaseous beam an an angle in blue. Laser (green) access at the same port, at a slight angle. Spectroscopy port, horizontal in the laboratory frame. VUV path in purple, optical path in red. Two unused ports. Ablation target, retractable behind the hand valve for target exchange. Another unused port. The last, unseen port is connected to an XUV spectrometer.

The FLASH-EBIT establishes the second generation of EBITs in Heidelberg. An overview in cross-sectional depiction can be seen in fig. 3.3. Since most parts of the FLASH-EBIT are analogous to the HD-EBIT described above, this section focuses primarily on the innovations and modifications.

Technological advancements in cryocooler technology permitted to omit the helium dewar, without major changes of the basic operating principles. The two-stage cooling system reaches temperatures of $T_1 =\approx 4\,\mathrm{K}$ and $T_2 =\approx 40\,\mathrm{K}$ in equilibrium. Hence, superconductivity can be achieved directly at T_1. The simplified cryogenic set-up can be seen in fig. 3.5. This allows for seven access ports orthogonal to the electron beam at the main axes and diagonal, minus the top one for the cooling connection.

Additionally, it is designed for lower beam energies and thus accelera-

tion voltage between DT and gun/collector. Only uses three instead of five ceramic insulations between the chambers. Transitional electrodes can be excluded as well. It has electrodes only used for the extraction of ions, which are out of the scope of this work. The decision for lower voltages was made to preserve transportability: The lower voltage allows to shrink the gun cage from a whole room (as with the HD-EBIT) to about rack-sized. To do so, the DT power supplies are placed in a rack with elevated potential, physically separated from the EBIT. The cables connecting the rack to the EBIT feature an additional insulation made from acrylic glass, which is sufficient for this lower voltage. Instead of the SF_6 tank used for the HD-EBIT, an acrylic glass cylinder (not shown) is used around the collector as well.

These measures permitted transportation of the FLASH-EBIT in a commercial shipping container. It was thus deployed at various high-energy radiation sources, like the Berlin electron storage ring society for synchrotron radiation (BESSY) or the free electron laser in Hamburg (FLASH), from which it got its name, as this was its initial application.

In the course of this work, substantial alterations for the application of the access ports have been designed. The result of those designs can be seen in fig. 3.4 and will be discussed in more detail in the following chapters.

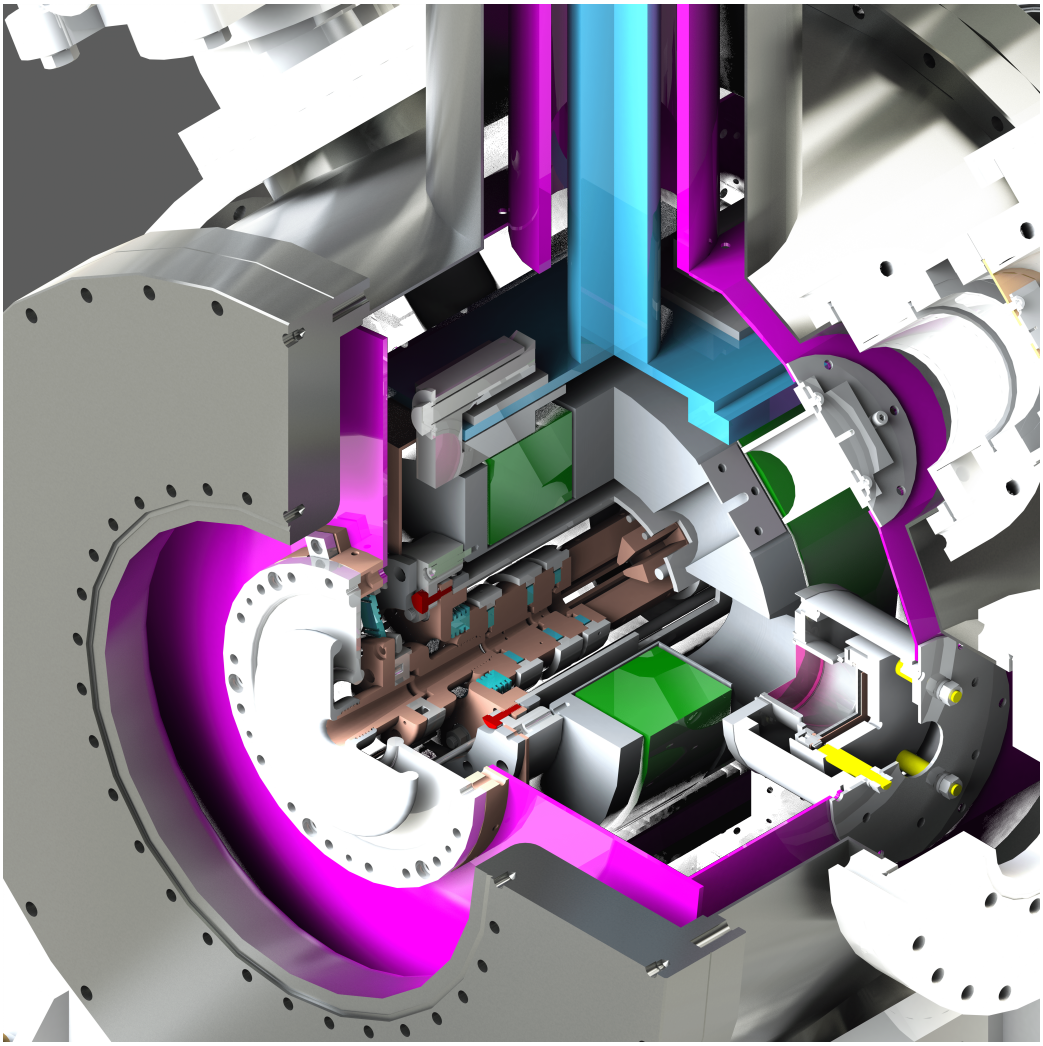

Figure 3.5: Detailed cross-sectional view of the main chamber. The left half of the assembly is shown to allow a more detailed view – the other half is symmetrical and works analogues. Above the picture, the cryocooler is located, as can be seen in fig. 3.3. Its coldest temperature is connected to the core (light blue), the higher temperature to the shield (purple), while the outside chamber (grey) is on room temperature. The core is connected to the magnet coils (green) as well as the central drift tubes (brown), the shield connects to the trumpets (copper/brown center, aluminium/gray surrounding, bottom left of the image), enclosing everything. Heat conduction whilst electrical insulation is ensured by sapphire (teal). Heat and electrical insulation between drift tubes and trumpet is done by ceramics (grey).

3.4 The “extreme ultraviolet”(XUV)-EBIT

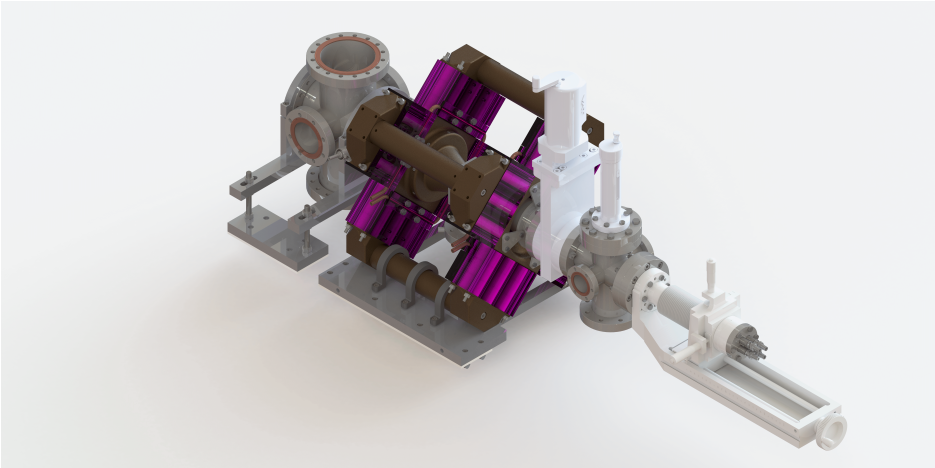

Figure 3.6: Vacuum chambers and magnetic system of a HC-EBIT rendered in solid works. From top left to bottom right: Collector chamber — magnetic system (purple/brown) enclosing the drift tube chamber — gun valve — gun chamber — gun manipulator. The magnetic system is made of two main components: soft iron yokes (brown) and permanent magnets housed in aluminium cartridges (purple). The cartridges are made translucent in this schematic to show the arrangement of the 72 permanent magnets.

The last EBIT used in the course of this work is the extreme ultraviolet EBIT (XUV-EBIT). It was built primarily to supply an XUV spectroscopy setup with HCIs and named accordingly. While the whole setup is out of scope for this work, the EBIT itself provided a suitable testing field for the laser injection method described in section 4.4. It is of the *HC-EBIT* type that are thoroughly described in [80]: Utilising 72 permanent neodymium magnets housed in aluminium cartridges and soft iron yokes, magnetic fields up to 0.86 T can be achieved in such a compact, room-temperature device. This magnetic system, as well as the vacuum chambers, can be seen in fig. 3.6.

Figure 3.7 shows a cross-sectional overview of the inner electrodes. The three main parts, gun, trap and collector, are very close together in this arrangement. This allows a high ratio of the electron beam to reach the collector, with a limit on electron beam energy as a drawback. In fig. 3.8, the electron gun assembly is shown in detail. The cathode's three parts are on the same principal potential $\sim 10^3$ V. A small voltage offset of ≈ 4 V is applied between the green handle and the teal/blue holder assembly. This drives a

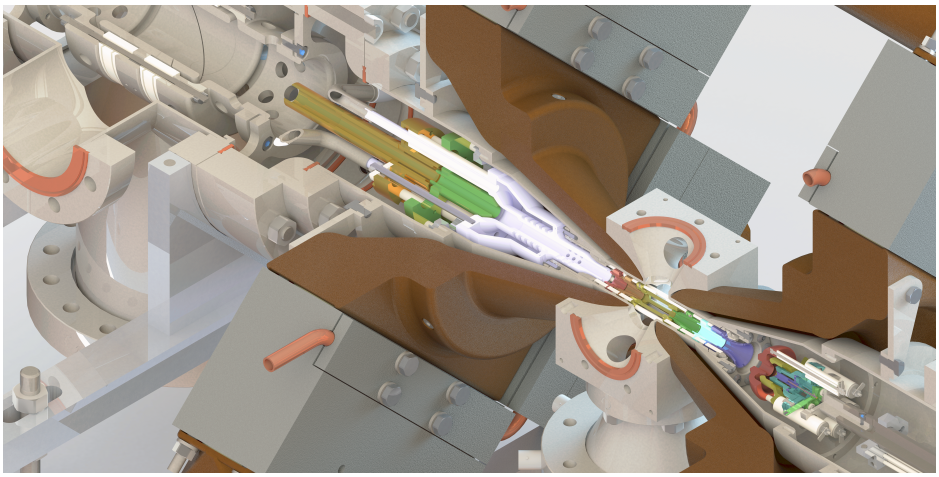

Figure 3.7: Cross-sectional view of a HC-EBIT. Bottom right to top left: Electron gun (red, yellow, teal around purple, green) — drift tubes (red, orange, yellow, green, teal, purple) — collector electrodes (orange, green, lilac). The electron beam runs from bottom right to top left. Surrounding the electrodes, the inner part of the magnetic system can be seen: The grey housing of the array of permanent magnets (compare translucent purple in fig. 3.6) connected to the two cones' soft iron yokes (brown). The gap between the two cones ensures a 0.86 T magnetic field in the centre of the trap.

heating current of about $\approx 1.2\,\mathrm{A}$, resulting in $\approx 5\,\mathrm{W}$ heating power, allowing electrons to leave the barium oxide surface. Then, the main acceleration of electrons is from cathode to anode, with the focus controlling the current, as explained in section 3.1.

The beam then leaves the gun towards the drift tube assembly shown in fig. 3.9. Unlike the superconducting EBIT shown in sections 3.2 and 3.3 the drift tubes of the HC-EBIT are not symmetric around the trap: DT 1 (in purple) is shaped like a trumpet to keep a distance to stay out of the way of an electron beam that is not fully compressed yet. Its voltage is typically chosen to tune the electron beam. Therefore, one might even think of DT 1 as more of a transitional electrode than a drift tube. On the other side of the trap, instead of another trumped-shaped electrode, the collector (in lilac) is positioned. There is no need for a trumped shape, as the electrons are supposed to be absorbed by this electrode anyway. DT 2 (in teal) is the first nearly cylindrical drift tube. It is a bit longer than its corresponding counterpart DT 6 behind the trap so that it connects seamlessly to the trumpet of DT 1 while on the other side moving the collector closer to the

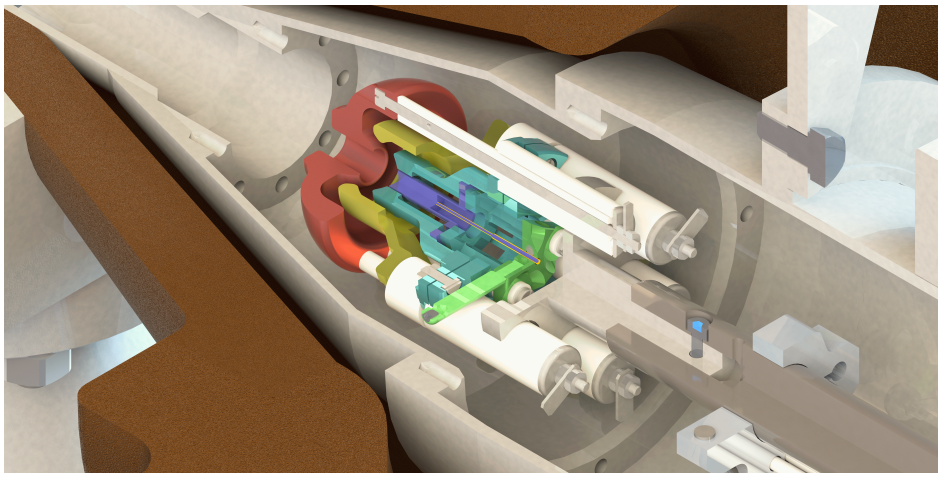

Figure 3.8: Schematic cross-section of the gun assembly of the HC-EBIT. From top left to bottom right: Anode (red) — Focus(yellow) — Cathode (teal, purple, green). The cathode is divided into three main parts: The two-part molybdenum holder (teal) holds the dispenser cathode (purple) in place. The dispenser cathode's filament (orange/purple) is connected to the "handle" (green) to apply a heating current to the cathode.

trap. DT 2 and 6 are also tuned according to the electron beam, although considerations of extracting ions or emptying the trap of unwanted ions come more into play here. DT 3 and 5 are close to symmetrical – DT 5 still being slightly shorter for the same reasons as above. Together with DT 4, they form the axial trapping potential in most operation cases.

Figure 3.10 shows the complete collector assembly. As mentioned above, it prolongs up to the drift tubes, with the collector electrode effectively constituting a seventh drift tube. The extended length allows for the deceleration and absorption of all electrons. As they transfer their kinetic energy, water cooling is necessary to dissipate the resulting heat. The extractor is split into two parts, green and orange. Routinely, the green one is used to ensure that no electrons leave the EBIT, while the orange one – also known as the extraction tube – is used as an ion lens to tune ion extraction. For this work, extraction of ions was not necessary, so both electrodes were put on the same potential. Contrary to the explanation in section 3.1, the HC-EBIT does not feature a suppressor electrode. However, due to the low electron beam energies, secondary electrons are not as problematic.

Electron beams with 80 mA current and energies up to 10 keV have been reported with this setup. For the purpose of this work, HC-EBITs are ad-

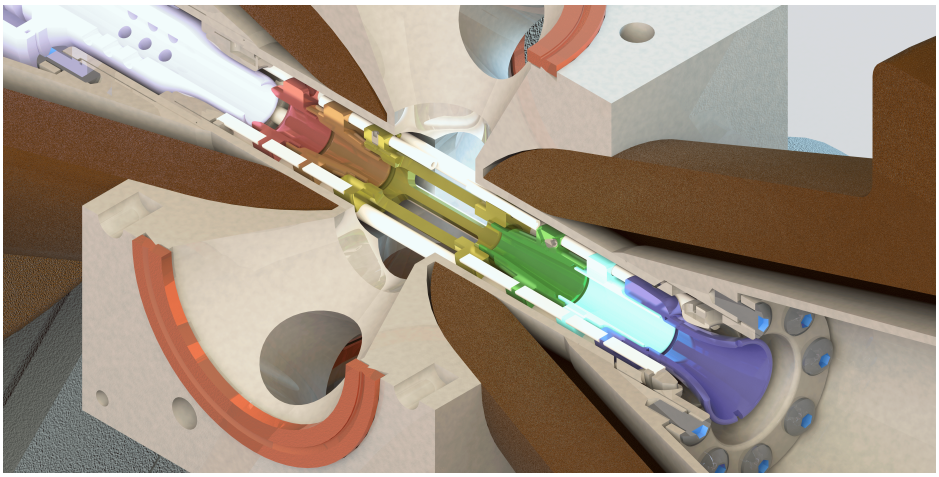

Figure 3.9: Cross-section of the HC-EBITs DT assembly. The DTs are typically numbered consecutively from gun side (purple, No. 1) to collector side (red, No. 6). The central DT 4 (yellow) features four slits to allow access to the trap for various purposes, e.g. injection or spectroscopy. DT 4 is situated in the gap of the soft iron yokes, where the magnetic field is entirely in the vacuum. This results in the highest magnetic field along the electron beam and, thus, the maximal beam compression and electron density. The last DT 6 is located directly in front of the collector (light violet, top left).

vantageous in two ways: Firstly, their permanent magnetic field and low operating cost would allow for a long, continuous operation, resulting in very accurate data due to averaging over a long time. Secondly, their simpler construction – especially the absence of heat shields – simplifies the access for the trap, both for spectroscopy and laser injection, compare sections 4.4 and 5.2. This comes at the drawback of a lower magnetic field – yielding less pronounced Zeeman shifts and lower beam currents – ensuing less photon flux and lower beam energies – limiting the achievable charge states.

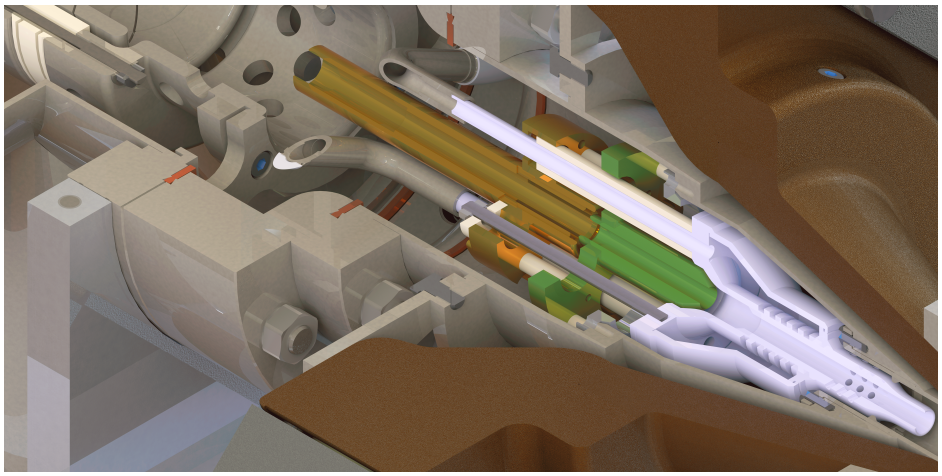

Figure 3.10: Collector assembly of the HC-EBIT in cross-sectional view. It consists of three electrodes: The grounded collector (light violet), where the electrons are deposited; the extractor electrode (green) on a negative potential below the cathode to prevent electrons from leaving and the extraction tube (orange) that can be tuned to optimise ion extraction from the EBIT. The water pipes (grey/light violet) and cooling ribs (light violet) are necessary to dissipate the energy of the collected electrons. Note that, due to spatial constraints, there is no suppressor electrode.

Chapter 4

Injection of chemical elements

"Wer nicht verändern will, wird auch das verlieren, was er bewahren möchte"

"Anyone unwilling to implement change will also lose what they seek to preserve"

—*Gustav Walter Heinemann* [81]

As noted briefly in section 3.1, *Injection* is the process of loading desired elements into the trap of an electron beam ion trap (EBIT). This is achieved once the matter, in an almost arbitrary manner, reaches the electron beam inside the central drift tube (DT) and is consequently ionised. Typical states for the injected matter include atomic or molecular beams, plasmas, ions or even solids.

This work is concerned with the methods of gaseous injection (GI), where an atomic or molecular beam is formed, and laser injection (LI), where plasma is produced. Before the detailed setups of the various experiments are discussed, this section describes both methods more generally.

4.1 Gaseous injection

Gaseous injection (GI) is one of the constructionally simplest methods, but the materials injected are limited to a few categories:

- gaseous elements, e.g. noble gases, nitrogen N_2, oxygen O_2

- volatile elements, e.g. iodine I_2, bromine Br
- volatile organometallic compounds, e.g. iron pentacarbonyl $FeCO_5$, tetraethyl lead $Pb(C_2H_5)_4$

The gaseous injection system in our laboratories relies on two differentially pumped chambers separated by a small aperture. Both chambers are pumped by a separate turbo molecular pump. On the EBIT side of this aperture, the so-called second stage, the pressure is typically in the ultra-high vacuum (UHV) range, with a mean free path above the chamber size, allowing free molecular flow. The aperture is positioned and shaped in such a way that the molecules – or atoms – passing it reach the electron beam at the trap center. Additional apertures may be used to reduce residual gas inflow through diagonal momentum.

On the far side of the aperture, in the first stage, a wide range of pressure is acceptable. It is typically limited by the pressure increase in the second stage. At this stage, different configurations are possible, depending on the injected substance: Gases are supplied in a pressurised bottle, separated from stage one by a needle valve to decrease the pressure and limit the flow. For volatile elements, the excess air around the sample is initially removed with a backing pump and closed off afterwards to prevent the sample from being pumped out. Depending on their phase diagram, elements or compounds already turn gaseous due to reduced pressure. Those are separated with the needle valve as well, controlling the inflow. Less volatile matter is directly connected to the first stage and heated, regulating the inflow through the temperature. Heating of the whole injection system is required to prevent condensation at colder sections along the injection path.

4.2 Laser injection

Unfortunately, a volatile organometallic compound is not known for all metal elements, limiting the applicability of the gaseous injection method. Additionally, this method requires comparatively large quantities, as the turbomolecular pump of the first stage pumps out a sizeable fraction of the sample. This led to the development of the *laser injection (LI)* method for EBITs as reported in ref. [82]. They achieved a very high capture efficiency by inducing the desorption of atoms at a sub-millimetre distance from the electron beam. The position is found by incrementally moving in until bremsstrahlung can be seen on an x-ray detector, then retracting the target until the signal is gone. The name *desorption* was chosen to stress the difference to *ablation* processes that need higher laser power and remove much more material. Samples as

low as $\approx 300\,\mathrm{pg}$, $\approx 10^{12}$ atoms, respectively, were shown to be sufficient to load the trap. This allows the usage of enriched isotope as well as synthetic radioisotope samples in an EBIT.

The system uses two diametrically opposed access ports of an EBIT, one for the sample, the other for the laser. The sample is affixed to a target. Larger samples may be spot-welded onto it. For rare isotopes, a drop-on-demand ink-jet printer is used. Condensing a suspension of the sample material in lactic acid onto the target, forming polylactic acid (PLA), is another possibility. This addition of light elements to the injection is not dissimilar to the organometallic compounds above and is generally considered unproblematic. To allow positioning close to the electron beam, that means inside the central drift tube, the target potential needs to be carefully tuned to $\varphi_{\mathrm{Target}} \approx \varphi_{\mathrm{DT6}} - U_{\mathrm{SC}}$.

Typically pulsed lasers are used, particularly Q-switched, frequency-doubled Nd:YAG laser, featuring pulse energies of $E \sim 1\,\mathrm{mJ}$ and pulse durations of $t < 10\,\mathrm{ns}$ at $532\,\mathrm{nm}$. Contrary to the system described here, LI may be realised with laser ablation at a larger distance – allowing more freedom in the overall design at the cost of efficiency, as will be discussed below.

4.3 "Contamination" with light elements

There are various sources of light elements, i.e. nuclear charge $Z \sim 10^1\,e$, that get injected into the trap inadvertently. Foremost, residual gas stems typically either from cleaning processes containing carbohydrates and water (H, C, O), and ambient air (H C, N, O). Additionally, the injection process may induce carbohydrates as well, either from the organometallic compounds or from the PLA-substrate.

Fortunately, this does not interfere with most highly charged ion (HCI) applications: Due to their low Z, they feature substantially different ionisation energies than the ions of interest. More precisely, the energy separation between neighbouring charge states is higher at the same energy than for larger ions. E.g. O VII at 739 eV and O VIII at 871 eV are separated by 132 eV, while for lead the separation between Pb XXV at 750 eV and Pb XXVI at 810 eV is only 60 eV [83]. They are, therefore, easily identifiable in an electron beam energy scan. This is explained in more detail in section 6.2. It also helps that these elements are easily accessible experimentally, and their spectra are therefore well known. At the same electron beam energy, heavy ions are bound stronger in the trap than light ions, an effect that leads to the so-called evaporative cooling, reducing the temperature of the remaining HCI [84]. This significantly reduces the ion count of

light elements, suppressing their signal.

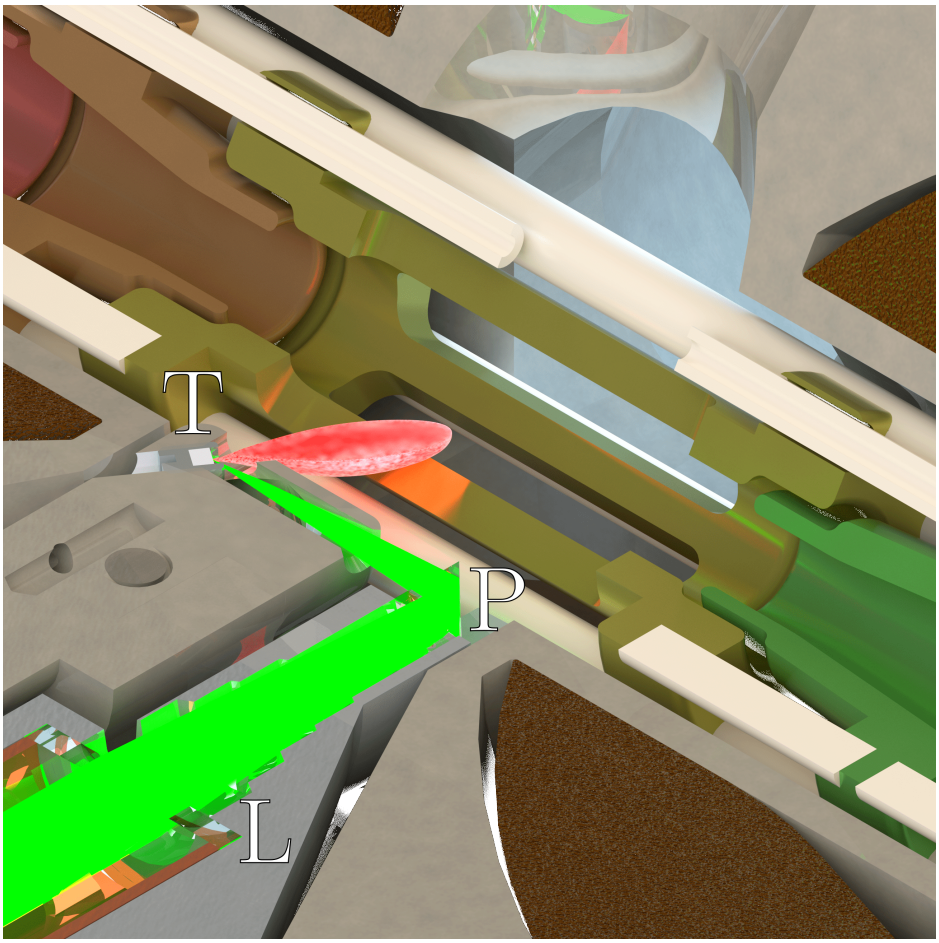

Figure 4.1: Visualisation of the one-sided LI procedure in the HC-EBIT. The green 532 nm laser enters collimated from the bottom left. The lens L focuses the beam, after deflection by the prism P, onto the target T, where a plasma plume (red) originates orthogonal to T and thus in the direction of the EBITs trap region.

4.4 Novel laser injection for Heidelberg Compact (HC) EBITs

The first laser injection system developed during the course of this thesis was for the HC-EBIT type to be used at the extreme ultraviolet EBIT (XUV-

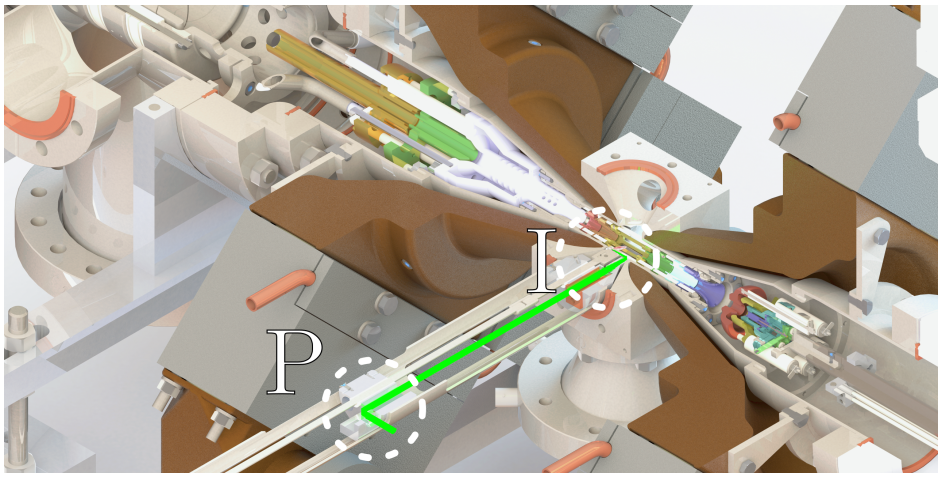

Figure 4.2: Overview of the ablation laser path in cross-sectional view. The laser enters through a window (not shown) and gets reflected towards the EBIT by the prism P. The interaction region I, where the other optics, the target and the trap are located, is shown in more detail in fig. 4.1.

EBIT). The overarching goal was to equip a HC-EBIT with an optical spectrometer to leverage its low operating costs for long exposure times.

A laser injection system for HC-EBIT already existed, but it required two opposite access ports. In the case of the XUV-EBIT, however, these were no longer available: The spectrometer was to be attached at the top, while the gas injection system on the right port had to be retained. Accordingly, the development of a new type of injection system requiring only a single access port was necessary. However, more common isotopes were planned for this case, relaxing the efficiency requirements and allowing for a system further away from the trap.

An illustration of the injection process can be seen in fig. 4.1, with the complete system depicted in fig. 4.2. The sample is applied to a target positioned at an angle, pointing at the trap centre. This allows the laser to be led on the same side of the trap while still being focused on the target. Laser-ablated material, on the other hand, is ejected orthogonally from the target towards the trap centre.

As with the system discussed in ref. [82], the target needs to be on the right potential. Thus, the whole target holder is insulated towards the chamber. In this case, the target needs to be on or above the voltage of DT 6. Otherwise, charge separation inside the plasma results in positive ions deflecting from the drift tube, as they do not have enough energy to surpass

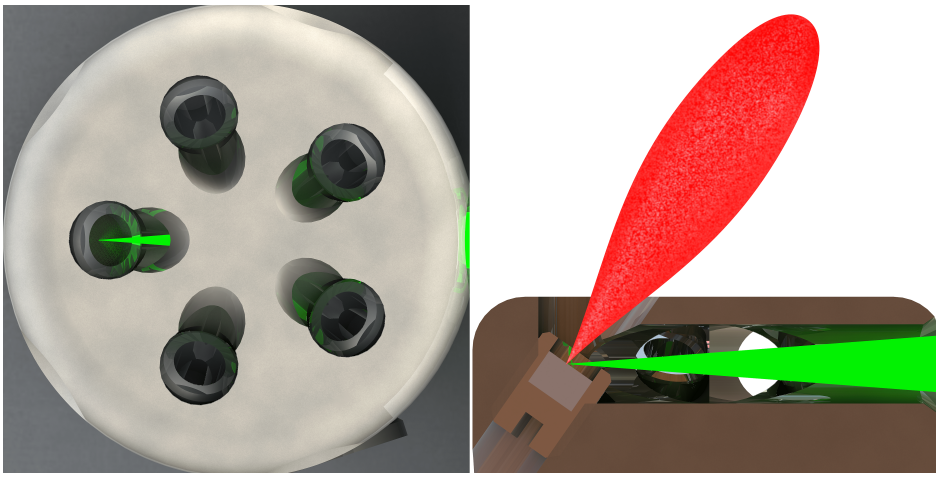

Figure 4.3: Detailed depiction of the target holder of the HC-EBIT-LI system. Left: Top-view of the target holder. Right: Cross-sectional view of the target holder.
The arrangement of the five different samples can be seen. Rotation of the holder changes between them. The samples are applied to modified set screws, forming the targets. The laser is led surface parallel inside the holder. The targets are slanted at the adequate angle, ejecting the plasma towards the trap once hit.

the potential barrier. Inside the central drift tube, the negative space charge of the electron beam draws ions into the beam, trapping them.

Our target holder features a five-fold symmetry, as can be seen in fig. 4.3. This allows up to five targets to be mounted at the same time, enabling fast switching between up to five samples without breaking the vacuum.

This system was designed in collaboration with the physialisch-technische Bundesanstalt in Braunschweig. Two implementations of the design have been manufactured, one for the extreme ultraviolet (XUV)-experiment in Heidelberg and one for the HCI experiment in Braunschweig. [85]

4.5 New injection system for FLASH

At the free electron laser Hamburg EBIT (FLASH-EBIT) we decided against this one-sided approach. It was deemed too complicated to fit a system similar to the one described in section 4.4 into the cryogenic system. Still wanting to minimise the uptake of ports, we decided to change the gas injection system slightly: The gaseous beam is now skewed 7° from the port axis,

allowing the laser to enter through the same port. Outside the chamber, the frequency-doubled laser gets widened to about 10 mm so that damage thresholds of windows and lenses do not cause any issues. It then passes to mirrors, allowing full control of the beam position and direction. One of them is driven by stepper motors to allow remote operation and precise positioning of the laser on the target. Then it is focused by a lens, with the focal point located at the 40 K aperture. After the lens, it passes through the centre of a drilled-out mirror. The mirror allows a charge-coupled device (CCD) camera, equipped with a telephoto lens, to look along the laser path, focused on the aperture plane as well. After this mirror, the vacuum chamber is entered through a window. The pathway in the chamber is shown in fig. 4.4. Another mirror, M, reflects the laser onto the aperture, and the aperture image back to the camera receptively. Here, an intermediate image of both laser focus and target is formed. Lens L maintains a 1:1 imaging of the target and this intermediate image, focusing the laser onto the target for ablation and relaying the observed ablation back to the camera.

The sample holder construction can be seen in fig. 4.5. The sample is mounted onto the sample holder (red), typically a condensed suspension of PLA, as described above. The holder is made from titanium to be lightweight and robust. Such targets are screwed onto the sample carrier (yellow). Screwing ensures both electrical and thermal conductivity between both parts. The carrier is made from oxygen-free copper and, therefore, features high thermal and electric conductivity. Thermally, it is connected to the 4 K-stage by the teal ball and cylinder construction, held by a sapphire (heat conductive, electrically insulating) ring. The ball fixes the x-y-position at that stage, leaving the z-position (along the cylinder axis) and the angles as variability. Electrically, it is connected with a set screw to the copper connection inside the green tube. At the end of the tube, a wire connects to a safe high voltage (SHV) feed through. It thus can be tuned to the appropriate potential $\varphi_{\mathrm{Target}} \approx \varphi_{\mathrm{DT6}} - U_{\mathrm{SC}}$.

The tube is made from fibreglass, isolating electrically and thermally. It runs from the room temperature, grounded outside, through the 40 K shield until the carrier at 4 K and high voltage $\varphi_{\mathrm{Target}}$. The thermal connection to the 40 K by copper springs minimises heat transfer from the room temperature through the slightly remaining conductivity. The flexible nature of the link does not constrain the position. The tube is mounted rigidly with a flange onto a high precision UHV manipulator. Its stroke length of 600 mm enables the sample to be retracted behind a UHV gate valve, allowing an exchange without breaking the vacuum in the main chamber. This accelerates target exchanges greatly, as vacuum and cryogenic temperatures can be maintained inside the trap; only the much smaller exchange chamber

needs to be pumped. The x-y-component can be moved inside 12.5 mm circle. While the position is fixed at the ball position, movement at the back bends the flexible fibreglass tube. This moves the sample at the tip in the opposite direction, scaled-down $\frac{\approx 90\,\mathrm{mm}}{\approx 810\,\mathrm{mm}} \approx 1:9$ due to the shorter lever arm, enhancing precision. This permits a LI operation analogues to ref. [82]. Thus, alternating, as well as simultaneous, gas and laser injection is possible at the FLASH-EBIT.

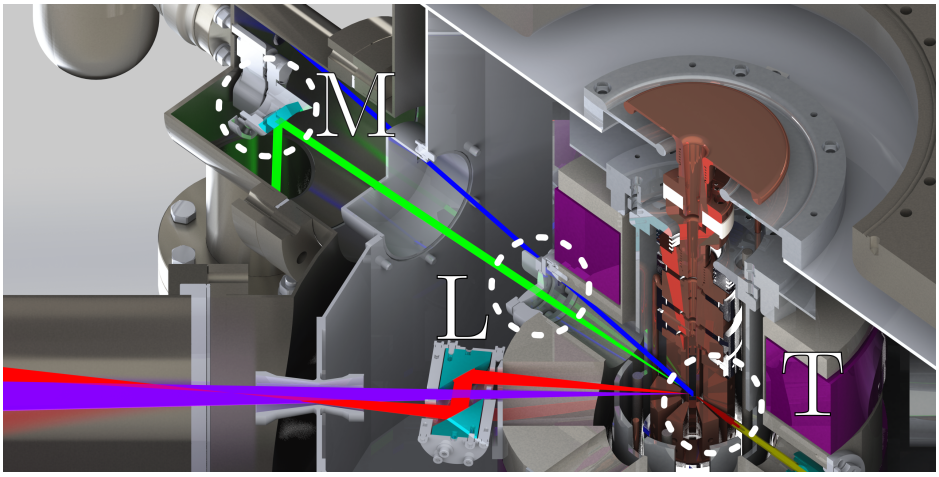

Figure 4.4: Laser pathway of the FLASH-EBITs LI system in cross-sectional view. The 532 nm laser, shown in green, enters the chamber collimated from a window below. It is then reflected by the mirror M towards the trap centre. Lens L focuses the beam onto the Target T. Note that the whole picture is turned for visibility; Actually, the drift tubes are in the horizontal, and the laser / GI port is in the upper diagonal.

4.6 HD-EBIT gas injection system

For the experiments with the Heidelberg EBIT (HD-EBIT), its gas injection system was used. It corresponds to the gas injection system descriptions above. Its two differentially pumped chambers are separated from the main chamber by a gate valve. This is opened once the desired steady injection pressure is adjusted. Additionally to the aperture between the injection chambers, each heat shield is equipped with an aperture as well, minimizing the divergence of the beam. This prevents material from freezing inside the trap, which happens when volatile compounds hit the 4 K stage.

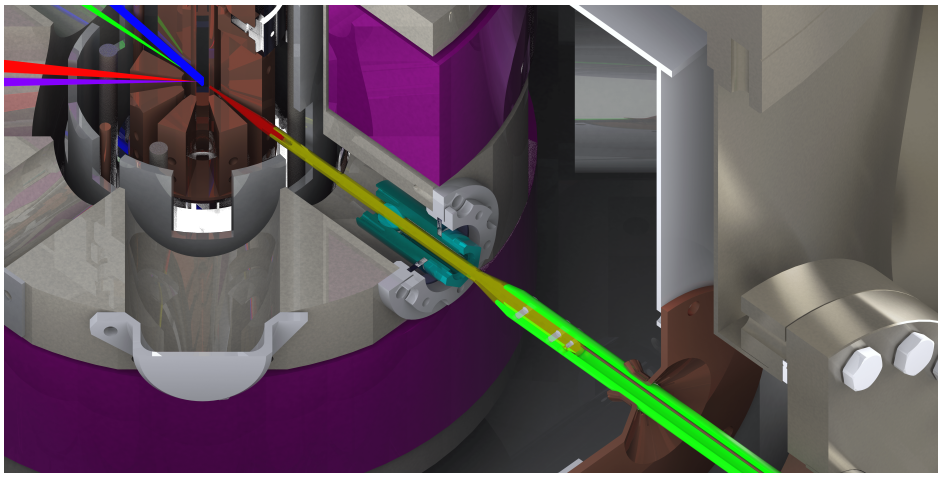

Figure 4.5: Depiction of the sample holder and its carrier system. The sample itself, i.e. the ablation target containing the desired element, might only be of microscopic quantities and can not be seen here. It is applied to the tip of the sample holder (red, titanium). This is then screwed into the sample carrier (yellow, copper), which is connected to an x-y-z manipulator (no longer visible in the picture) by a tube (green, fibreglass). A copper wire (brown) for contacting the sample carrier is housed inside the tube. The following components are installed for thermalisation with the various cooling stages: At 4 K, the sample carrier is guided inside a bronze sphere (light teal), which is screwed into a cylinder (teal). The other side of the cylinder is screwed into a sapphire ring to ensure thermalisation as well as electrical insulation. For the heat shield at 40 K, a sleeve made of copper springs (brown, around the green) is used.

The compounds used were tetraethyl lead $Pb(C_2H_5)_4$, chemical abstracts service registry number (CAS RN) 78-00- 2, and triphenyl bismuthine $Bi(C_6H_5)_3$, CAS RN 603-33-8. The latter one required heating, realised by a silicon-insulated constantan wire coiled around the chambers. Regulating the power supplies thus allows constant heating power, enabling a steady-state operation.

Chapter 5

Data acquisition

"Everything not saved will be lost"

—*Nintendo* [86]

The data for this work were taken through optical spectroscopy of ions trapped in electron beam ion traps (EBITs). Reflective diffraction gratings are used as dispersive elements. Gratings of different groove densities are used. Low densities $\sim 10^2\,\mathrm{mm}^{-1}$ are beneficial for taking overview spectra to build a general understanding of the electronic system in question. After that, higher density $\sim 10^3\,\mathrm{mm}^{-1}$ gratings are used for precision measurement. Multiple gratings are used since higher groove density results in higher resolution, but due to geometrical constraints, they are limited in the applicable wavelength range. In our set-ups, we refer to the low-density gratings as "coarse" and the high-density gratings as "fine", respectively. Measurements taken are called "coarse" and "fine" according to the grating used as well.

The data acquisition is performed by thermo-electrically cooled charge-coupled device (CCD) sensors. Temperatures as low as $-80\,^\circ\mathrm{C}$ reduce the dark current, allowing long acquisition times $t_{\mathrm{ac}} \sim 10^3\,\mathrm{s}$. The geometric calibration is accurate to $\approx 0.5\,\mathrm{nm}$ for the coarse gratings. This is sufficient for most overview scans, as, in our experience, the atomic code predictions are accurate to about 10 %, i.e. 20 nm to 80 nm. The fine gratings in use, on the other hand, span ranges of $\sim 10^1\,\mathrm{nm}$, and thus cover lines known to 0.5 nm precision.

For the fine measurements, however, accuracy is of the utmost importance. Instead of the geometrical calibration, the ion image is thus referenced

to the known spectrum of the calibration lamp. Typically, multiple calibration, ion and dark spectra are taken and combined afterwards. The repetition is needed due to the limited acquisition time caused by cosmic events and to allow the correction of thermal drifts in the optical system. Hollow-cathode lamps are used to fulfil the demands on strong, narrow line widths as a reference. They consist of a noble-gas atmosphere-protected metal cathode featuring the spectrum of the noble gas and metal elements, typically from the neutral atoms and singly charged ions. The elements are carefully chosen for the particular wavelength to feature *at least* four strong, *unambiguously identifiable* calibration lines. The calibration light is inserted into the optical pathway on a retractable high-reflective screen, at the location of an intermediate image, by an optical fibre.

As seen in the following chapters, additional vacuum ultraviolet (VUV) spectroscopy enables the connection of more electronic states through higher energy transitions. This was kept in mind for the design of the spectroscopy set-up at the free electron laser Hamburg EBIT (FLASH-EBIT). Essentially, this setup would enable simultaneous acquisition of optical, VUV, extreme ultraviolet (XUV) and even X-ray spectra. Cross-referencing these spectra would simplify the analysis, as for example the charge state distribution can now be inferred from wavelength range into another, or calculated more precisely thorough the combination of data from the different spectrometer. Since no VUV, XUV or X-ray data was evaluated for this work, it is only discussed insofar as it influences the layout of the system. More information about VUV spectroscopy at FLASH-EBIT can be found in ref. [87].

5.1 Optical setup at the HD-EBIT

The optical spectroscopy setup at the HD-EBIT is shown in fig. 5.1. Inside its magnet chamber, a system of fused silica lenses projects the ion spectra onto an intermediate image outside the chamber, passing a fused silica window. At this intermediate image, the retractable reflector, connected to the calibration lamp by optical fibre, is located. A periscope box is needed to turn the horizontal ion cloud image, matching the vertical spectrometer entrance slit. Lenses inside the periscope box image the intermediate image onto the entrance slit. One of them is movable to counter chromatic aberrations. In the *Czerny-Turner* spectrometer, two concave mirrors are used for projecting the entrance slit onto the CCD screen while collimating the light on the planar diffraction grating.

All data used in this thesis were taken with this setup. A more detailed description and characterisation can be found in ref. [88].

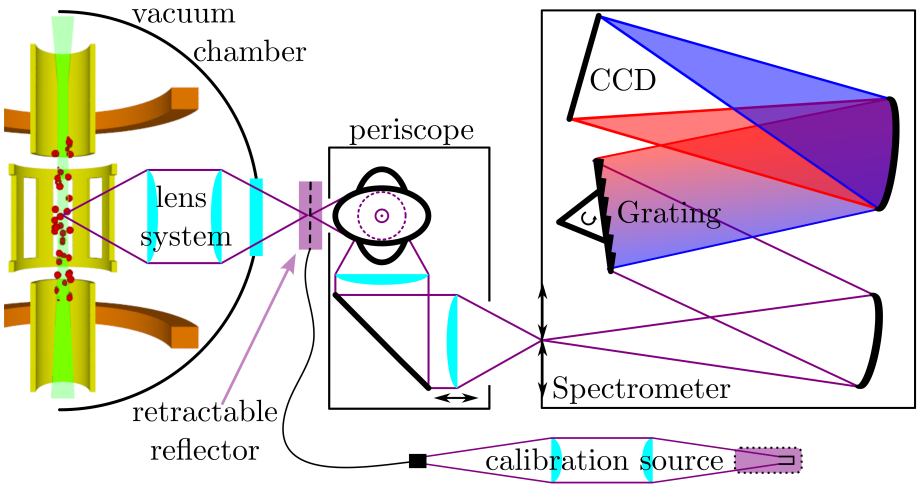

Figure 5.1: Schematic depiction of the HD-EBIT optical spectroscopy setup. The EBIT is to the left. The radiation originates from the ions (red), trapped by the electron beam (green) and the DTs (yellow). The slits in the central DTs allow the radiation to reach the lens system. After that, it leaves the vacuum chamber to form an intermediate image at the location of the retractable reflector. When in place, the reflector guides light from the calibration source into the periscope, otherwise the ions radiation enters. The periscope encompasses three mirrors and two lenses, turning the beam by 90° and refocusing it into the spectrometer. One of the lenses is moveable, as indicated by the two-sided arrow, to correct chromatic aberrations. In the spectrometer, two concave mirrors project the entrance slit onto the CCD. Between them, where the light is collimated, the reflection grating is located, inducing dispersion. Adapted from ref. [88].

5.2 Optical setup planned for the XUV-EBIT

For the extreme ultraviolet EBIT (XUV-EBIT), a simpler optical path is possible. Due to the small size of the Heidelberg compact EBITs (HC-EBITs), no optics inside the vacuum is necessary. A sapphire window, featuring transmission from 200 nm to 1 µm, is passed at the top of the trap. Then, an off-axis parabolic mirror collimates the light onto a plane mirror. After the plane mirror, a second parabolic mirror focuses the light again into the spectrometer's entrance slit. In the absence of an intermediate image, the calibration light is directly inserted into the pathway of the collimated light by a switchable mirror. Like the emission spectra, the calibration light is collimated by an off-axis parabolic mirror, preserving the achromatic nature of the optics.

As spectrometer, a 1.26 m Spex1269 Czerny-turner spectrometer was acquired from the Physikalisch-Technische Bundesanstalt in Braunschweig. While less accurate than the spectrometer at the HD-EBIT, it would be sufficient for most measurements. Lines demanding a very high accuracy will be supplemented with measurement at the HD-EBIT anyway, due to its higher magnetic field and hence larger Zeemann splitting.

5.3 Future optical for the FLASH-EBIT

The setup at FLASH-EBIT has been planned after the XUV-EBIT became unavailable for optical spectroscopy. It thus depends mainly on the same parts as the previously discussed design. Two additional off-axis paraboloids are positioned inside the vacuum to bridge the larger distance from inside the magnetic coils and traverse the heat shield. They are built around an aperture left for VUV radiation, as depicted in fig. 5.2. Their optical axis is thus skewed in the laboratory frame, allowing positioning of the optics outside the VUV pathway while using the same aperture at the 40 K stage. The unit of two off-axis parabolic mirrors essentially works like a biconvex lens, projecting the ion cloud onto an intermediate image just behind the aperture. A third off-axis parabolic mirror, located above the VUV pathway, reflects the light collimated out of the chamber through the sapphire window. The paraboloid is positioned at such an angle that the optical axis after it is horizontal in the laboratory frame to simplify adjustments.

Since the light leaves in the horizontal plane, like at HD-EBIT, a periscope is needed here as well. Otherwise, the optical set-up outside the vacuum is the same as planned for XUV-EBIT.

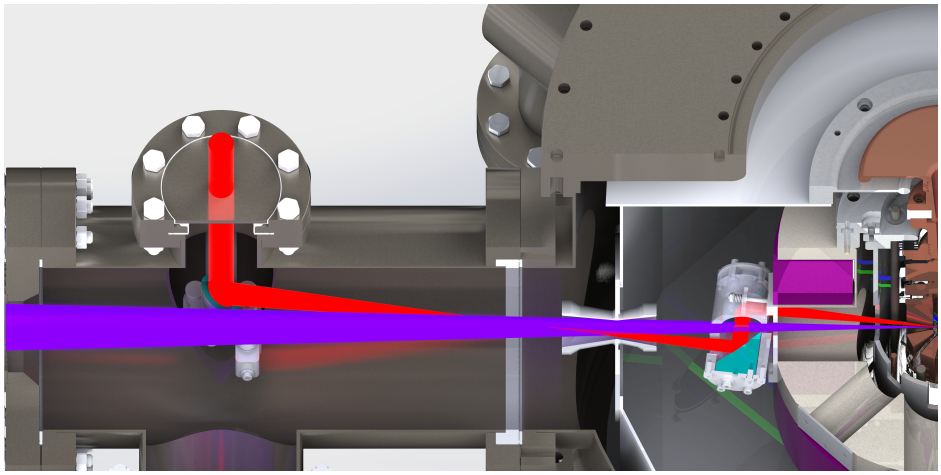

Figure 5.2: In-vacuum assembly of the FLASH-EBIT spectroscopy setup in the optical (red beam) and VUV (purple beam) range in cross-sectional view. The radiation originates in the ions trapped by the electron beam at the right edge of the image. The VUV radiation passes apertures of increasing size from right to left, continuing to the grating spectrometer. The first off-axis parabolic mirror in the optical pathway, at the top, is partially hidden by the mounting cylinder, which is made of solid aluminium but rendered translucent to show its inner workings. The optical axis is orthogonal – collinear – orthogonal to the mounding cylinder. Slightly after the 40 K aperture, an intermediate image is located, picked up by the third parabolic mirror.

5.4 Spectrography

5.4.1 McPherson spectrometer

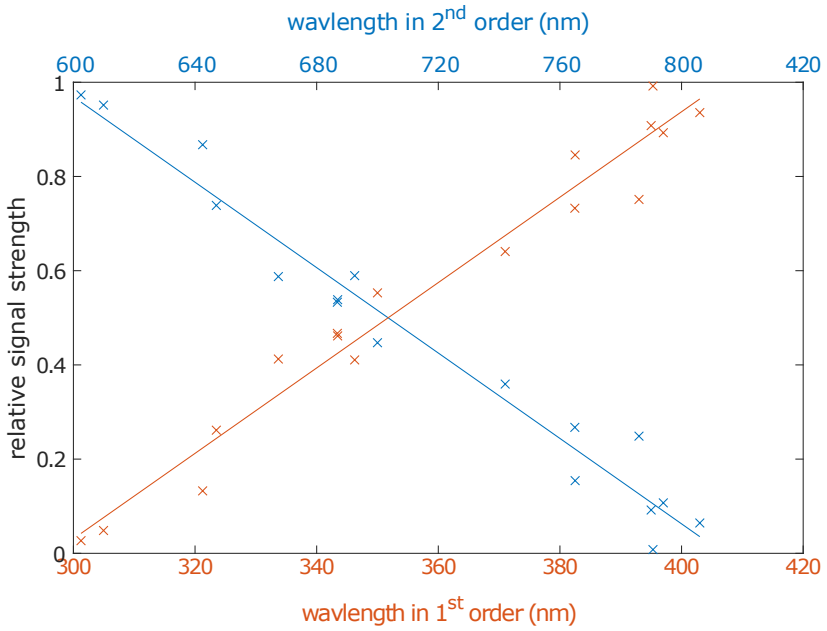

Figure 5.3: Determination of the effect of the 500 nm-*blazing* featured by the 150 mm^{-1} grating. Comparison of the relative signal strength of first and second-order measurements of the same spectral lines. Crosses show data points and lines of the linear regression. The orders closer to 500 nm get increasingly stronger. Below the intersection at $\approx$ 350 nm, the second-order measurements are stronger than their first-order, contrary to the typical diffraction-induced distribution.

The spectrometer used for this work was a 2 m "Model 2062" manufactured by McPherson. While it is sold with a variety of gratings, three are available for our experiment.

Firstly, the "coarse" 150 mm^{-1} grating, featuring a resolution of 40×10^{-3} nm and a dispersion of 3.32 $\mathrm{nm\,mm}^{-1}$, blazed at 500 nm, able to disperse spectra up to 1040 nm [89]. The blazing shifts the typical intensity distribution between different orders of interference, especially away from the zeroth order. The effect can be seen in fig. 5.3, where lines measured twice, in the first and the second order, are shown. The relative signal strengths $I_{\mathrm{rel},x}$ are shown, $I_{\mathrm{rel},x} = I_x(I_1 + I_2)^{-1}$, with the intensity $I_x, x \in 1, 2$ of the

x^{th} order. This way, transitions with different line strengths are comparable. The intersection is at $\approx 350\,\text{nm}$, transitions below that wavelength yield their strongest signal in the second order and transitions above that in the first. This intersection is $500\,\text{nm} - 350\,\text{nm} = 150\,\text{nm}$ from the blazing wavelength in the first order, and $2 \cdot 350\,\text{nm} - 500\,\text{nm} = 200\,\text{nm}$ from the second. This asymmetry presumably stems from the fact that the first order is naturally stronger than the second due to diffraction, which is superimposed on the blazing effect. Below $\approx 300\,\text{nm}$, no signal is anticipated, as the intensity is completely shifted into the second order. Aside from those special characteristics for lines below $\approx 400\,\text{nm}$, this type of grating benefits of increased efficiency close to the blazed wavelength.

Secondly, two "fine" gratings are provided. $3600\,\text{mm}^{-1}$ grating, featuring a resolution of $2 \times 10^{-3}\,\text{nm}$ and a dispersion of $0.14\,\text{nm}\,\text{mm}^{-1}$, able to disperse spectra up to 430 nm, and the $1800\,\text{mm}^{-1}$ grating, featuring a resolution of $4 \times 10^{-3}\,\text{nm}$ and a dispersion of $0.26\,\text{nm}\,\text{mm}^{-1}$, able to disperse spectra up to 860 nm, both holographic [89]. In contrast to blazed or ruled gratings, they feature low stray light [90] and a flat efficiency curve along their range, improving the signal-to-noise ratio (SNR). The highest wavelengths of those gratings can only be achieved using the so-called *extended mode*, where the grating has to be moved manually to a second position. This is only done in rare cases where a severe experimental benefit is gained. For most cases however, the $3600\,\text{mm}^{-1}$ grating is used up to 400 nm, the limit of the *"normal" mode*, and the $1800\,\text{mm}^{-1}$ grating above.

The spectrometers entrance slit is variable between 5 mm and 10 µm. A narrower entrance slit yields higher resolution and lower stray light. A too small slit, however, forms a diffraction pattern on the first mirror and, exceeding its bounds, reduces intensity without the anticipated gain of resolution. Ref. [91] has found a slit of 40 µm as the width for optimal resolution. This, however, requires *perfectly* aligned optics, strong lines and long integration times. Therefore, typically values of 60 µm to 100 µm are chosen for the experiments conducted in the course of this work.

5.4.2 Oxford Instruments Newton DU940P-BU2 CCD camera

The CCD camera that took all spectrographic images used for this work is a "Newton DU940P-BU2" from Oxford Instruments. It features a back-illuminated, 250 nm enhanced CCD sensor with 2048×512 active pixel (px), each $13.5\,\mu\text{m} \times 13.5\,\mu\text{m}$ in size, covering a $27.6\,\text{mm} \times 6.9\,\text{mm}$ image size with a 100 % fill factor. A pixel ($1\,\text{px} = 13.5\,\mu\text{m}$) is used as a unit of length

throughout this work. The chip is covered with an ultraviolet (UV)-grade fused silica window and thermoelectrically cooled down to −80 °C, reducing the dark current to $2 \times 10^{-3}\, e\, \mathrm{s}^{-1}$, per physical pixel, according to the manufacturer. The readout noise is rated at $2.5\, e$, per read-out pixel, for our operating conditions. [92].

Signal-to-noise ratio

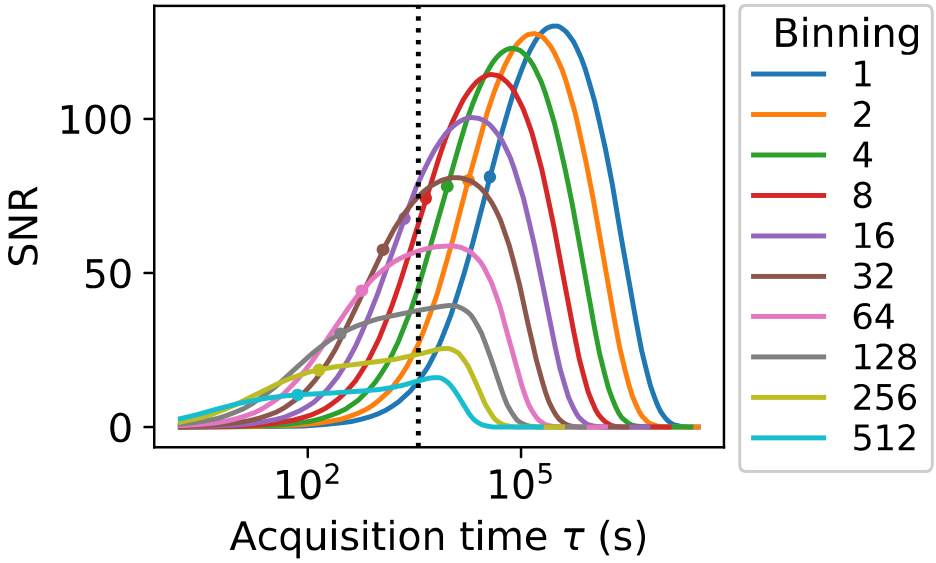

Figure 5.4: Approximation of the SNR for different y-binning and acquisition times. The acquisition time is on a logarithmic scale. Read-out noise, thermal noise and cosmic background radiation are taken into consideration. The dot on each curve represents $t_=$, where the contribution of thermal and read-out noise are equal. The binning $b_y = 16$ at $t_{\mathrm{ac}} = 30\,\mathrm{min}$ is indicated by the dashed line. Adapted from ref. [91].

Our camera is mounted with the long sensor side parallel to the optical plane, this is called the x-direction. The other side of the sensor, the y-direction, is perpendicular to the optical plane. Thus, the 2048 px correspond to different wavelengths, while the 512 px are typically averaged to yield an intensity-wavelength plot. While this "average" is replaced with an intricate process for the high precision achieved in this work, a simple mean is a close enough approximation for the considerations in this chapter.

The signal to be detected thus spans a rectangular area on the sensor, covering a section in the x-direction and all pixels in the y-direction, i.e. $\sigma_x \times 512\,\mathrm{px}$ for a linewidth σ_x. The total signal S, given in e, is therefore

$$S = t_{\mathrm{ac}} i_S \sigma_x 512\,\mathrm{px} \tag{5.1}$$

with the acquisition time t_{ac} and a signal intensity i_S, including all efficiencies, e.g. given in $e\,\mathrm{s}^{-1}\,\mathrm{px}^2$.

It needs to exceed the flat readout noise

$$N_{\mathrm{ro}} = \frac{2048}{b_x}\frac{512}{b_y} 2.5\,e \tag{5.2}$$

$11\,e$ per pixel bin, with x- and y-bin sizes, b_x and b_y, and the time-dependent thermal noise, also known as dark current,

$$N_{\mathrm{th}} = t_{\mathrm{ac}} \cdot 2048 \cdot 512 \cdot 0.0003\,e\,\mathrm{s}^{-1} \tag{5.3}$$

The acquisition time is free to choose, as long as it stays above 0.02 ms, as a read-out frequency above 50 kHz results in higher read-out noise. The bin sizes, telling how many physical pixels form a read-out pixel, are constraints to integer divisors of the sensor size, $b_x = 2^n, n \in \mathbb{N}_0, n < 12$ and $b_y = 2^n, n \in \mathbb{N}_0, n < 10$, ensuring divisibility. For spectroscopy purposes, binning in the dispersive direction is uncommon, as it reduces resolution, i.e. $b_x = 1$, while b_y is generally to choose.

Both, S and N_{th} are linear in t_{ac}. A longer t_{ac} can therefore only reduce N_{ro}, awakening interest in $t_=$, where $N_{\mathrm{th}} = t_{\mathrm{ac}}$, marking the point from which thermal noise exceeds read-out noise:

$$t_= = \left(\frac{2048}{b_x}\frac{512}{b_y} 2.5\,e\right) \div \left(2048 \cdot 512 \cdot 0.0003\,e\,\mathrm{s}^{-1}\right) \tag{5.4}$$

$$= \frac{2.5\,e}{0.0003\,e\,\mathrm{s}^{-1} b_y} \approx 8333 \frac{\mathrm{s}}{b_y} \tag{5.5}$$

Choosing $t_{\mathrm{ac}} > t_=$, and rounding up to convenient values, this results in *minimum* acquisition times for typical binning:

1 $t_{\mathrm{ac}} > 140\,\mathrm{min}$

2 $t_{\mathrm{ac}} > 70\,\mathrm{min}$

4 $t_{\mathrm{ac}} > 35\,\mathrm{min}$

8 $t_{\mathrm{ac}} > 17.5\,\mathrm{min}$

16 $t_{\mathrm{ac}} > 9\,\mathrm{min}$

32 $t_{\mathrm{ac}} > 4.5\,\mathrm{min}$

The *typical* acquisition times are above those values, as this reduces the overall noise by lowering the read-out noise. For example, $b_y = 16$ and $t_{\mathrm{ac}} = 30\,\mathrm{min}$ was used for lead precision measurements.

Only considering the CCD noise, the highest possible binning of $b_y = 512$ and acquisition time t_{ac} would be the clear decision if it were not for high energetic cosmic background radiation. Due to the high energetic and random energy nature, such a signal recorded on the CCD sensor must be removed before averaging along the y-direction. As physical pixels affected are summed into read-out pixels before any treatment can take place, the whole read-out pixel is affected and must be discarded. Also, more pixels are affected at longer acquisition times. Therefore, it is of utmost importance to find a balance between y-binning and acquisition time, as an increase reduces thermal noise but worsens the effect of cosmic background radiation. Ref. [91] did measurements in order to quantify the cosmic events occurring at this setup; compare fig. 5.4. While the global optimum is $b_y = 1$ and $t_{\mathrm{ac}} \approx 145 \times 10^3\,\mathrm{s} \approx 40\,\mathrm{h}$, such long acquisition times are unsuitable in reality. First of all, with the large number of measurements needed and the high operational cost of the setup, especially the liquid helium consumption, such an operation would not be economical.

Additionally, thermal drifts occur within a day cycle, shifting the images up to $\Delta_x \approx 0.83\,\mathrm{px}$ [91], resp. $0.000\,52(2)\,\mathrm{nm}$[88]. For this work, an algorithm to consider this thermal shift, at least in the first order, was developed, relying on multiple calibration measurements during a day cycle. This limits the time between calibration measurement and, thus, individual image acquisition time to about $\approx 4\,\mathrm{h}$. It further calls for an average over multiple ion images instead of one long exposure, reducing the individual images acquisition time t_{ac} for the same total exposure time of the line in question. After deciding on t_{ac}, keeping at as high as reasonable, the appropriate binning according to the diagram is chosen.

5.4.3 Spectral range

The spectral range covered by this setup is effectively limited by the achievable SNR.

At higher wavelengths, the black body radiation of the heated cathode vastly increases the background noise, setting in at about $\approx 800\,\mathrm{nm}$. Additionally, the CCDs quantum efficiency decreases here, from 60 % at 800 nm

to below 10 % at 1000 nm, reducing the measurement signal [92]. Thus, only extraordinarily strong lines could be measured there. Typically, the range between 800 nm and 860 nm is only examined if a strong line is suspected there, which was not the case for this work.

At low wavelengths, the noise contributions do not differ from the main range. However, due to photon absorption from oxygen molecules in the optical pathway, signal below ≈ 250 nm gets increasingly absorbed with decreasing wavelength. Due to the blazing of the coarse grating, lines below 300 nm are recorded in their second order. Thus, lines found between 400 nm and 600 nm lead to additional measurements at half their registered wavelength with the fine gratings. Purging the whole optical path with nitrogen would increase the spectral range, allowing for measurements as low as 185 nm [89].

The combination of the CCD sensor size and then gratings dispersion gives a spectral range covered by an individual image. They are 91.8 nm for the 150 mm^{-1}, 3.9 nm for the 3600 mm^{-1} and 7.2 nm for the 1800 mm^{-1} grating respectively. Thus, the discussed geometric overview accuracy of 0.5 nm is sufficient to cover a line, even with the 3.9 nm range of the 3600 mm^{-1} grating.

Chapter 6

Measurement-transition attribution process

"Physics is to be regarded not so much as the study of something *a priori* given, but rather as the development of methods of ordering and surveying human experience."

—*Nils Bohr* [93]

The experimental setup described in the previous chapters delivers data of mainly one type: Two-dimensional monochromatic spectroscopic images recorded by a charge-coupled device (CCD) sensor and associated database files with acquisition and device parameters. In this chapter, we will first give an explanation of how images get processed into datasets in section 6.1. Section 6.2 is concerned with so-called *overview* measurements, a series of low-accuracy high-range spectra taken at many different electron beam energies and spread over the whole optical wavelength range. Its main purpose is finding lines of interest and establishing an electron-beam-energy to charge-state-distribution relation. Section 6.3 finally covers the evaluation process of high-accuracy single-line measurements, including the process of attributing the measured lines to the calculated electronic level structures. A more technical overview of the data taken is found in appendix A.

6.1 Analysis of spectroscopic images

To convert the raw spectroscopic images, e.g. figs. 6.1 and 6.3, to one-dimensional arrays of data, which in turn can be calibrated, the following steps are executed:

1. Removal of cosmic background radiation artefacts, section 6.1.1
2. Evaluation of projection curve, section 6.1.2
3. Thermal drift correction, section 6.1.3
4. Composition of the projection section 6.1.4

Each step is presented in its corresponding section. Typically, a set of images is taken at a given wavelength without movement of the grating. This includes multiple images of the ion cloud at the same or varying energies, background images with an emptied trap, and calibration images.

6.1.1 Removal of artefacts

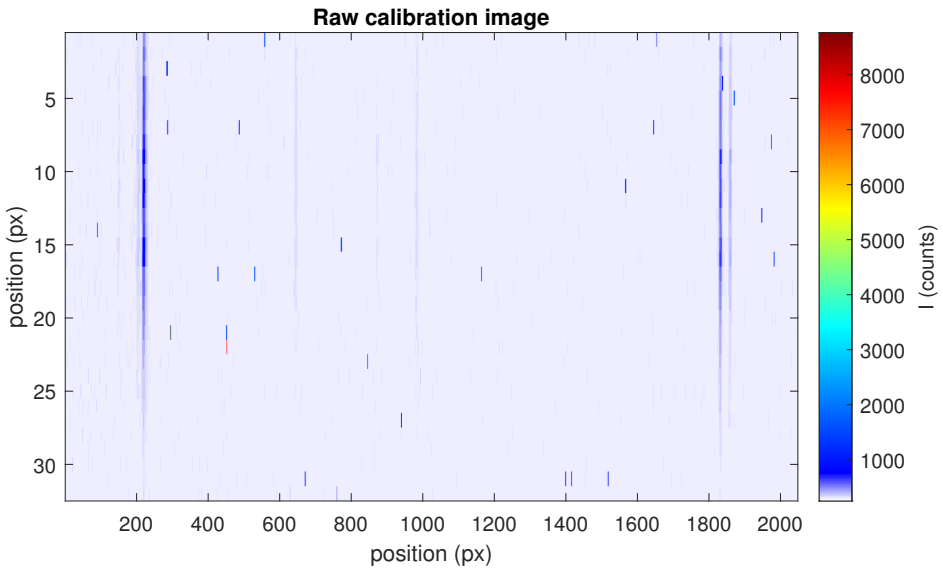

Figure 6.1: Example of a raw calibration measurement. The high-intensity artefacts stem from cosmic background radiation and need to be removed.

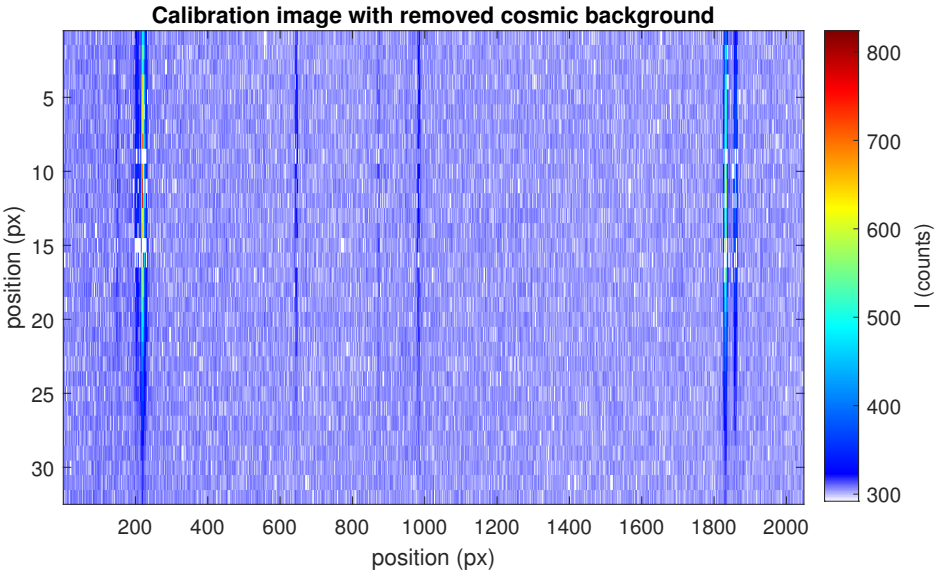

Figure 6.2: Same calibration measurement as in fig. 6.1, after the removal of cosmic background radiation. Removed values are shown in white.

Cosmic background radiation refers to events caused by high energetic background radiation recorded on the CCD sensor. The difficulty arising from cosmic rays has already been taken into consideration regarding the choice of acquisition time. These events are not entirely preventable and must be removed after the fact. This type of radiation reaches the sensor, not through the spectrometer, penetrating the camera housing or stray light screen instead. Their path is thus out of square regarding the measured lines and the sensor. Thus, the recorded events are either localized spots or inclined traces, in the rare case of particle movement in the sensor plane. Due to their high energy, the count rate of these events exceeds the spectroscopy signal distinctly in most cases.

As artefacts from cosmic background radiation are random events, their exact contribution can not be determined, and all affected pixels must be omitted for further analysis. The first measure against them is thus limiting the acquisition time. The second remedy is discarding images with too much contamination through Cosmic background radiation, e.g. in the rare case of a ray traversing the whole image. The third method is used against a minor quantity of localised spots.

Here, an algorithm based on the one presented in ref. [94] is used for detection. It forms a histogram of the image, or partitions thereof, and identifies

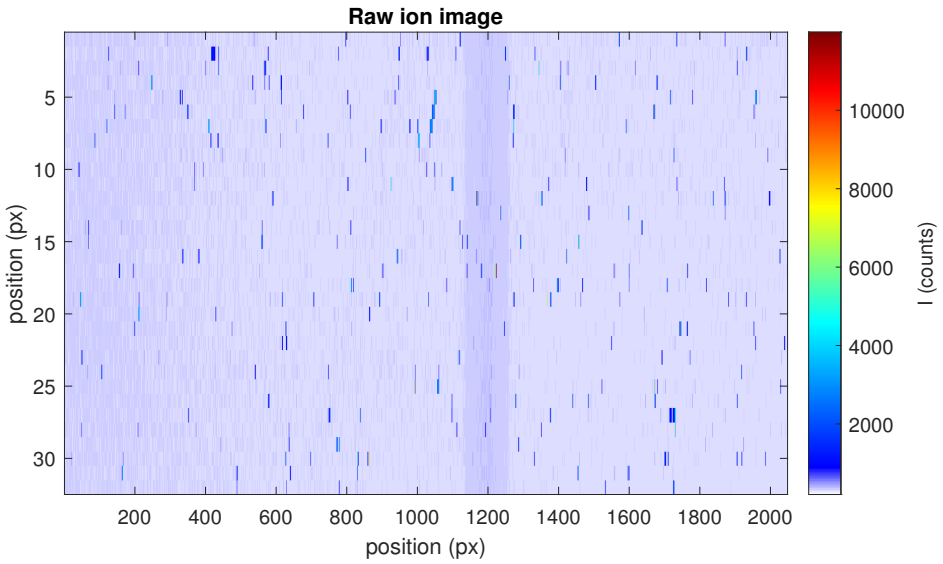

Figure 6.3: Example of a raw ion measurement. The high-intensity artefacts stem from cosmic background radiation and need to be removed.

the pixels with the highest count rates as "cosmic". This may be tweaked in several ways, e.g., demanding a certain gap in the histogram between signal and removed events, discarding the top x per cent of the distribution, or even setting a fixed threshold for removal. Additionally, the bins used to make the histograms also influence the outcome. The removed values are replaced by "nan" – not a number – and are thus not considered in the following arithmetic operations: They are left out for fits and averages of multiple images; as a result individual pixels may be the average of different number of values, depending on the coinciding Cosmic background radiation events. Another approach is to replace them with an average of the surrounding pixels, thus not changing the mean values but delivering a more robust, less arithmetically constrained data set.

6.1.2 Evaluation of projection curve

Different optical aberrations, like coma and astigmatism, distort the projection of the entrance slit onto CCD camera. Additionally, the pixels of the CCD are not perfectly aligned with the entrance slits direction. Therefore, the two-dimensional dataset cannot be projected into a one-dimensional array by simply averaging in a pixel direction. Instead, a projection curve is

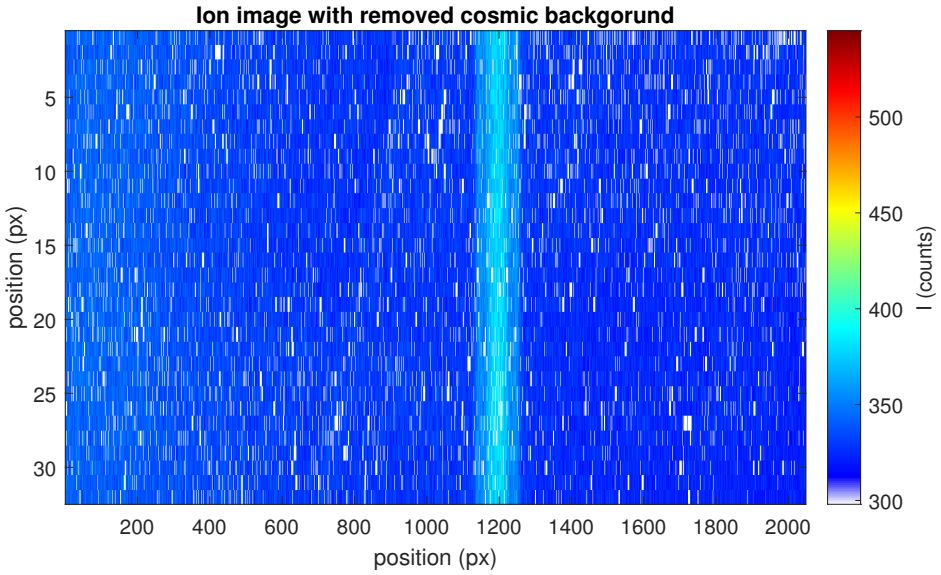

Figure 6.4: Same ion measurement as in fig. 6.1, after the removal of the cosmic background radiation signals. Removed values are shown in white.

determined by a two-dimensional fit of strong lines with the function

$$f(x,y) = A \cdot \exp\left(-\left(\frac{x-(m(y-y_0)^2+b(y-y_0)+c)}{\sigma_x}\right)-\left(\frac{y-y_0}{\sigma_y}\right)^2\right)+d, \tag{6.1}$$

representing a two-dimensional Gaussian of widths σ_x, σ_y and intensity A, with a y-position y_0 and the x-position slanted by a second-degree polynomial featuring the parameters m, b and c. Typically, multiple chosen lines are fitted simultaneously, each with their individual x-position c_i and intensity A_i, and shared remaining parameters. Due to the increased intensity, shorter acquisition time, and thus less noise, as well as fewer removed "comics", the calibration images are used to do so. A different angle of the grating leads to different optical aberrations; hence, a different projection curve is produced for each set of measurements. More details can be found in ref. [91].

6.1.3 Thermal drift correction

Finding a balance between cosmic events, thermal noise and background noise, acquisition times between 10^3 s and 10^4 s have proven to be beneficial. Additionally, the multiple images taken for each set of measurements further

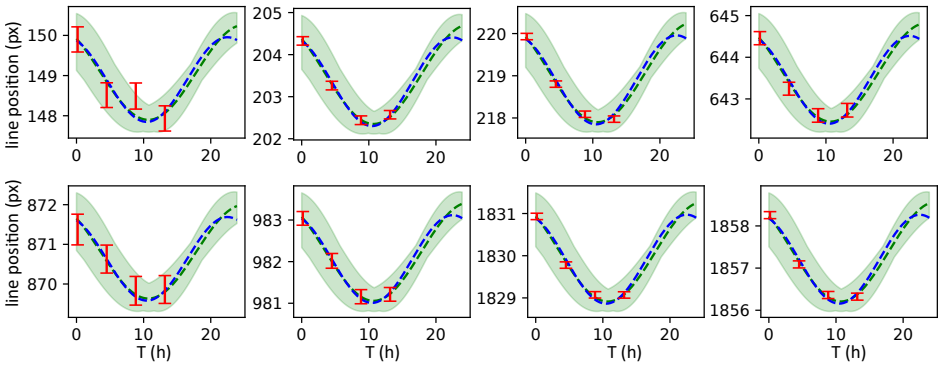

Figure 6.5: Example of a thermal correction fit. Each subplot is a separate calibration line. Temporal drifts of calibration lines are shown in red. The fitted functions from eq. (6.3) (blue) and eq. (6.2) (green) are dashed. The green shaded area gives the confidence bounds of the fit from eq. (6.2) since it was more accurate and thus used in this case.

increase the timespan images of one set are taken. With that time spanning multiple hours, the thermal drift follows a day cycle, as shown in refs. [88, 91], which needs to be considered. Thus, multiple calibration pictures are taken throughout the set and spread out between the other images. The positions x_i of the i strongest lines are determined for each calibration image by fitting the lines with a Gaussian after performing the line projection. Combining the timestamps t_{st} and acquisition times t_{ac}, the mean point in time of acquisition t_{pit} can be calculated by $t_{\mathrm{pit}} = t_{\mathrm{ac}} + t_{\mathrm{st}}$ for each image. As a result, multiple t_{pit}-x diagrams, one for each line, can be compiled from the calibration images, each yielding a data point. Choosing a fit function appropriate to the given dataset approximates the temporal behaviour of x to counteract the shift. The following functions have been used for this work,

$$f(t) = A \cdot \sin(\omega(t - t_0)) + p_i \tag{6.2}$$

$$f(t) = A \cdot \sin\left(\frac{2\pi}{24\,\mathrm{h}}(t - t_0)\right) + p_i \tag{6.3}$$

$$f(t) = m \cdot t + p_i \tag{6.4}$$

with decreasing degrees of freedom. Equations (6.2) and (6.3) feature a common amplitude A and the phase shift t_0. Equation (6.2) has the frequency ω as free parameter, while it is fixed to match a day cycle in eq. (6.3). In the fixed case, an uncertainty of $0.05\,\mathrm{h}^{-1}$ was assigned to ω, corresponding

to a variation of about three hours. This is consistent with the evaluation in ref. [88, 91] and the successfully determined ω in the course of this work. The linear function eq. (6.4) uses the slope m. In all three eqs. (6.2) to (6.4), the individual mean positions p_i are featured. There is one for each of the i calibration lines chosen, stating their position on the image separated from the shift $\Delta x = f(t)$.

The choice of function depends on the number of calibration images, the total duration covered by them, and, in rare cases, the section of the day cycle covered. Thus, the function chosen may vary with each measurement set, even when featuring the same acquisition parameters. The function with the least uncertainty but reasonable result is chosen. For this work, the functions in eqs. (6.2) and (6.3) are compared for each set of data. An example is shown in fig. 6.5. Due to its large associated uncertainty, a fixed ω is only used in cases where ω can not be properly determined from the data points. After determining the parameters, the shift Δx is calculated for each image of the set and applied to the cosmic background radiation-corrected, two-dimensional images.

6.1.4 Composition of the projected data

Before projecting, an average of all "dark" images, spectroscopic images of an empty trap, are subtracted from each ion image. The next step is to project these images into one-dimensional datasets. Naturally, the data at this point can not match with the initial integer pixels anymore: Even a slope as a projection curve would lead to sub-pixel shifts, and a higher-degree polynomial, as in our case, even more so. The thermal corrections shift the images in fractional units of pixels relative to each other as well. Thus, a new array with fractional pixels is created to best fit the projection function. To calculate the corresponding projection, the average of all ± 0.5 px surrounding sub-pixels along the projection function of all images after the thermal shift is applied is taken for each entry. An average has the advantage, e.g. over a sum, that is delivers robust and comparable results, even for a varying amount of input values. This is of utmost importance here, as the projection function covers a lower number of pixels at the images edges, the thermal shift additionally changes the input-count, and the removed Cosmic background radiation events additionally lower the quantity of inputs randomly. The averages of "dark" images of an empty trap are then subtracted from those of the images containing the signal of interest. This typically results in four arrays – a set of calibration arrays and a set of ion image arrays, each consisting of a sub-pixel and an intensity array. The thus projected data from the images in figs. 6.1 to 6.4 are shown in figs. 6.6 and 6.7. The single-pixel

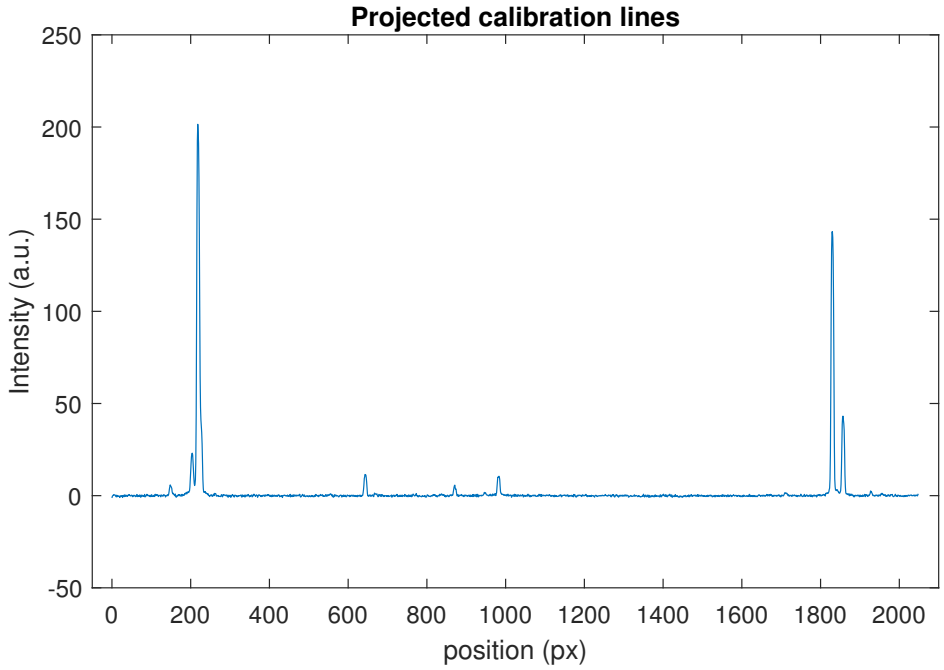

Figure 6.6: Curved projection of the calibration data shown in figs. 6.1 and 6.2.

outliers that can be seen typically stem from lower-energy cosmic background radiation, which is too weak to be removed and contributes to measurement accuracy akin to noise. This includes the negative one at $\approx 800\,\mathrm{px}$ in fig. 6.7, where it impaired one of the background images.

6.2 Evaluation of the overview spectra in Lead

An exception to the aforementioned four arrays per measurement set is energy scans. Here, multiple ion images at different electron beam energies, i.e., with different charge state distributions, are taken at each wavelength. As those spectra are supposed to be different, they are not averaged among each other but rather stacked up to yield a two-dimensional array of intensities for different wavelengths and electron beam energies, respectively. Additionally, they are typically taken with the coarse grating, producing multiple sets at distinct wavelengths spread over the visible range, comprising all lines of interest visible by this setup. The infra-red unfortunately vanishes below the black-body-radiation background. The ultraviolet, on the other hand, can be measured; however, the 500 nm blazing featured by the coarse grating in

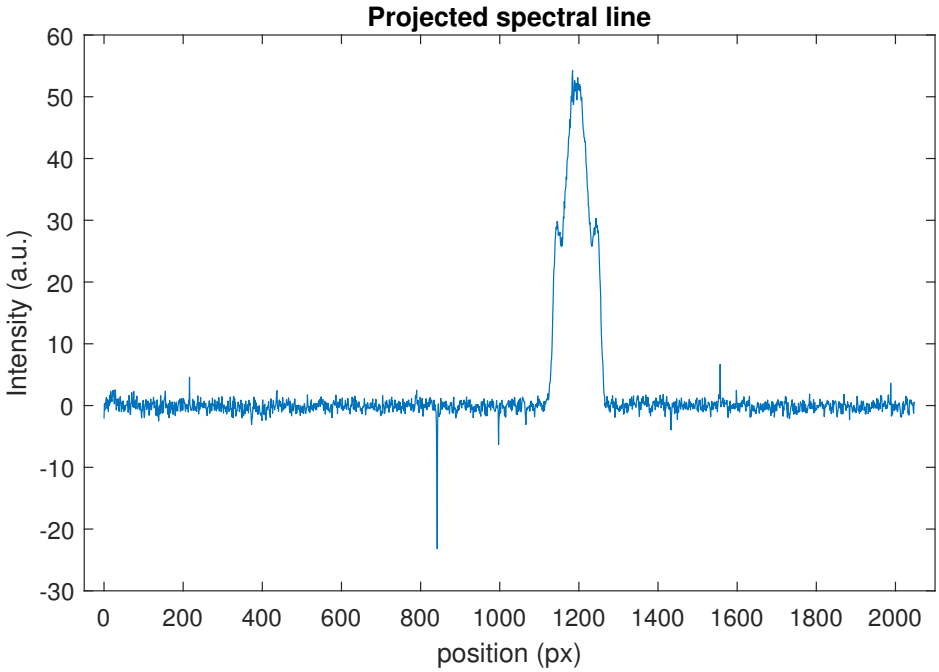

Figure 6.7: Curved projection of the ion data shown in figs. 6.3 and 6.4. The Zeeman structure is distinctly visible. Individual, small, single-pixel deviations can be seen as well.

use bundles the intensity of different orders of interference. Orders closer to 500 nm have thus enhanced signal strengths. The distinction can be easily verified by measuring the half wavelength, as only second-order lines yield a signal there. Therefore, for this work, a scan range of 300 nm to 800 nm was used, choosing the lowest covered wavelength $\lambda = 300\,\mathrm{nm}$, with $|500\,\mathrm{nm} - 300\,\mathrm{nm}| = 200\,\mathrm{nm}$ further away from the optimal wavelength than its second order $2\lambda = 600\,\mathrm{nm}$, with $|500\,\mathrm{nm} - 600\,\mathrm{nm}| = 100\,\mathrm{nm}$. The upper limit needs to be chosen to cover the maximal measurable wavelength, as fractional interference orders do not exist.

This data has two purposes. Firstly, it gives the information at which wavelengths and beam energies lines can be found, consequently enabling fine-line measurements. Secondly, these scans – typically encompassing multiple different charge states – can be deconstructed into charge state associated wavelength-overviews, enabling the attribution of charge states to measured lines using the synthetic spectra, given by `FAC`, of the ions of interest.

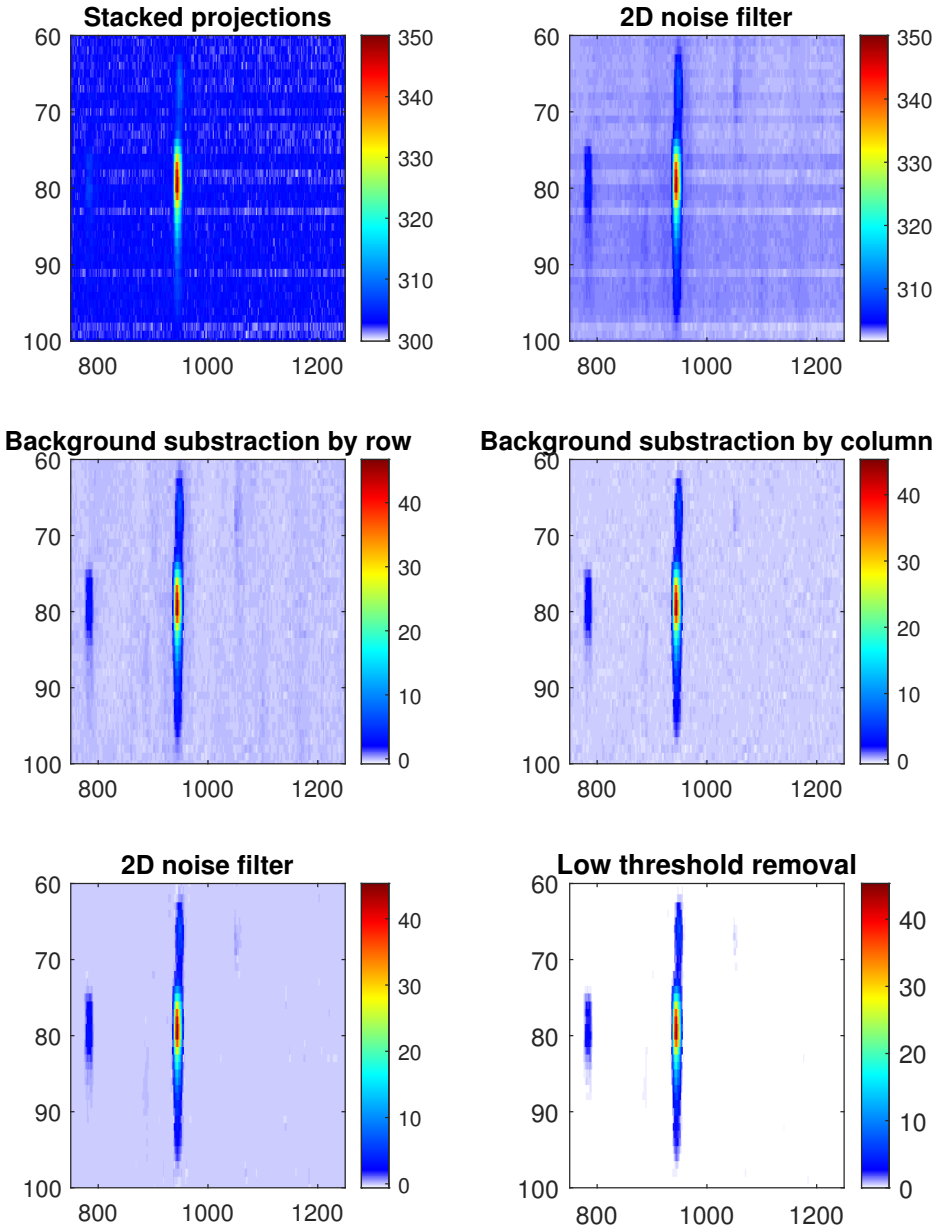

Figure 6.8: Illustration of the preprocessing steps taken. Each image is the input for the next step, starting with the stacked projections on the top left. The order is top-left, top-right, centre left, centre right, bottom left, bottom right. Since these steps are performed as image processing, the axis is shown in image pixels px here. The ordinate represents different energies, while the abscissa represents different wavelengths.

6.2.1 Preprocessing of the spectra

After these measurements are done, their projection into one-dimensional datasets is carried out for the different beam energies, respectively. The pixels are converted into wavelengths from geometric parameters of the spectrometer and grating. Linear corrections are applied to shift and stretch the wavelength axis to match the same lines in the overlap region of adjacent wavelength ranges, averaging the wavelength of both recordings. Stacking the resulting data up, treating the energies as an additional axis, yields two-dimensional wavelength-energy spectra for each wavelength range. These spectra feature great irregularities, especially between different energies and noise, as seen in fig. 6.8. While these deviations are not necessarily problematic for a manual consideration, we want to separate the charge state with a method called *non-negative matrix factorisation (NNMF)*, as explained in section 6.2.2. This algorithmic charge state separation requires preprocessed data. The image-processing steps to optimise the wavelength-energy spectra are shown in fig. 6.8.

First, a non-local mean two-dimensional de-noising algorithm is used, essentially smoothing the picture by calculating weighted averages. Then, a background spline is fitted for each row and subtracted, removing background fluctuations for different energies. Equally, the background fluctuations for different wavelengths are removed by subtracting column-wise fitted background splines. The added noise in the lines from removing the background in a grid pattern is then removed by using the non-local mean de-noising algorithm again. Knowing most pixels are only showing noise, and all relevant signal is much stronger, all pixels with a value below the images total average are then set to zero. The resulting sparse matrix, which is only non-zero for the lines of interest, has proven the ideal input for NNMF. Any artefacts, systematic shifts or increased uncertainties emerging from this process are acceptable, as the aim is a general understanding of the date *before* a rigorous series of precise measurements and evaluation follows.

6.2.2 Non-negative matrix factorisation

Non-negative matrix factorisation (NNMF) is an algorithm to factorize an $n \times m$ matrix $\mathbf{S}$ into an $n \times k$ matrix $\mathbf{N}$ and a $k \times m$ matrix $\mathbf{I}$. All three matrices are entirely non-negative. Generally, the resulting matrices are a lower rank approximation $\mathbf{N} \cdot \mathbf{I} \approx \mathbf{S}$, reducing the quadratic deviation $\sum_{i,j}(\mathbf{S} - \mathbf{N} \cdot \mathbf{I})^2_{ij}$. [95].

In a physical sense, a wavelength-energy overview-spectrum is composed of two separate distributions: The abundance $N_{\mathrm{q}}(E_{\mathrm{beam}})$ of ions of charge q

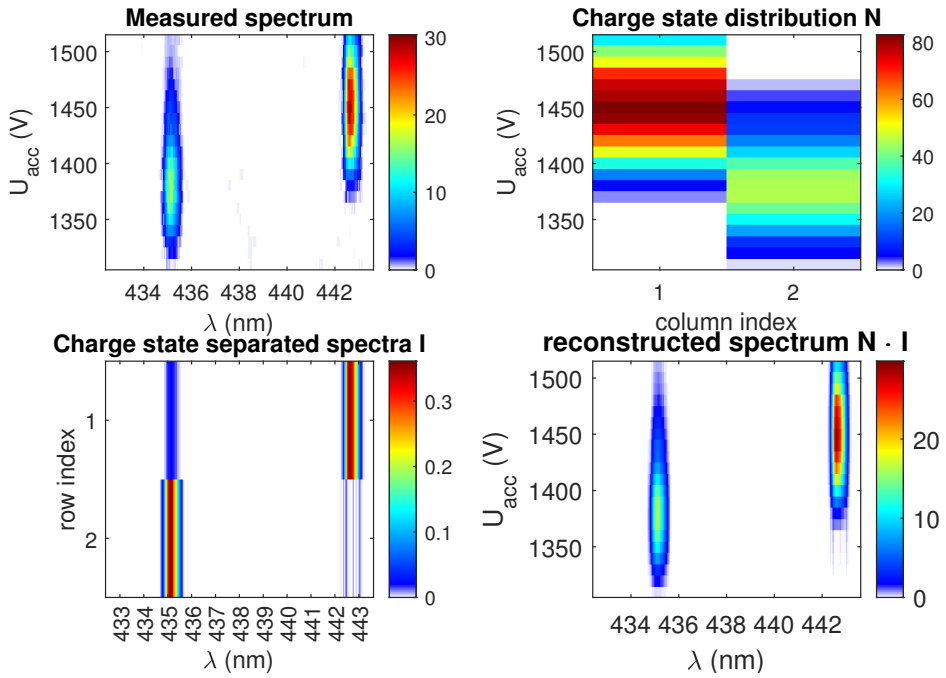

Figure 6.9: Illustration of the separation of spectra using NNMF. Since two charge states are involved, $k = 2$ has been chosen. The measured spectrum, top-left, has been successfully separated into the ion-specific spectra, bottom left, and the energy-dependent charge state distribution, top-right. Matrix multiplication yields the reconstructed spectrum, bottom right, where the key features of the initial input are clearly retained.

at different energies E_{beam} and the the emission spectrum $I_{\mathrm{q}}(\lambda)$ at different wavelengths λ. The complete spectrum then is given by the sum over the multiplication for all charge states,

$$S(E_{\mathrm{beam}}, \lambda) = \sum_{\mathrm{q}} N_{\mathrm{q}}(E_{\mathrm{beam}}) I_{\mathrm{q}}(\lambda) \tag{6.5}$$

Discretisation, as for the n steps of an energy scan and m sensor pixels of a wavelength measurement, transform the functions N_{q} and I_{q} into arrays of length n and m respectively. Composing the arrays of the k relevant charge states yield the $n \times k$ matrix $\mathbf{N}$ and the $k \times m$ matrix $\mathbf{I}$, where the total spectrum is given by the $n \times m$ matrix $\mathbf{S} = \mathbf{N} \cdot \mathbf{I}$. Hence, the entire physical information of interest can still be contained in the lower-rank approximation of the factorisation.

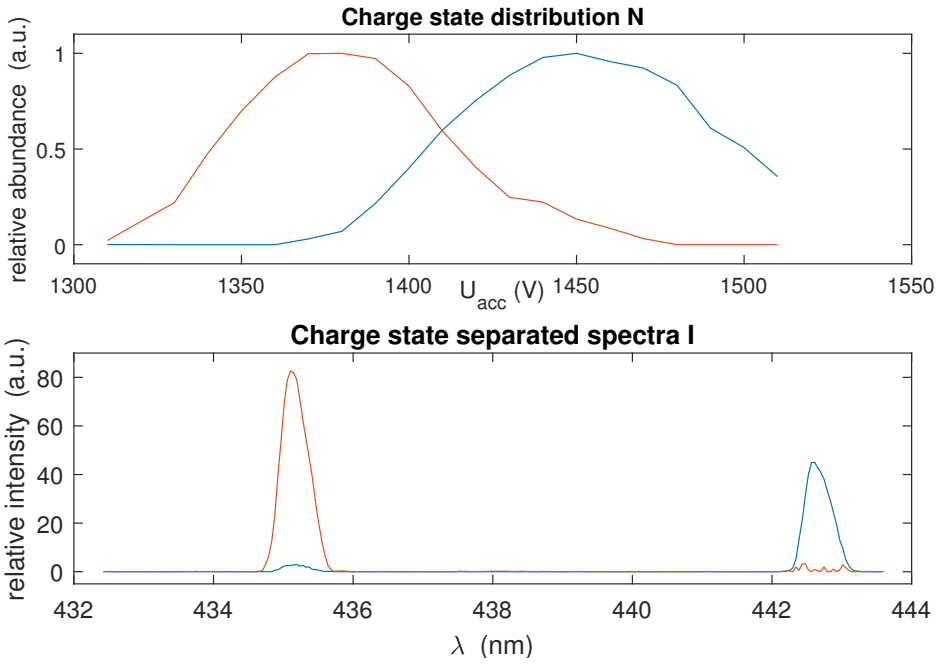

Figure 6.10: Charge state separated spectra resulting from NNMF. The top shows the charge state distribution for different acceleration voltages U_{acc}, while the bottom shows the optical lines occurring from those charge states. Line colours indicate the same charge state. The small signals at the respective other spectral lines, most prominent at 435 nm, stem from inaccuracies in the separation.

The application of NNMF on the preprocessed data is illustrated in fig. 6.9, where a small section, only containing two lines, has been factorised. The two lines feature different intensities. Mathematically, any constant factor c can be multiplied to any row in $\mathbf{I}$, without changing $\mathbf{S} = \mathbf{N} \cdot \mathbf{I}$, if the corresponding column in $\mathbf{N}$ is in turn multiplied by c^{-1}. This degree of freedom is overcome algorithmically by setting $\max(\mathbf{I}_{i*}) = 1 \ \forall\, i \leq k$ and calculating $\mathbf{N}$ accordingly. Here $*$ is used as a place-holder to note a vector spanning all possible indices, e.g. here $j \leq m$, thus the entire i^{th} row. In the physical view, however, the equality of the resulting matrices is not given. Instead, we *assume* that, at their respective optimum electron beam energy, the maximal abundance of ions of charge q is equal. Therefore

$$\mathbf{I}'_{l*} = \max(\mathbf{N}_{*l}) \cdot \mathbf{I}_{l*} \ \ \forall\, l \leq k \tag{6.6}$$

and

$$\mathbf{N}'_{*l} = \frac{\mathbf{N}_{*l}}{\max(\mathbf{N}_{*l})} \ \forall\, l \leq k \tag{6.7}$$

is calculated, ensuring

$$\max(\mathbf{N}'_{*l}) = 1 \ \forall\, l \leq k. \tag{6.8}$$

Applying this to the example in fig. 6.9 yields the spectra shown in fig. 6.10. In the lower plot, showing the individual ions spectra, the comparability of line intensities between both lines is retained. At the same time, the change in charge state distributions at the top follows the expectation.

The overview datasets for multiple wavelengths have been created with the same beam energies. Thus, a single matrix $\mathbf{N}$ is sufficient to describe all measurement sets. The matrices $\mathbf{I}_\lambda$, on the other hand, are sections of the whole measured range. Lining up the datasets, creating a big $m \times o \cdot n$ matrix from the o datasets thus matches the physical reality best. Performing a single NNMF on the big matrix thus yields better results than performing multiple factorisations for the sections, as this way, the common charge state distribution is adjusted to fit all measured lines simultaneously.

The parameter k needs to be chosen carefully to match the number of charge states present. A too-small k leads to charge states pooled together, while a too-big k separates single charge states into two spectra. Finding lines from metastable states by increasing k and thus assigning them a separate distribution seems possible for small energy steps but has not been tried for this work. Instead, k was chosen to be slightly smaller than the expected quantity of charge states: Due to the varying electronic structure from state to state, the anticipated, and likewise measured, intensity of the strongest line in a given ions spectra spans several orders of magnitude. Therefore, statistical fluctuations of the strongest lines of the brightest charge states exceed the total line strengths of "darker" states. To reduce the mean deviation, it is more beneficial to separate the brighter state to accommodate those fluctuations than to match the weak lines. A k small enough to avoid this was chosen.

A solution would be a separation of the big matrix into matrices with fewer rows, featuring a section of the charge state but still spanning the whole wavelength range, performing multiple NNMF. Fortunately, the "darker" states treated in the course of this work feature a low number of lines, so they can easily be picked by hand.

6.3 Attribution of transitions

From the results of the NNMF, we know the ideal electron beam energy for a certain charge state by looking at the maximum of **N**, as well as the corresponding approximate wavelengths and intensities from **I**. This is enough information to perform high-precision measurements with the fine grating.

Due to the blazing of the coarse grating at 500 nm, all lines in **I** between 400 nm and 600 nm are measured at λ and $\lambda/2$, to cater for second order lines. Generally, performing both measurements is favourable, as in rare cases, two lines, one in first, the other in second order, may overlap in the coarse scan. The lower limit $2\lambda = 400\,\mathrm{nm}$ is chosen, as photons below 200 nm are absorbed before reaching the CCD. The upper limit $2\lambda = 600\,\mathrm{nm}$ is picked, as the overview scan starts at $\lambda = 300\,\mathrm{nm}$ and, as a consequence, measures those lines twice, in the first and second order, already. So, including each occurrence in the overview once also results in two fine measurements. After comparison, the lowest order where a line occurs is evaluated.

For the evaluation of a high-precision measurement, the data set is processed, according to section 6.1, for the calibration and ions, respectively, including the best possible thermal drift correction. Then calibration lines are identified using the geometric calibration and known transition from the National Institute of Standards and Technologies standard reference data (NIST data) [83]. Each identified calibration line is fitted, typically with a Gaussian or a set of Gaussians. This has proven to be the most robust method to evaluate the central wavelength for a line, even if they are quite weak or overlapping. Various different methods have been tried during the course of this work. These deviations are typically $\approx 0.005\,\mathrm{px}$, systematic and are hence listed as a systematic wavelength uncertainty $\Delta\lambda_{\mathrm{sys}}$. It mainly changes between measurement sessions when different slit widths at the spectrometer are used.

This results in a pair of nm - px values for each calibration line. A 2^{nd} order polynomial is fitted to these values. The resulting function translates the ion spectrum from the image position in pixels into an intensity-wavelength diagram. Using the photon energy $E = hc\lambda^{-1}$, with the Planck constant h and the speed of light c, gives an intensity-energy diagram, which is beneficial for the inclusion of the Zeeman components, which are symmetrical in E, as given in eq. (2.21). The sum over all components, using their relative intensities given in eq. (2.22), give the function

$$f\big(E_0, \sigma, I_0, I_\pm, g_{J,\mathrm{i}}, g_{J,\mathrm{f}}, c\big) = c + \sum_k I_k\big(I_0, I_\pm\big) \cdot G\Big(E_0 + \Delta E_k\big(B_{\mathrm{ext}}, g_{J,\mathrm{i}}, g_{J,\mathrm{f}}\big), \sigma\Big) \tag{6.9}$$

which readily describes the present data with the following parameters:

E_0 mean energy of the transition, free parameter.

σ width of each Zeeman component, free parameter.

I_0 & $I_\pm$ joint intensity of the middle (0) and outer ($\pm$) Zeeman components, free parameter.

$g_{J,\mathrm{i}}$ & $g_{J,\mathrm{f}}$ Landé g-factor (g-factor) of the initial (i) and final (f) state respectively. Free or fixed parameter.

k index of the individual Zeeman component

c constant for background compensation

I_k Function to calculate the individual intensities from the joint intensities, compare eq. (2.22)

ΔE_k Function to calculate the energy shifts from the g-factor, compare eq. (2.21). $B_{\mathrm{ext}} = 8\,\mathrm{T}$

The quantity of individual lines k to be considered is governed by the m_J of the initial and final state and, thus, by the total angular momentum J of the two involved energy levels. Thus, to perform a Zeeman fit, a corresponding transition candidate has to be found *beforehand*. They are chosen according to their expected wavelength, from AMBiT, and their expected intensity, from the `FAC` based collisonal radiative model (CRM). In some cases, more than one candidate was present. In those cases, multiple Zeeman fits have been conducted to confirm or discard them. For those fits, $g_{J,\mathrm{i}}$ and $g_{J,\mathrm{f}}$ are fixed with the values given by AMBiT instead of free parameters, delivering a more distinctive line shape. To accurately determine the mean energy E_0, a fit with free g-factor is conducted for every line as well.

Chapter 7

Level structure reconstructions

"Da steh' ich nun, ich armer Tor,
Und bin so klug als wie zuvor!"
"And here, at last, I stand, poor fool!
As wise as when I entered school;"

—*Faust* [96]

For this work, spectra of two elements, lead (Pb) and bismuth (Bi) were taken. The lead spectra cover partially filled f-shells, in particular from $[Kr]4d^{10}4f^{3}$ in Pb XXXIV to $[Kr]4d^{10}4f^{13}5s^{2}$ in Pb XXII. Here, the abbreviation $[Kr] = 1s^{2}2s^{2}2p^{6}3s^{2}3p^{6}3d^{10}4s^{2}4p^{6}$ analogous to the National Institute of Standards and Technologies standard reference data (NIST data) is used. The bismuth spectra on the other hand covers partially filled d-shells, in particular from $[Xe]4f^{14}4d$ in Bi XV to $[Xe]4f^{14}5d^{6}$ in Bi X. Again, the abbreviation $[Xe] = 1s^{2}2s^{2}2p^{6}3s^{2}3p^{6}3d^{10}4s^{2}4p^{6}4d^{10}5s^{2}5p^{6}$ is used analogous to the NIST data.

The overview spectra of all desired charge states were taken using the coarse $150\,\mathrm{mm}^{-1}$ grating and an acceleration voltage step size of 10 V. The acceleration voltage range covered for lead was 600 V to 2000 V, for bismuth 80 V to 500 V. The lines of interest were remeasured with a fine grating, $3600\,\mathrm{mm}^{-1}$ for $\lambda \leq 400\,\mathrm{nm}$, and $1800\,\mathrm{mm}^{-1}$ for $\lambda > 400\,\mathrm{nm}$ respectively, yielding sub-pm precision. While the higher grooves density grating has a higher resolving power, it is unfortunately unable to cover the whole range of interest.

The systematic deviations of $\Delta\lambda_{\mathrm{sys}} \approx 0.005\,\mathrm{px}$ are listed at the precision measurements, translated into nm by the respective calibration curve. All parameter uncertainties from the fits are propagated to yield the statistical uncertainty $\Delta\lambda_{\mathrm{stat}}$. Hence, for each precision measurement, the statistical uncertainty $\Delta\lambda_{\mathrm{stat}}$ and the systematic uncertainty $\Delta\lambda_{\mathrm{sys}}$ is given. The calculated Zeeman-structure, from J_{i}, J_{f} and the Landé g-factor (g-factor), matches the given lines within the assumed calculation uncertainties, except for the lines marked p for as of now only preliminarily identified. In these cases, either the spectral resolution or the calculation accuracy was insufficient to confirm the assignment unambiguously. Definitely unfitting line identifications, however, have been rejected.

The ion temperature has been investigated by the 392 nm transition of Pb XXI, which features only three distinctly resolved Zeeman components. This allows an accurate linewidth determination on which the temperature approximation is based: Fitting a Gaussian profile, the width depends on our instrumental resolution and the Doppler broadening arising from the ion temperature. This combined line width was $\sigma_{\mathrm{com}} = 8.092(25) \times 10^{-5}\,\mathrm{eV}$. Fitting a calibration line, the instrumental resolution can be determined, as it is mainly broadened by the finite instrumental resolution and thus much narrower due to a *comparatively* low temperature. This comparison is shown in fig. 7.1. The calibration linewidth was determined as $\sigma_{\mathrm{calib}} = 2.986(43) \times 10^{-5}\,\mathrm{eV}$. Subtracting that, the resulting linewidth $\sigma_{\mathrm{ion}} = \sigma_{\mathrm{com}} - \sigma_{\mathrm{calib}} = 7.521(31) \times 10^{-5}\,\mathrm{eV}$ gives an upper limit for the ion temperature $T = mc^2 k_b^{-1} (\sigma_E/E)^2 = 1.273(10)\,\mathrm{MK}$, where the mass of the ion is m, the speed of light c and the Boltzmann constant k_b.

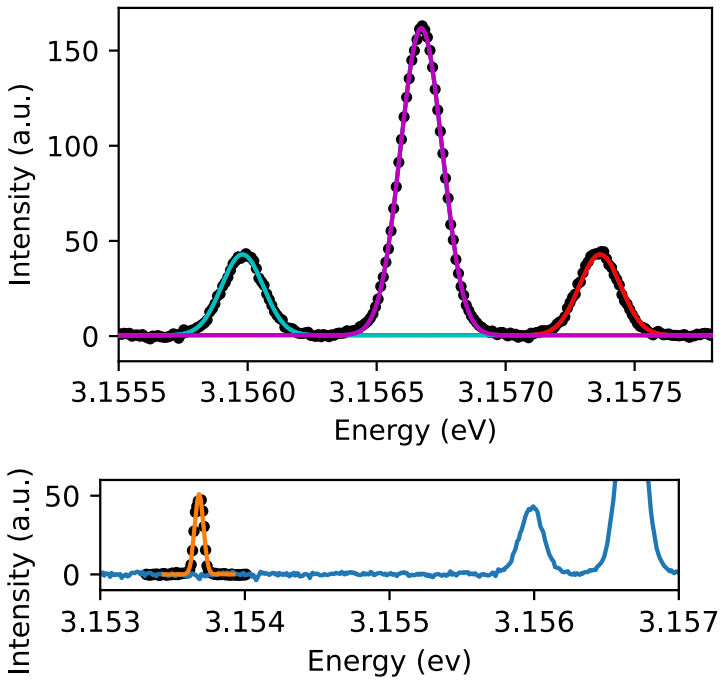

Figure 7.1: Top: Fit of the $1 \rightarrow 0$ line of Pb XXXI at $\lambda = (392.657\,39 \pm 0.000\,26 \pm 0.000\,06)\,\mathrm{nm}$, with the value given as $\lambda \pm \Delta\lambda_{\mathrm{stat}} \pm \Delta\lambda_{\mathrm{sys}}$. The change in total angular momentum J, $1 \rightarrow 0$, leads to only three Zeeman components, shown in cyan, purple and red. The large initial g-factor $g_i \approx 1.5$ results in a clear separation of those components. Details on the transitions are in table 7.10 . Bottom: Comparison of the calibration linewidth comparison (fit orange, data black) and the Pb XXXI ion signal (blue), used to approximate the ion temperature $T \approx 1.27(1)\,\mathrm{MK}$. Reprinted from ref. [97].

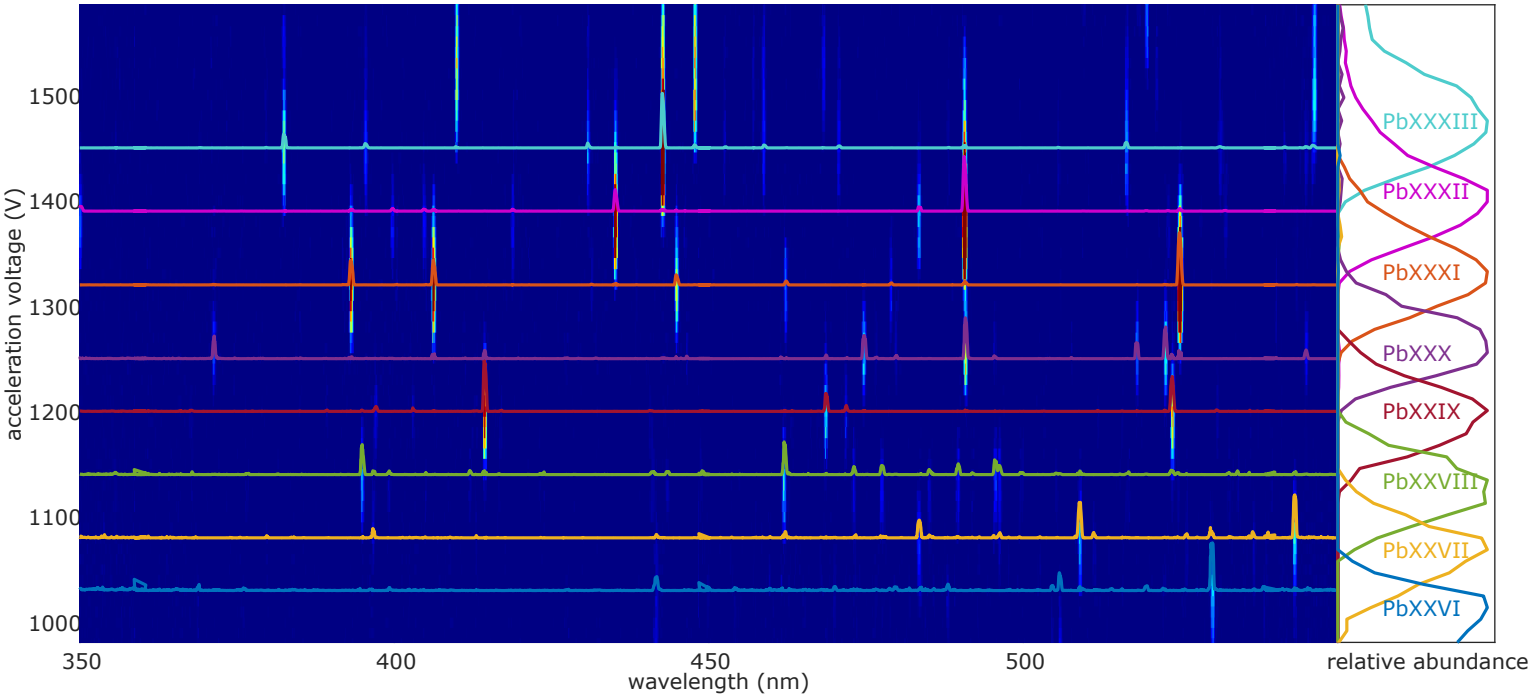

Figure 7.2: Overview of the measured lead lines in between 550 nm and 800 nm, with the separation by NNMF. The two-dimensional spectrum is shown in the background. The intensity distribution **I** is superimposed row-by-row, with the baseline of each charge state raised to the U_{acc} of its maximal abundance. The charge state distribution **N** is shown column-by-column at the right. The corresponding charge states from Pb XXVI to Pb XXXIII are colour-coded. Pb XXXIV transitions, while not part of the NNMF separation, can be seen in the spectrum in the background at $U_{\mathrm{acc}} \approx 1550\,\mathrm{V}$. Adapted from ref. [97].

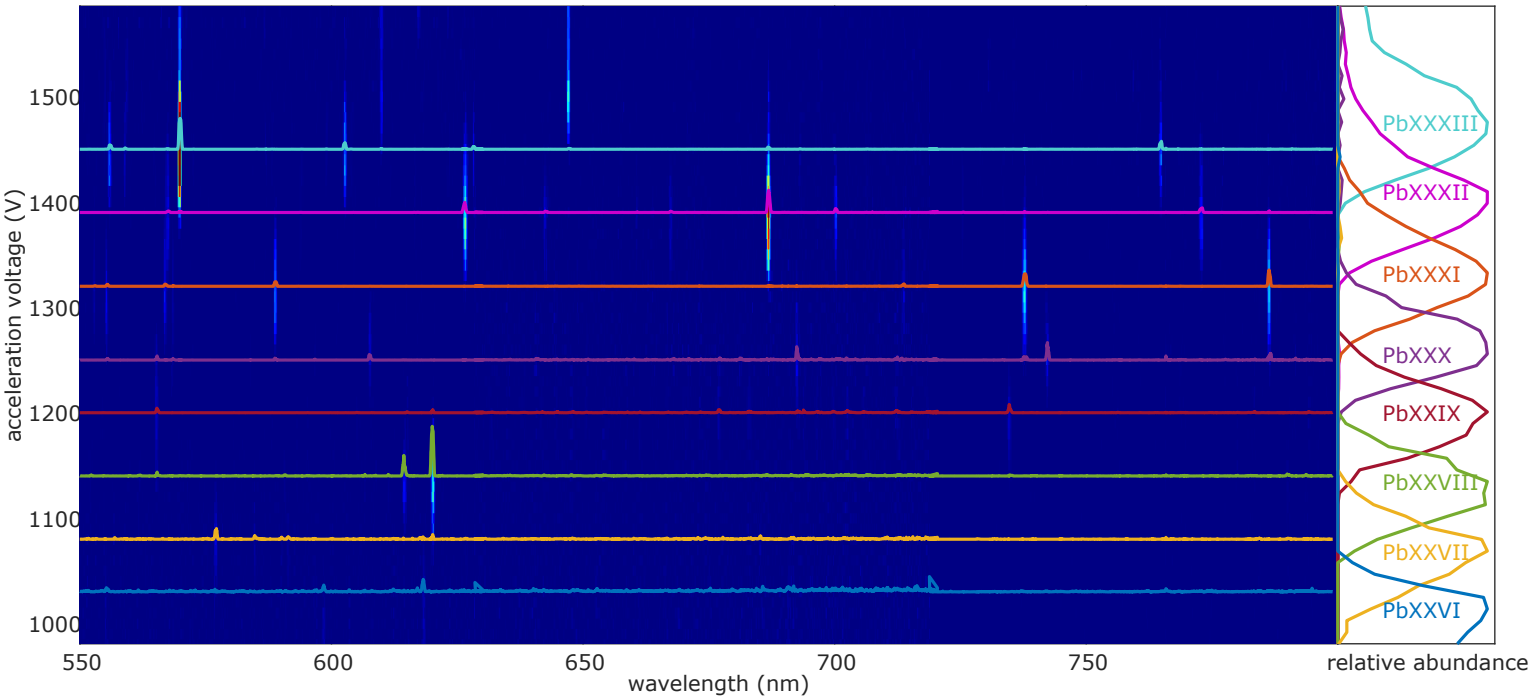

Figure 7.3: Overview of the measured lead lines in between 550 nm and 800 nm, with the separation by NNMF. The two-dimensional spectrum is shown in the background. The intensity distribution **I** is superimposed row-by-row, with the baseline of each charge state raised to the U_{acc} of its maximal abundance. The charge state distribution **N** is shown column-by-column at the right. The corresponding charge states from Pb XXVI to Pb XXXIII are colour-coded. Pb XXXIV transitions, while not part of the NNMF separation, can be seen in the spectrum in the background at $U_{\mathrm{acc}} \approx 1550\,\mathrm{V}$. Adapted from ref. [97].

7.1 Lead

The overview spectrum from lead can be seen in figs. 7.2 and 7.3. The charge states and their spectra have been separated from the two-dimensional image using NNMF. A comparison of the predicted lines with those separated leads to an identification of the charge states. Adjacent charge states in the NNMF must also correspond to adjacent charge states in the simulation. The following lines clearly point to a charge state identification:

Pb XXVI $U_{\mathrm{acc}} \approx 1030\,\mathrm{V}$

530.0(5) nm predicted at 269(27) nm, 2nd order (O.) 568(54) nm

Pb XXVII $U_{\mathrm{acc}} \approx 1080\,\mathrm{V}$

543.2(5) nm predicted at 277(28) nm, 2nd O. 554(55) nm

Pb XXVIII $U_{\mathrm{acc}} \approx 1140\,\mathrm{V}$

620.5(5) nm predicted at 318(32) nm, 2nd O. 638(64) nm

Pb XXIX $U_{\mathrm{acc}} \approx 1200\,\mathrm{V}$

414.1(5) nm predicted at 433(43) nm

523.9(5) nm predicted at 578(58) nm

Pb XXX $U_{\mathrm{acc}} \approx 1250\,\mathrm{V}$

346.4(5) nm **&** 692.5(5) nm predicted at 355(36) nm, 2nd O. 710(71) nm

371.4(5) nm **&** 741.8(5) nm predicted at 403(40) nm, 2nd O. 806(81) nm

Pb XXXI $U_{\mathrm{acc}} \approx 1320\,\mathrm{V}$

393.0(5) nm **or** 406.2(5) nm predicted at 427(43) nm,

524.7(5) nm predicted at 543(54) nm

738.0(5) nm predicted at 736(74) nm

The other charge states must follow accordingly due to succession. From the overview spectra,

Pb XXXII $U_{\mathrm{acc}} \approx 1390\,\mathrm{V}$

Pb XXXIII $U_{\mathrm{acc}} \approx 1450\,\mathrm{V}$

Pb XXXIV $U_{\mathrm{acc}} \approx 1550\,\mathrm{V}$

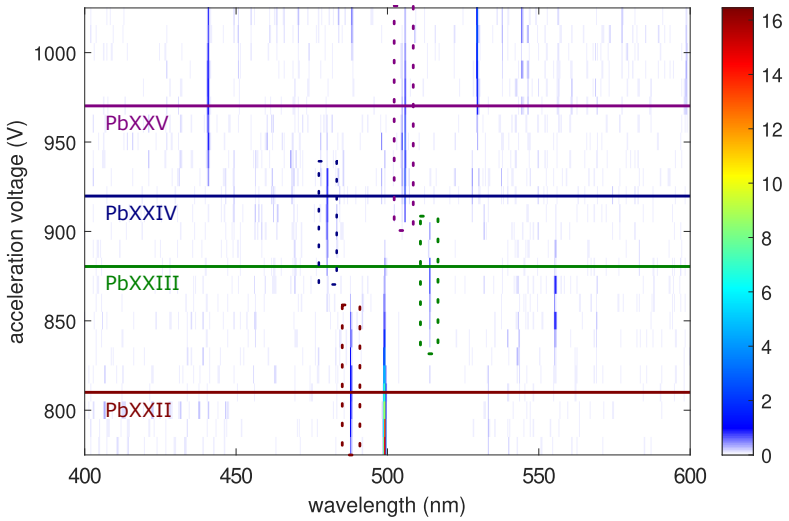

Figure 7.4: Section of the overview scan that shows the weak lines of the lower charge states. The lines are marked in dotted boxes. Horizontal lines mark U_{acc} of the respective highest abundance. The strongest shown line, just below 500 nm, spans a wide range of beam energies and stems clearly not from lead.

follows for higher charge states.

The lower charge states feature only very weak lines. They have not been plotted in figs. 7.2 and 7.3, as they would have vanquished at the present colour scale. Instead, they can be found in fig. 7.4. Here, their optimal voltages can be found at

Pb XXV $U_{\mathrm{acc}} \approx 960\,\mathrm{V}$

Pb XXIV $U_{\mathrm{acc}} \approx 920\,\mathrm{V}$

Pb XXIII $U_{\mathrm{acc}} \approx 880\,\mathrm{V}$

Pb XXII $U_{\mathrm{acc}} \approx 810\,\mathrm{V}$

A comparison with the ionisation energies E_{ion} in the NIST data, e.g. 610 eV for Pb XXII until 1430 eV for Pb XXXIV corroborates this identification further: The beam energy E_{beam} is generally smaller than the acceleration voltage. Also, the electron impact ionisation (EII) cross-section sets in at E_{ion} and increases for higher E_{beam}. Both effects lead to a maximum of abundance at a U_{acc} above E_{ion}, agreeing with the present identification.

For these thirteen stated lead ions, magnetic dipole transitions between 240 nm and 800 nm were found; 28 of those have been identified, with an additional preliminary identification. Eleven of the identified lines were ground

state transitions. For the about half field f-shells, specifically Pb XXIX to Pb XXXIV, many more lines connecting other states were identified. The charge states, with their measured lines and calculation parameters, are now discussed in more detail. An overview of those results can also be found in tables A.2 and A.3.

Table 7.1: Observed wavelength λ of an optical, magnetic dipole (M1) transition in Pb XXII. Wavelength uncertainties are given as statistical uncertainty ($\Delta\lambda_{\mathrm{stat}}$) and a systematic uncertainty ($\Delta\lambda_{\mathrm{sys}}$). The initial ($\mathrm{L_i}$) and final ($\mathrm{L_f}$) levels are given, as well as the initial (J_i) and final (J_f) total angular momenta. Calculations with AMBiT include the calculated wavelength λ_A, the g factor of the initial (g_Ai) and final (g_Af) level. Relative intensities I_F from the CRM are given. Reprinted from ref. [97].

$\mathrm{L_i} \to \mathrm{L_f}$	$J_\mathrm{i} \to J_\mathrm{f}$	$\lambda(\Delta\lambda_{\mathrm{stat}})(\Delta\lambda_{\mathrm{sys}})$(nm)	λ_A(nm)	I_F	g_Ai	g_Af
$1 \to 0$	$5/2 \to 7/2$	243.64949(154)(8)	244	3.18	0.86	1.14

Pm-like Pb XXII The NIST data states $[\mathrm{Kr}]4\mathrm{d}^{10}4\mathrm{f}^{13}5\mathrm{s}^2$ as the electronic ground state configuration of Pb XXII [83]. In contrast, we found $[\mathrm{Kr}]\ 4\mathrm{d}^{10}4\mathrm{f}^{14}\ 5\mathrm{s}^1$ with both, `FAC` and AMBiT.

Accordingly, the following parameters were used in our calculations:

`FAC`

Core configuration

$[\mathrm{Kr}]4\mathrm{d}^{10}$

Configuration used for radial optimisation

$4\mathrm{f}^{14}5\mathrm{s}^1$

Shell configurations used for configuration interaction (CI)

$4\mathrm{f}^{14}5\mathrm{s}^1$

$4\mathrm{f}^{14}5\mathrm{p}^1$

$4\mathrm{f}^{14}5\mathrm{d}^1$

$4\mathrm{f}^{13}5\mathrm{s}^2$

$4\mathrm{f}^{13}5\mathrm{s}^1 5\mathrm{p}^1$

AMBiT

Ground state configuration

$[\mathrm{Kr}]\,4d^{10} : 4\bar{f}^{6}4f^{8}5s^{1}$

Leading configurations

$4f^{14}5s^{1}$

$4f^{13}5s^{2}$

Number of considered electron excitations: 2

Number of considered hole excitation: 1

The ground-state of Pb XXII, [Kr] $4d^{10}4f^{14}$ $5s^{1}$, is only comprised of a single level, with a total angular momentum $J = 1/2$. The next higher level, in the [Kr] $4d^{10}4f^{13}5s^{2}$ configuration, has a total angular momentum of $J = 7/2$ and is thus metastable, featuring a $\Delta J = 3$ transition as direct connection to the ground state. Thus, the measured transition takes place inside the [Kr] $4d^{10}4f^{13}5s^{2}$ configuration, between the first and second excited level. More details on the transition are given in table 7.1. The `FAC` gives an energy $E \approx 38\,\mathrm{eV}$ above the ground state for the metastable state. Therefore, no interesting optical ground state transitions are anticipated for this ion.

Table 7.2: Observed wavelength λ of an optical, magnetic dipole (M1) transition in Pb XXIII. Continuation of table 7.2, reprinted from ref. [97].

$L_i \rightarrow L_f$	$J_i \rightarrow J_f$	$\lambda(\Delta\lambda_{stat})(\Delta\lambda_{sys})$(nm)	λ_A(nm)	I_F	g_{Ai}	g_{Af}
$1 \rightarrow 0$ p	$3 \rightarrow 4$	256.86064(107)(8)	214	1.13	1.04	1.25

p: preliminary identification

Nd-like Pb XXIII The NIST data states $[\mathrm{Kr}]4d^{10}4f^{13}5s^{1}$ as the electronic ground state configuration of Pb XXIII [83]. In contrast, we found $[\mathrm{Kr}]4d^{10}$ $4f^{14}$ with both, `FAC` and AMBiT.

Accordingly, the following parameters were used in our calculations:

`FAC`

Core configuration

[Kr]

Configuration used for radial optimisation

$4d^{10}4f^{14}$

Shell configurations used for CI

$4d^{10}4f^{14}$

$4d^{10}4f^{13}5s^{1}$

$4d^{10}4f^{13}5p^{1}$

AMBiT

Ground state configuration

$[\mathrm{Kr}]\,4d^{10} : 4\bar{f}^{6}4f^{8}$

Leading configurations

$4f^{14}$

$4f^{13}5s^{1}$

Number of considered electron excitations: 2

Number of considered hole excitation: 1

The ground-state of Pb XXIII, [Kr] $4d^{10}4f^{14}$, is only comprised of a single level, with a total angular momentum $J = 0$. The next higher level, in the [Kr] $4d^{10}4f^{13}5s^{1}$ configuration, has a total angular momentum of $J = 4$ and is thus metastable, featuring a $\Delta J = 4$ transition as direct connection to the ground state. Thus, the measured transition takes place inside the [Kr] $4d^{10}4f^{13}5s^{1}$ configuration, between the first and second excited level. More details on that transition are given in table 7.2. The `FAC` gives an energy $E \approx 42\,\mathrm{eV}$ above the ground state for the metastable state. Therefore, no interesting optical ground state transitions are anticipated for this ion.

Table 7.3: Observed wavelength λ of an optical, magnetic dipole (M1) transition in Pb XXIV. Continuation of table 7.2, reprinted from ref. [97].

$L_i \to L_f$	$J_i \to J_f$	$\lambda(\Delta\lambda_{stat})(\Delta\lambda_{sys})$(nm)	λ_A(nm)	I_F	g_{Ai}	g_{Af}
$1 \to 0$	$5/2 \to 7/2$	239.70162(150)(8)	242	1.55	0.86	1.14

Pr-like Pb XXIV The NIST data states [Kr]$4d^{10}4f^{13}$ as the electronic ground state configuration of Pb XXIV [83]. This was confirmed with both, `FAC` and AMBiT.

Accordingly, the following parameters were used in our calculations:

`FAC`

Core configuration

[Kr]

Configuration used for radial optimisation

$4d^{10}4f^{13}$

Shell configurations used for CI

$4d^{10}4f^{13}$

$4d^{10}4f^{12}5s^{1}$

$4d^{10}4f^{12}5p^{1}$

$4d^{9}4f^{14}$

$4d^{9}4f^{13}5s^{1}$

AMBiT ground state configuration

[Kr] $4d^{10}$: $4\bar{f}^{5.57}4f^{7.43}$

Leading configurations

$4f^{13}$

Number of considered electron excitations: 2

Number of considered hole excitation: 1

The transition identified in Pb XXIV takes place ins the ground states configuration [Kr] $4d^{10}4f^{13}$. This configuration comprises only two levels connected by a single transition, as stated in table 7.3. The lowest level of the next configuration, [Kr]$4d^{10}4f^{12}5s^1$, however is at an energy $E \approx 52\,\mathrm{eV}$ above the ground state according to `FAC` calculations. Therefore, no interesting optical ground state transitions are anticipated for this ion.

Table 7.4: Observed wavelength λ of optical, magnetic dipole (M1) transitions in Pb XXV. Continuation of table 7.2, reprinted from ref. [97].

$L_i \to L_f$	$J_i \to J_f$	$\lambda(\Delta\lambda_{stat})(\Delta\lambda_{sys})$(nm)	λ_A(nm)	I_F	g_{Ai}	g_{Af}
$3 \to 1$	$4 \to 4$	252.17575(25)(8)	258	0.91	1.01	1.14
$2 \to 0$	$5 \to 6$	252.77713(23)(8)	256	1.62	1.03	1.16

Ce-like Pb XXV The NIST data states [Kr]$4d^{10}4f^{12}$ as the electronic ground state configuration of Pb XXV [83]. This was confirmed with both, `FAC` and AMBiT.

Accordingly, the following parameters were used in our calculations:

`FAC` Core configuration

[Kr]

Configuration used for radial optimisation

$4d^{10}4f^{12}$

Shell configurations used for CI

$4d^{10}4f^{12}$
$4d^{10}4f^{11}5s^1$
$4d^{10}4f^{11}5p^1$
$4d^{9}4f^{13}$
$4d^{9}4f^{12}5s^1$

AMBiT

Ground state configuration

$[\mathrm{Kr}]\,4d^{10} : 4\bar{f}^{5.14}4f^{6.86}$

Leading configurations

$4f^{12}$

Number of considered electron excitations: 2

Number of considered hole excitation: 0

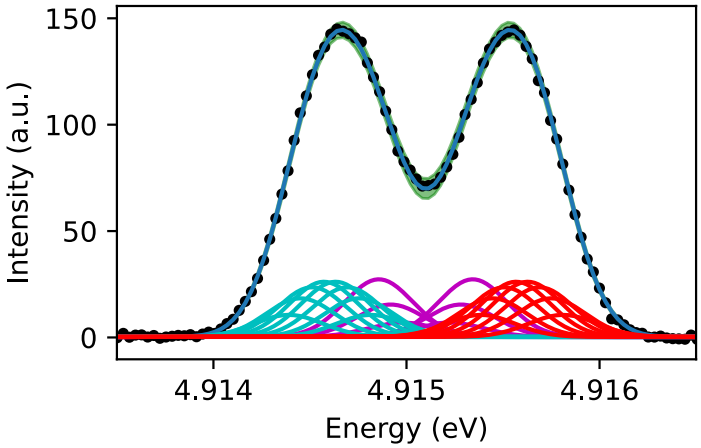

Figure 7.5: Zeeman fit of the $3 \rightarrow 1$ line in Pb XXV. For more details on the transition, refer to table 7.4. Data points are in black, fit in blue, and confidence bounds are in green. The individual Zeeman components are shown in teal, purple and red. The different colours correspond to different $\Delta m \in -1, 0, 1$.

The transitions identified in Pb XXV take place ins the ground states configuration $[\mathrm{Kr}]\ 4d^{10}4f^{12}$. They are stated in table 7.4, and one of them is a ground state transition. An exemplary Zeeman fit can be found in fig. 7.5. Unfortunately, no connection between the participating levels could be found, and no prediction over interesting optical ground state transitions can be made without further analysis.

Table 7.5: Observed wavelength λ of an optical, magnetic dipole (M1) transition in Pb XXVI. Continuation of table 7.2, reprinted from ref. [97].

$L_i \rightarrow L_f$	$J_i \rightarrow J_f$	$\lambda(\Delta\lambda_{stat})(\Delta\lambda_{sys})(\mathrm{nm})$	$\lambda_A(\mathrm{nm})$	I_F	g_{Ai}	g_{Af}
$1 \rightarrow 0$	$^{13}/_2 \rightarrow {}^{15}/_2$	264.88477(147)(8)	269	2.86	1.10	1.19

La-like Pb XXVI The NIST data states $[Kr]4d^{10}4f^{11}$ as the electronic ground state configuration of Pb XXVI [83]. This was confirmed with both, `FAC` and AMBiT.

Accordingly, the following parameters were used in our calculations:

`FAC` Core configuration

$[Kr]$

Configuration used for radial optimisation

$4d^{10}4f^{11}$

Shell configurations used for CI

$4d^{10}4f^{11}$
$4d^{10}4f^{10}5s^{1}$
$4d^{10}4f^{10}5p^{1}$
$4d^{9}4f^{12}$
$4d^{9}4f^{11}5s^{1}$

AMBiT Ground state configuration

$[Kr]\,4d^{10} : 4\bar{f}^{4.71}4f^{6.29}$

Leading configurations

$4f^{11}$

Number of considered electron excitations: 2

Number of considered hole excitation: 0

The transition identified in Pb XXVI take place ins the ground states configuration [Kr] $4d^{10}4f^{11}$. It is a ground state transition, as stated in table 7.5. Unfortunately, no other transition was found, and without further analysis, no prediction about interesting optical ground state transitions can be made.

Table 7.6: Observed wavelength λ of an optical, magnetic dipole (M1) transition in Pb XXVII. Continuation of table 7.2, reprinted from ref. [97].

$L_i \to L_f$	$J_i \to J_f$	$\lambda(\Delta\lambda_{stat})(\Delta\lambda_{sys})$(nm)	λ_A(nm)	I_F	g_{Ai}	g_{Af}
$1 \to 0$	$7 \to 8$	271.54179(13)(8)	277	5.39	1.16	1.22

Ba-like Pb XXVII The NIST data states [Kr]$4d^{10}4f^{10}$ as the electronic ground state configuration of Pb XXVII [83]. This was confirmed with both, `FAC` and AMBiT.

Accordingly, the following parameters were used in our calculations:

`FAC` Core configuration

[Kr]

Configuration used for radial optimisation

$4d^{10}4f^{10}$

Shell configurations used for CI

$4d^{10}4f^{10}$
$4d^{10}4f^{9}5s^{1}$
$4d^{10}4f^{9}5p^{1}$
$4d^{9}4f^{11}$
$4d^{9}4f^{10}5s^{1}$

AMBiT Ground state configuration

$[\mathrm{Kr}]\,4d^{10} : 4\bar{f}^{4.29}4f^{5.71}$

Leading configurations

$4f^{10}$

Number of considered electron excitations: 2

Number of considered hole excitation: 0

The transition identified in Pb XXVII take place ins the ground states configuration [Kr] $4d^{10}4f^{10}$. It is a ground state transition, as stated in table 7.6. Unfortunately, no other transition was found, and without further analysis, no prediction about interesting optical ground state transitions can be made.

Table 7.7: Observed wavelength λ of an optical, magnetic dipole (M1) transition in Pb XXVIII. Continuation of table 7.2, reprinted from ref. [97].

$L_i \to L_f$	$J_i \to J_f$	$\lambda(\Delta\lambda_{stat})(\Delta\lambda_{sys})$(nm)	λ_A(nm)	I_F	g_{Ai}	g_{Af}
$1 \to 0$	$^{13}/_2 \to {}^{15}/_2$	309.92900(56)(7)	318	5.38	1.25	1.28

Cs-like Pb XXVIII The NIST data states [Kr]$4d^{10}4f^9$ as the electronic ground state configuration of Pb XXVIII [83]. This was confirmed with both, `FAC` and AMBiT.

Accordingly, the following parameters were used in our calculations:

`FAC` Core configuration

[Kr]

Configuration used for radial optimisation

$4d^{10}4f^9$

Shell configurations used for CI

$4d^{10}4f^9$
$4d^{10}4f^8 5s^1$
$4d^{10}4f^8 5p^1$
$4d^9 4f^{10}$
$4d^9 4f^9 5s^1$

AMBiT Ground state configuration

[Kr] $4d^{10} : 4\bar{f}^{3.86}4f^{5.14}$

Leading configurations

$4f^9$

Number of considered electron excitations: 2

Number of considered hole excitation: 0

The transition identified in Pb XXVIII take place ins the ground states configuration [Kr] $4d^{10}4f^9$. It is a ground state transition, as stated in table 7.7. Unfortunately, no other transition was found, and without further analysis, no prediction about interesting optical ground state transitions can be made.

Table 7.8: Observed wavelength λ of optical, magnetic dipole (M1) transitions in Pb XXIX. Continuation of table 7.2, reprinted from ref. [97].

$L_i \to L_f$	$J_i \to J_f$	$\lambda(\Delta\lambda_{stat})(\Delta\lambda_{sys})$(nm)	λ_A(nm)	I_F	g_{Ai}	g_{Af}
$3 \to 0$	$5 \to 6$	413.96783(45)(17)	433	4.68	1.45	1.43
$4 \to 2$	$3 \to 4$	523.48424(47)(16)	578	1.26	1.44	1.41
$6 \to 5$	$9 \to 10$	733.89990(124)(13)	689	1.89	1.13	1.15

Xe-like Pb XXIX The NIST data states [Kr]$4d^{10}4f^8$ as the electronic ground state configuration of Pb XXIX [83]. This was confirmed with both, `FAC` and AMBiT.

Accordingly, the following parameters were used in our calculations:

`FAC` Core configuration

[Kr]

Configuration used for radial optimisation

$4d^{10}4f^8$

Shell configurations used for CI

$4d^{10}4f^8$
$4d^{10}4f^75s^1$
$4d^{10}4f^75p^1$
$4d^94f^9$
$4d^94f^85s^1$

AMBiT Ground state configuration

[Kr] $4d^{10} : 4\bar{f}^{3.43}4f^{4.57}$

Leading configurations

$4f^8$

Number of considered electron excitations: 2

Number of considered hole excitation: 0

The transitions identified in Pb XXIX take place in the ground states configuration [Kr] $4d^{10}4f^8$. They are given in table 7.8, and one of them is a ground state transition. The level structure of interest is depicted fig. 7.7. An exemplary Zeeman fit can be found in fig. 7.6. There is a clock transition candidate, $1 \rightarrow 0$ with a wavelength $\lambda \approx 595\,\mathrm{nm}$ according to AMBiT, and $\Delta J = 2$. At $E \approx 9.3\,\mathrm{eV}$ above the ground state and $J = 4$, a level is predicted that could connect the levels 1 and 2 with two vacuum ultraviolet (VUV) measurements, allowing the calculation of the clock candidates wavelength using Ritz-Rydberg combinations. The transitions characteristics are $\lambda \approx 170\,\mathrm{nm}$, $\Delta J = 0$ and $\lambda \approx 190\,\mathrm{nm}$, $\Delta J = 1$ respectively.

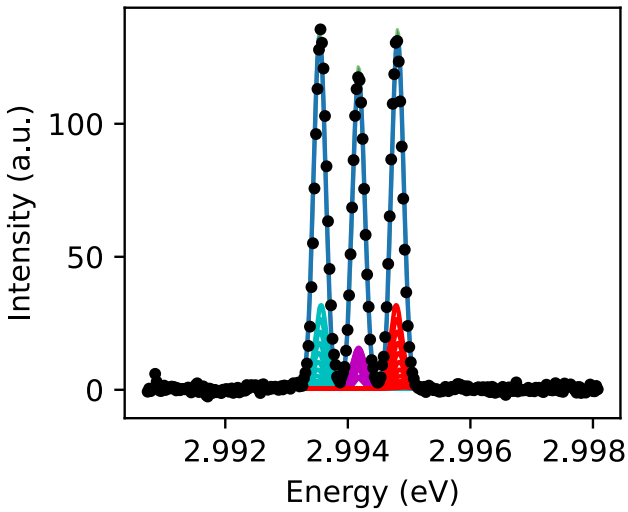

Figure 7.6: Zeeman fit of the $3 \to 0$ line in Pb XXIX. For more details on the transition, refer to table 7.8. Data points are in black, fit in blue, and confidence bounds are in green. The individual Zeeman components are shown in teal, purple and red. The different colours correspond to different $\Delta m \in -1, 0, 1$.

Table 7.9: Observed wavelength λ of optical, magnetic dipole (M1) transitions in Pb XXX. Continuation of table 7.2, reprinted from ref. [97].

$L_i \to L_f$	$J_i \to J_f$	$\lambda(\Delta\lambda_{stat})(\Delta\lambda_{sys})$(nm)	λ_A(nm)	I_F	g_{Ai}	g_{Af}
$2 \to 1$	$^7/_2 \to {}^7/_2$	370.79125(37)(7)	403	1.43	0.96	1.23
$3 \to 1$	$^9/_2 \to {}^7/_2$	345.98611(25)(7)	355	2.45	1.04	1.23

I-like Pb XXX The NIST data states $[Kr]4d^{10}4f^7$ as the electronic ground state configuration of Pb XXX [83]. This was confirmed with both, `FAC` and AMBiT.

Accordingly, the following parameters were used in our calculations:

`FAC`

Core configuration

$[Kr]$

Configuration used for radial optimisation

$4d^{10}4f^7$

Shell configurations used for CI

$4d^{10}4f^7$
$4d^{10}4f^6 5s^1$
$4d^9 4f^8$

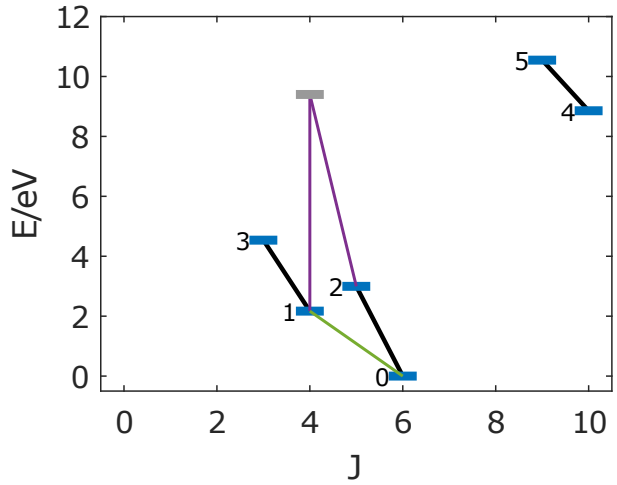

Figure 7.7: Partial Grotrian diagram showing transitions and energy levels of interest in Pb XXIX. Solid black lines mark measurements. The energy levels linked by observed transitions are shown in blue over their total angular momentum J. The lower energy levels for transitions not linked to the ground state are taken from AMBiT calculations. A potential bridge between the connected levels is predicted via the energy level shown in grey through two VUV transitions, marked by purple lines. The thus determinable clock transition candidate is shown in green. Reprinted from ref. [97].

AMBiT

Ground state configuration

$[\mathrm{Kr}]\,4d^{10} : 4\bar{f}^{3}4f^{4}$

Leading configurations

$4f^{7}$

Number of considered electron excitations: 2

Number of considered hole excitation: 0

The transitions identified in Pb XXX take place in the ground states configuration $[\mathrm{Kr}]\ 4d^{10}4f^{7}$. According to `FAC`, the first excited level is too high for this ion to feature any optical ground state transitions. The found transitions between excited levels are displayed in fig. 7.9 and table 7.9. An exemplary Zeeman fit can be found in fig. 7.8.

Te-like Pb XXXI The NIST data states $[\mathrm{Kr}]4d^{10}4f^{6}$ as the electronic ground state configuration of Pb XXXI [83]. This was confirmed with both, `FAC` and AMBiT.

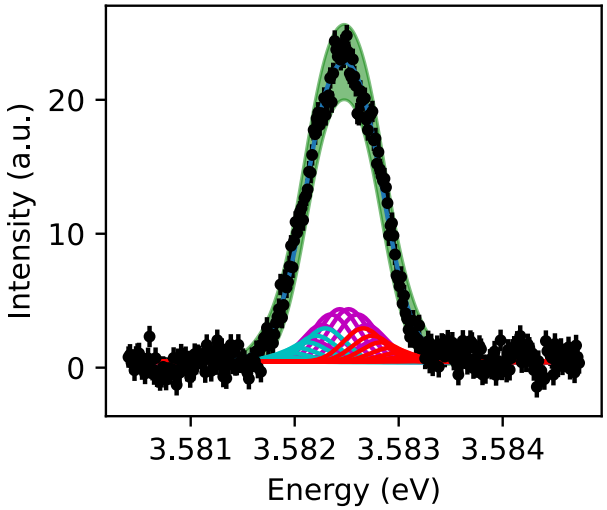

Figure 7.8: Zeeman fit of the $3 \rightarrow 1$ line in Pb XXX. For more details on the transition, refer to table 7.9. Data points are in black, fit in blue, and confidence bounds are in green. The individual Zeeman components are shown in teal, purple and red. The different colours correspond to different $\Delta m \in -1, 0, 1$.

Table 7.10: Observed wavelength λ of optical, magnetic dipole (M1) transitions in Pb XXXI. Continuation of table 7.2, reprinted from ref. [97].

$L_i \rightarrow L_f$	$J_i \rightarrow J_f$	$\lambda(\Delta\lambda_{stat})(\Delta\lambda_{sys})$(nm)	λ_A(nm)	I_F	g_{Ai}	g_{Af}
$1 \rightarrow 0$	$1 \rightarrow 0$	392.65739(26)(6)	427	18.73	1.50	0
$2 \rightarrow 1$	$2 \rightarrow 1$	524.68818(101)(16)	543	10.42	1.47	1.50
$3 \rightarrow 2$	$3 \rightarrow 2$	737.13765(31)(13)	736	3.74	1.45	1.47

Accordingly, the following parameters were used in our calculations:

`FAC` Core configuration

[Kr]

Configuration used for radial optimisation

$4d^{10}4f^{6}$

Shell configurations used for CI

$4d^{10}4f^{6}$

$4d^{10}4f^{5}5s^{1}$

$4d^{9}4f^{7}$

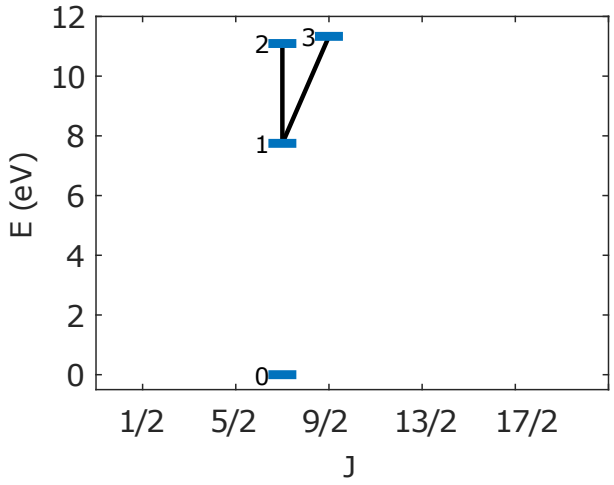

Figure 7.9: Partial Grotrian diagram showing transitions and energy levels of interest in Pb XXX. Solid black lines mark measurements. The energy levels linked by observed transitions are shown in blue over their total angular momentum J. The lower energy level for the transitions not linked to the ground state is taken from AMBiT calculations. Reprinted from ref. [97].

AMBiT

Ground state configuration

$[\mathrm{Kr}]\,4d^{10} : 4\bar{f}^{2.57}4f^{3.43}$

Leading configurations

$4f^{6}$

Number of considered electron excitations: 2

Number of considered hole excitation: 0

The transitions identified in Pb XXXI take place in the ground states configuration [Kr] $4d^{10}4f^{6}$. A "ladder" of three transitions was established, connecting the four lowest levels, as seen in fig. 7.11 and table 7.10. The black lines indicate measured transitions. An exemplary Zeeman fit can be found in fig. 7.10.

Sb-like Pb XXXII The NIST data states $[\mathrm{Kr}]4d^{10}4f^{5}$ as the electronic ground state configuration of Pb XXXII [83]. This was confirmed with both, `FAC` and AMBiT.

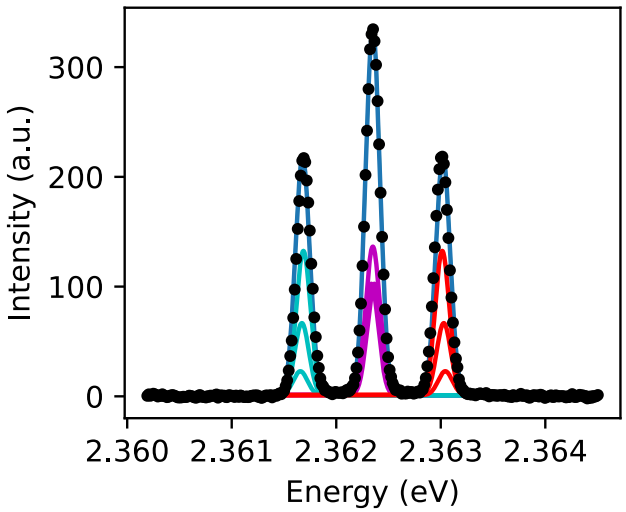

Figure 7.10: Zeeman fit of the $2 \to 1$ line in Pb XXXI. For more details on the transition, refer to table 7.10. Data points are in black, fit in blue, and confidence bounds are in green. The individual Zeeman components are shown in teal, purple and red. The different colours correspond to different $\Delta m \in -1, 0, 1$.

Accordingly, the following parameters were used in our calculations:

`FAC`

Core configuration

[Kr]

Configuration used for radial optimisation

$4d^{10}4f^{5}$

Shell configurations used for CI

$4d^{10}4f^{5}$

$4d^{10}4f^{4}5s^{1}$

$4d^{9}4f^{6}$

Table 7.11: Observed wavelength λ of optical, magnetic dipole (M1) transitions in Pb XXXII. Continuation of table 7.2, reprinted from ref. [97].

$L_i \to L_f$	$J_i \to J_f$	$\lambda(\Delta\lambda_{stat})(\Delta\lambda_{sys})$(nm)	λ_A(nm)	I_F	g_{Ai}	g_{Af}
$1 \to 0$	$^7/_2 \to {}^5/_2$	343.16795(78)(7)	364	7.10	0.89	0.53
$3 \to 1$	$^9/_2 \to {}^7/_2$	490.49287(18)(16)	496	2.22	1.06	0.89
$5 \to 1$	$^7/_2 \to {}^7/_2$	283.75284(55)(8)	272	0.87	1.27	0.89
$5 \to 2$	$^7/_2 \to {}^5/_2$	434.81120(60)(17)	443	1.64	1.27	1.02
$4 \to 3$	$^{11}/_2 \to {}^9/_2$	771.89599(157)(13)	741	0.64	1.13	1.06
$6 \to 5$	$^9/_2 \to {}^7/_2$	626.21185(87)(15)	597	0.59	1.30	1.27

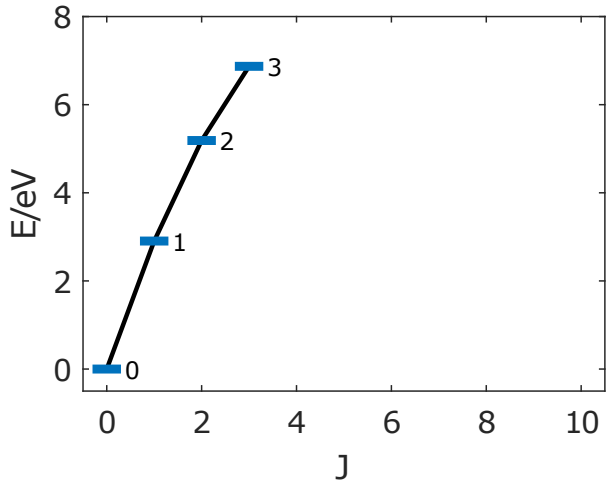

Figure 7.11: Partial Grotrian diagram showing transitions and energy levels of interest in Pb XXXI. Solid black lines mark measurements. The energy levels linked by observed transitions are shown in blue over their total angular momentum J. Reprinted from ref. [97].

AMBiT

Ground state configuration

$[\mathrm{Kr}]\,4d^{10} : 4\bar{f}^{2.14}4f^{2.86}$

Leading configurations

$4f^5$

Number of considered electron excitations: 2

Number of considered hole excitation: 0

The transitions identified in Pb XXXII take place in the ground states configuration [Kr] $4d^{10}4f^5$. Two connected "ladders" of six transitions were established, connecting seven different levels in the ion, compare table 7.11 and fig. 7.14. One ground state transition is found. Unfortunately, no optical clock candidate could be found in this ion. Exemplary Zeeman fits can be found in figs. 7.12 and 7.13.

Sn-like Pb XXXIII The NIST data states $[\mathrm{Kr}]4d^{10}4f^5$ as the electronic ground state configuration of Pb XXXIII [83]. This was confirmed with both, `FAC` and AMBiT.

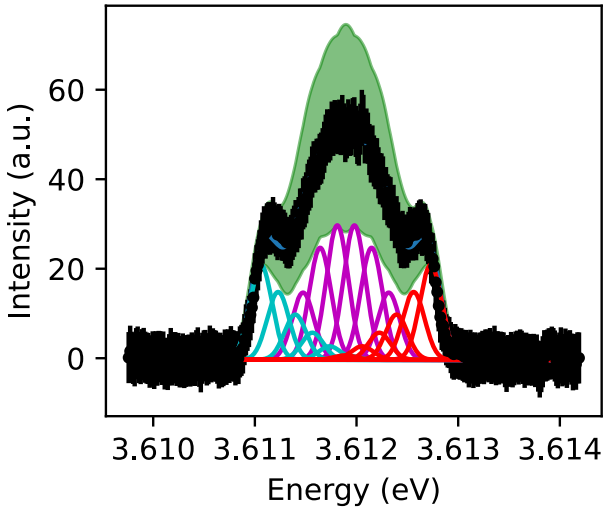

Figure 7.12: Zeeman fit of the $1 \to 0$ line in Pb XXXII. For more details on the transition, refer to table 7.11. Data points are in black, fit in blue, and confidence bounds are in green. The individual Zeeman components are shown in teal, purple and red. The different colours correspond to different $\Delta m \in -1, 0, 1$.

Accordingly, the following parameters were used in our calculations:

`FAC`

Core configuration

[Kr]

Configuration used for radial optimisation

$4d^{10}4f^{4}$

Shell configurations used for CI

$4d^{10}4f^{4}$

$4d^{10}4f^{3}5s^{1}$

$4d^{9}4f^{5}$

Table 7.12: Observed wavelength λ of optical, magnetic dipole (M1) transitions in Pb XXXIII. Continuation of table 7.2, reprinted from ref. [97].

$L_i \to L_f$	$J_i \to J_f$	$\lambda(\Delta\lambda_{stat})(\Delta\lambda_{sys})$(nm)	λ_A(nm)	I_F	g_{Ai}	g_{Af}
$1 \to 0$	$5 \to 4$	284.88000(61)(8)	296	2.55	0.92	0.68
$3 \to 1$	$6 \to 5$	442.31591(51)(17)	437	0.78	1.03	0.92
$4 \to 2$	$1 \to 2$	381.97750(24)(6)	425	2.21	0.17	0.91
$6 \to 2$	$3 \to 2$	277.931099(36)(8)	296	1.14	1.07	0.91
$7 \to 2$	$2 \to 2$	258.09230(49)(8)	264	2.17	0.66	0.91
$8 \to 5$	$5 \to 4$	301.21601(51)(8)	292	0.33	1.16	1.00

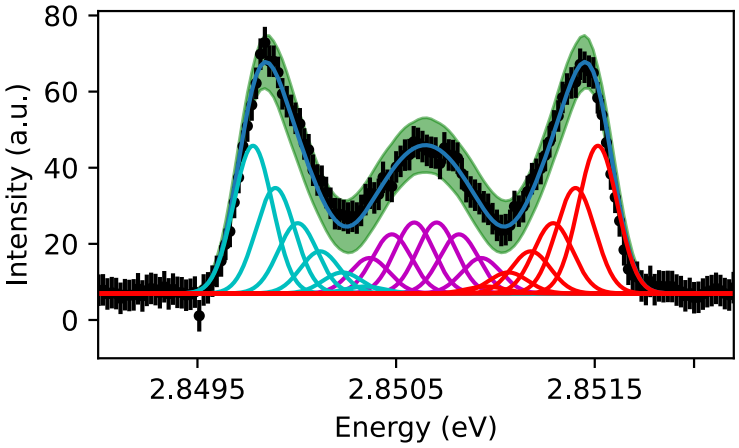

Figure 7.13: Zeeman fit of the $5 \rightarrow 2$ line in Pb XXXII. For more details on the transition, refer to table 7.11. Data points are in black, fit in blue, and confidence bounds are in green. The individual Zeeman components are shown in teal, purple and red. The different colours correspond to different $\Delta m \in -1, 0, 1$.

AMBiT

Ground state configuration

$[\mathrm{Kr}]\, 4d^{10} : 4\bar{f}^{1.71} 4f^{2.29}$

Leading configurations

$4f^4$

Number of considered electron excitations: 2

Number of considered hole excitation: 0

The transitions identified in Pb XXXIII take place in the ground states configuration [Kr] $4d^{10}4f^4$. Multiple connected transitions in three separate clusters have been found, as seen in fig. 7.17 and table 7.12. To establish the optical clock transition between the ground state 0 and the metastable state 2, shown in green, the respective clusters need to be connected. AMBiTpredicts its wavelength $\lambda \approx 225\,\mathrm{nm}$, the achange in total angular momentum change is $2 \rightarrow 4$. A direct link is predicted with the VUV transition between the levels $6 \rightarrow 0$. It features a strong intensity $I = 1.26$ predicted by CRM, at a wavelength $\lambda \approx 130\,\mathrm{nm}$ according to AMBiT, with a total angular momentum change $3 \rightarrow 4$. Exemplary Zeeman fits in figs. 7.15 and 7.16.

In-like Pb XXXIV The NIST data states $[\mathrm{Kr}]4d^{10}4f^3$ as the electronic ground state configuration of Pb XXXIV [83]. This was confirmed with both, `FAC` and AMBiT.

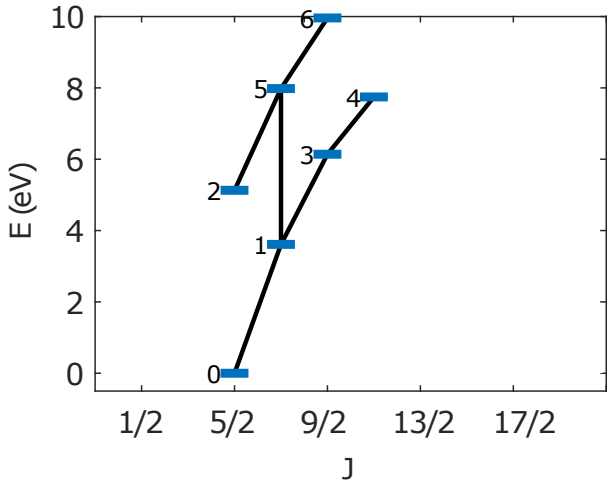

Figure 7.14: Partial Grotrian diagram showing transitions and energy levels of interest in Pb XXXII. Solid black lines mark measurements. The energy levels linked by observed transitions are shown in blue over their total angular momentum J. Reprinted from ref. [97].

Table 7.13: Observed wavelength λ of an optical, magnetic dipole (M1) transition in Pb XXXIV. Continuation of table 7.2, reprinted from ref. [97].

$L_i \to L_f$	$J_i \to J_f$	$\lambda(\Delta\lambda_{stat})(\Delta\lambda_{sys})$(nm)	λ_A(nm)	I_F	g_{Ai}	g_{Af}
$3 \to 2$	$^5/_2 \to {}^3/_2$	409.47995(59)(17)	396	5.94	0.82	0.71

Accordingly, the following parameters were used in our calculations:

`FAC` Core configuration

[Kr]

Configuration used for radial optimisation

$4d^{10}4f^3$

Shell configurations used for CI

$4d^{10}4f^3$

$4d^{10}4f^25s^1$

$4d^94f^4$

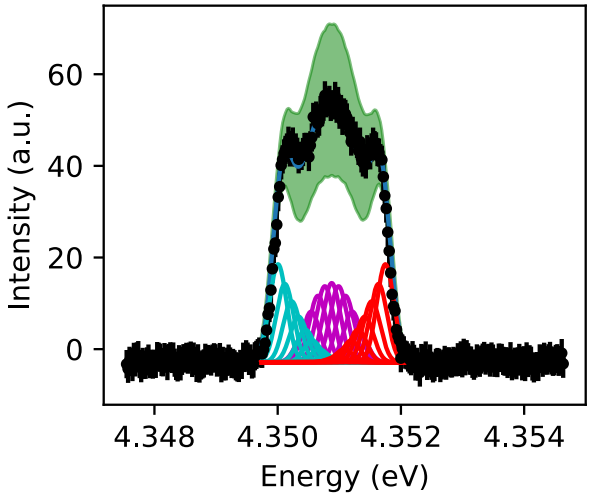

Figure 7.15: Zeeman fit of the $1 \rightarrow 0$ line in Pb XXXIII. For more details on the transition, refer to table 7.12. Data points are in black, fit in blue, and confidence bounds are in green. The individual Zeeman components are shown in teal, purple and red. The different colours correspond to different $\Delta m \in -1, 0, 1$.

AMBiT

Ground state configuration

$[\mathrm{Kr}]\, 4d^{10} : 4\bar{f}^{1.29} 4f^{1.71}$

Leading configurations

$4f^3$

Number of considered electron excitations: 2

Number of considered hole excitation: 0

The transitions identified in Pb XXXIV take place in the ground states configuration [Kr] $4d^{10}4f^3$. An optical transition was identified, compare fig. 7.19 and table 7.13. Its Zeeman fit can be found in fig. 7.18. According to our calculations, the first excited state is too high for that ion to feature any optical ground state transitions; thus, transitions of interest are not expected here.

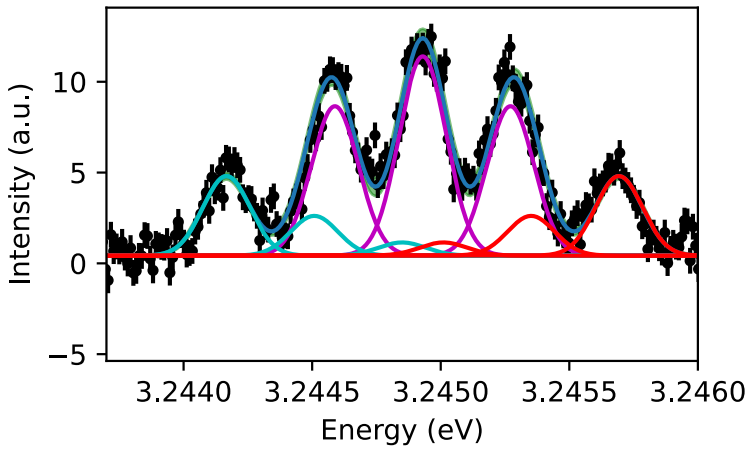

Figure 7.16: Zeeman fit of the $4 \rightarrow 2$ line in Pb XXXIII. For more details on the transition, refer to table 7.12. Data points are in black, fit in blue, and confidence bounds are in green. The individual Zeeman components are shown in teal, purple and red. The different colours correspond to different $\Delta m \in -1, 0, 1$.

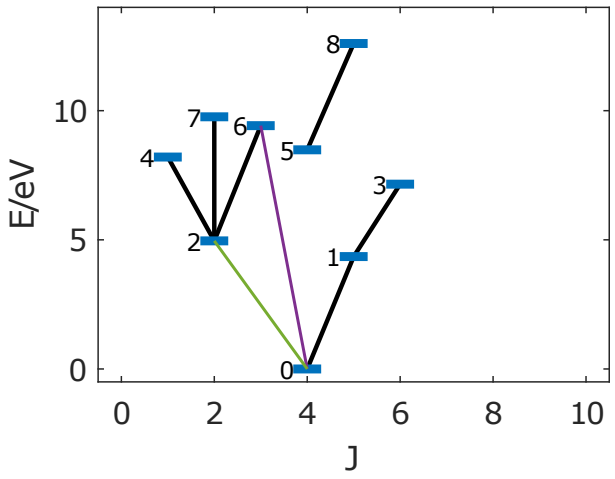

Figure 7.17: Partial Grotrian diagram showing transitions and energy levels of interest in Pb XXXIII. Solid black lines mark measurements. The energy levels linked by observed transitions are shown in blue over their total angular momentum J. The lower energy levels for transitions not linked to the ground state are taken from AMBiT calculations. A potential bridge between the connected levels is predicted via a VUV transition, marked by a purple line. The thus determinable clock transition candidate is shown in green. Reprinted from ref. [97].

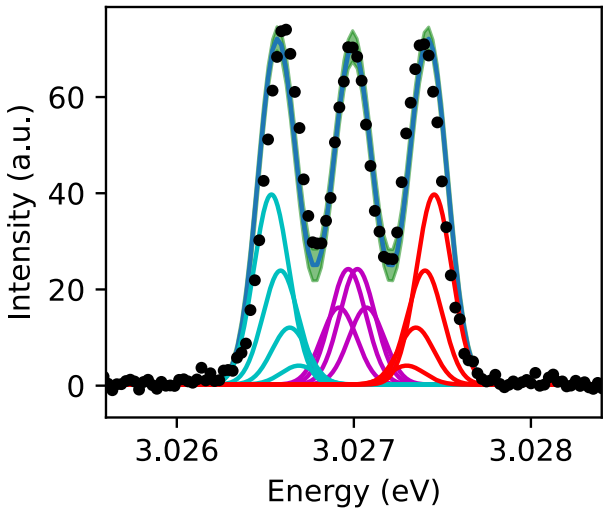

Figure 7.18: Zeeman fit of the $3 \rightarrow 2$ line in Pb XXXIV. For more details on the transition, refer to table 7.13. Data points are in black, fit in blue, and confidence bounds are in green. The individual Zeeman components are shown in teal, purple and red. The different colours correspond to different $\Delta m \in -1, 0, 1$.

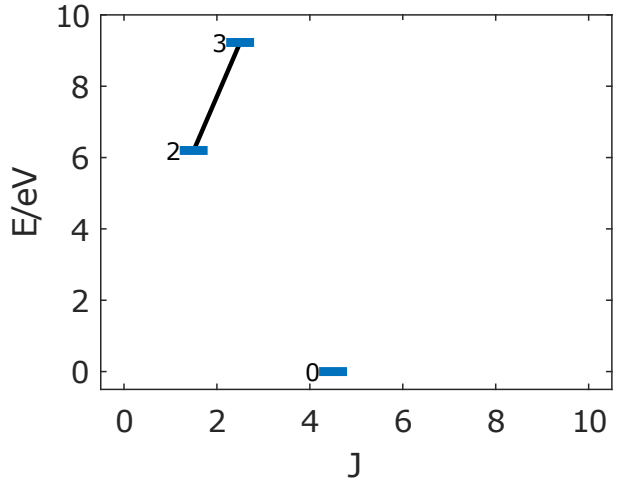

Figure 7.19: Partial Grotrian diagram showing transitions and energy levels of interest in Pb XXXIV. Solid black lines mark measurements. The energy levels linked by observed transitions are shown in blue over their total angular momentum J. The lower energy level for the transition not linked to the ground state is taken from AMBiT calculations. Reprinted from ref. [97].

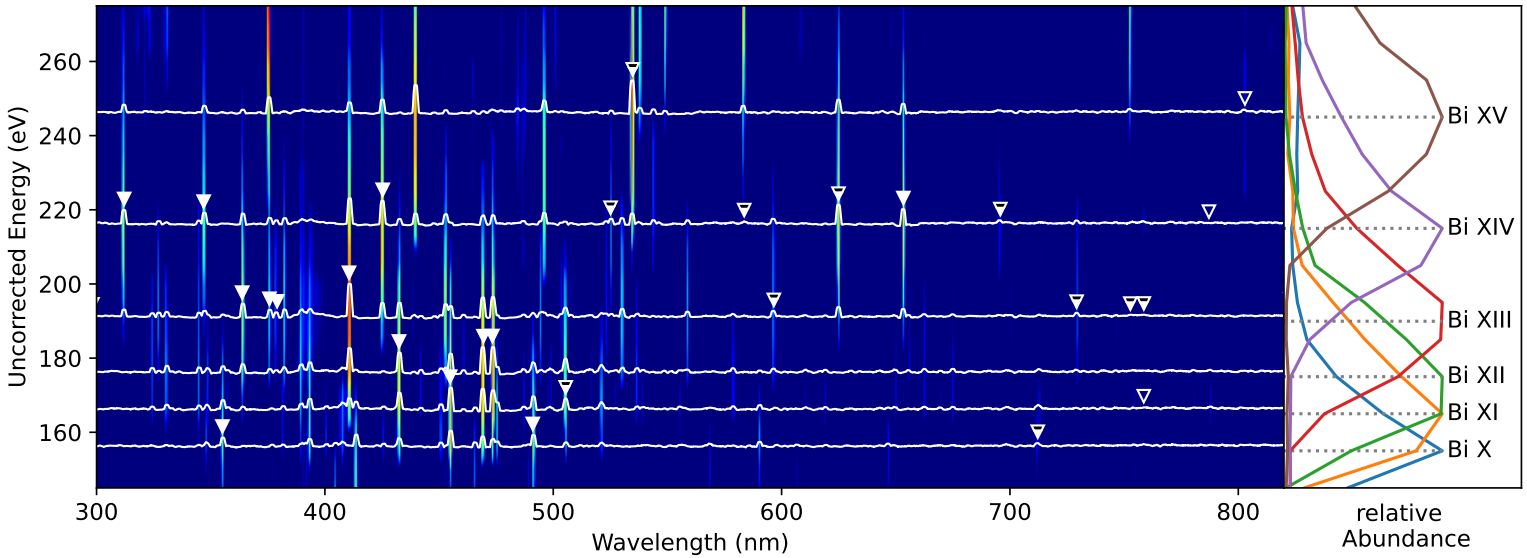

Figure 7.20: Overview of the measured bismuth lines in between 300 nm and 810 nm. The two-dimensional spectrum is shown in the background. The charge state distribution shown to the right was extracted from the signal along a prominent line and normalised. The acceleration voltage U_{acc} at their maxima has been calculated. The white lines show the spectrum taken at these U_{acc} values, raised by that U_{acc}, flattened by a moving average filter. The white triangles indicate the identified transitions in 1^{st} (filled), 2^{nd} (half-filled) and 3^{rd} (unfilled) order. Adapted from ref. [97].

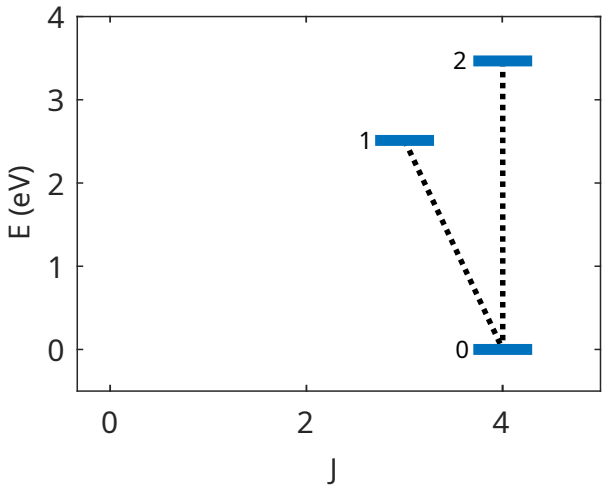

Figure 7.21: Partial Grotrian diagram showing transitions and energy levels of interest in Bi X. Black lines mark measurements, preliminary identifications are dotted. The energy levels linked by observed transitions are shown in blue over their total angular momentum J. Reprinted from ref. [97].

7.2 Bismuth

The overview spectrum for bismuth can be seen in fig. 7.20. Due to the lower number of electrons in the d-subshell, identifying charge states and subsequent extraction of lines was easier than for lead. Therefore, the use of NNMF was deemed unnecessary. Again, $E_\mathrm{i} < U_\mathrm{acc}$ has been found, confirming our identification.

In the six charge states from Bi X to Bi XV, 19 magnetic dipole (M1) transitions have been found. Thirteen of those transitions have been unambiguously identified, the remaining six preliminary. The preliminary identifications here are mainly due to low measurement precision, as not all lines given have been measured with the fine grating. Instead, a calibration line reference for the coarse grating measurements has been carried out, yielding intermediate accuracies of $\sim 10\,\mathrm{pm}$. The effort of sub-pm measurements, on the other hand, has been mainly concentrated on Bi XIV, as the calculation promised an interesting clock candidate ground state transition with a total angular momentum change of $\Delta J = 0$. The charge states, with their measured lines and calculation parameters, are now discussed in more detail. An overview of those results can also be found in table A.4.

Table 7.14: Observed wavelength λ of optical, magnetic dipole (M1) transitions in Bi X. Wavelength uncertainties are given as statistical uncertainty ($\Delta\lambda_{\mathrm{stat}}$) and a systematic uncertainty ($\Delta\lambda_{\mathrm{sys}}$). The initial ($\mathrm{L_i}$) and final ($\mathrm{L_f}$) levels are given, as well as the initial (J_i) and final (J_f) total angular momenta. Calculations with AMBiT include the calculated wavelength λ_A, the g factor of the initial (g_Ai) and final (g_Af) level, as well as transition rates $A_{ki}(\mathrm{s}^{-1})$. Reprinted from ref. [97].

$\mathrm{L_i} \rightarrow \mathrm{L_f}$	$J_\mathrm{i} \rightarrow J_\mathrm{f}$	$\lambda(\Delta\lambda_{\mathrm{stat}})(\Delta\lambda_{\mathrm{sys}})$(nm)	λ_A(nm)	$A_{ki}(\frac{1}{\mathrm{s}})$	g_Ai	g_Af
$2 \rightarrow 0$ p	$4 \rightarrow 4$	356.18(8)(12)	349.5	364.7	1.104	1.377
$1 \rightarrow 0$ p	$3 \rightarrow 4$	491.93805(92)(4)	503.7	211.0	1.439	1.377

p: preliminary identification

W-like Bi X The NIST data states $[\mathrm{Xe}]4\mathrm{f}^{14}5\mathrm{d}^6$ as the electronic ground state configuration of Bi X [83]. This was confirmed with both, `FAC` and AMBiT.

Accordingly, the following parameters were used in our calculations:

`FAC`

Core configuration

$[\mathrm{Xe}]4\mathrm{f}^{14}$

Configuration used for radial optimisation

$5\mathrm{d}^6$

Shell configurations used for CI

$5\mathrm{d}^6$
$5\mathrm{d}^5\ 5\mathrm{f}^1$
$5\mathrm{d}^5\ 5\mathrm{g}^1$
$5\mathrm{d}^5\ 6\mathrm{s}^1$
$5\mathrm{d}^5\ 6\mathrm{p}^1$
$5\mathrm{d}^5\ 7\mathrm{s}^1$
$5\mathrm{d}^5\ 7\mathrm{p}^1$

AMBiT

Ground state configuration

$[\mathrm{Xe}]\ 4\mathrm{f}^{14} : 5\bar{\mathrm{d}}^{2.3}5\mathrm{d}^{3.7}$

Leading configurations

$5\mathrm{d}^6$

Number of considered electron excitations: 2

Number of considered hole excitation: 0

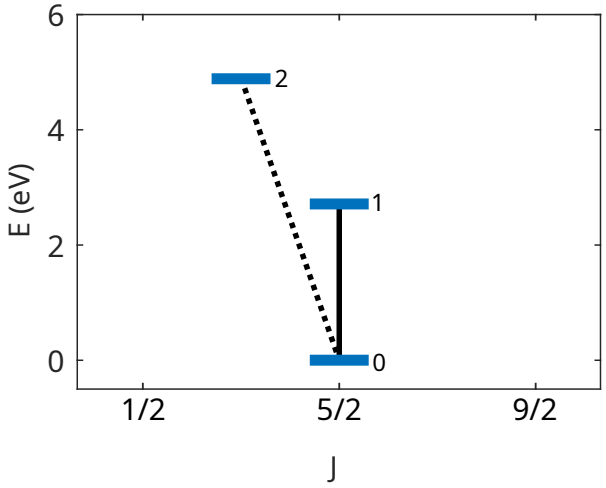

Figure 7.22: Partial Grotrian diagram showing transitions and energy levels of interest in Bi XI. Black lines mark measurements, preliminary identifications are dotted. The energy levels linked by observed transitions are shown in blue over their total angular momentum J. Reprinted from ref. [97].

The two preliminarily identified transitions in Bi X take place inside the $[Xe]4f^{14}5d^6$ configuration. They are both ground state transitions, as seen in fig. 7.21. The transition details are listed in table 7.14. No interesting optical ground state transitions are anticipated for this ion, so more precision measurements are unnecessary.

Table 7.15: Observed wavelength λ of optical, magnetic dipole (M1) transitions in Bi XI. Continuation of table 7.14, reprinted from ref. [97].

$L_i \rightarrow L_f$	$J_i \rightarrow J_f$	$\lambda(\Delta\lambda_{stat})(\Delta\lambda_{sys})$(nm)	λ_A(nm)	$A_{ki}(\frac{1}{s})$	g_{Ai}	g_{Af}
$1 \rightarrow 0$	$5/2 \rightarrow 5/2$	455.8462(13)(3)	435.7	307.8	1.145	1.733
$2 \rightarrow 0$ p	$3/2 \rightarrow 5/2$	253.071(69)(26)	258.1	625.8	1.280	1.733

p: preliminary identification

Ta-like Bi XI The NIST data states $[Xe]4f^{14}5d^5$ as the electronic ground state configuration of Bi XI [83]. This was confirmed with both, `FAC` and AMBiT.

Accordingly, the following parameters were used in our calculations:

FAC

Core configuration

$[Xe]4f^{14}$

Configuration used for radial optimisation

$5d^5$

Shell configurations used for CI

$5d^5$
$5d^4\ 5f^1$
$5d^4\ 5g^1$
$5d^4\ 6s^1$
$5d^4\ 6p^1$
$5d^4\ 7s^1$
$5d^4\ 7p^1$

AMBiT

Ground state configuration

$[Xe]\ 4f^{14} : 5\bar{d}^2 5d^3$

Leading configurations

$5d^5$

Number of considered electron excitations: 2

Number of considered hole excitation: 0

The two found transitions in Bi XI take place inside the $[Xe]4f^{14}5d^5$ configuration. One is preliminarily identified, and one definitely. They are both ground state transitions, as seen in fig. 7.22. The transition details are listed in table 7.15. No interesting optical ground state transitions are anticipated for this ion, rendering more precision measurements unnecessary.

Table 7.16: Observed wavelength λ of optical, magnetic dipole (M1) transitions in Bi XII. Continuation of table 7.14, reprinted from ref. [97].

$L_i \to L_f$	$J_i \to J_f$	$\lambda(\Delta\lambda_{stat})(\Delta\lambda_{sys})$(nm)	λ_A(nm)	$A_{ki}(\frac{1}{s})$	g_{Ai}	g_{Af}
$5 \to 3$	$3 \to 3$	433.40007(43)(24)	425.0	237.9	1.010	1.320
$1 \to 0$	$1 \to 0$	469.91626(17)(3)	489.6	271.8	1.498	0
$4 \to 2$	$4 \to 4$	474.4117(24)(5)	490.2	265.2	1.143	1.162

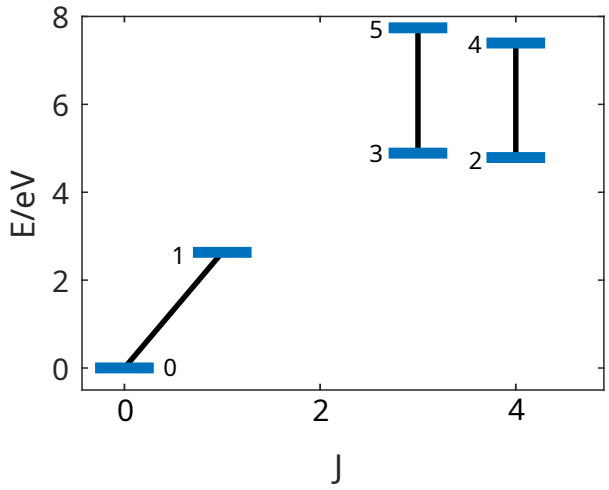

Figure 7.23: Partial Grotrian diagram showing transitions and energy levels of interest in Bi XII. Black lines mark measurements. The energy levels linked by observed transitions are shown in blue over their total angular momentum J. The lower energy level for the transitions not linked to the ground state is taken from AMBiT calculations. Reprinted from ref. [97].

Hf-like Bi XII The NIST data states $[Xe]4f^{14}5d^4$ as the electronic ground state configuration of Bi XII [83]. This was confirmed with both, `FAC` and AMBiT.

Accordingly, the following parameters were used in our calculations:

`FAC`

Core configuration

$[Xe]4f^{14}$

Configuration used for radial optimisation

$5d^4$

Shell configurations used for CI

$5d^4$
$5d^3\ 5f^1$
$5d^3\ 5g^1$
$5d^3\ 6s^1$
$5d^3\ 6p^1$
$5d^3\ 7s^1$
$5d^3\ 7p^1$

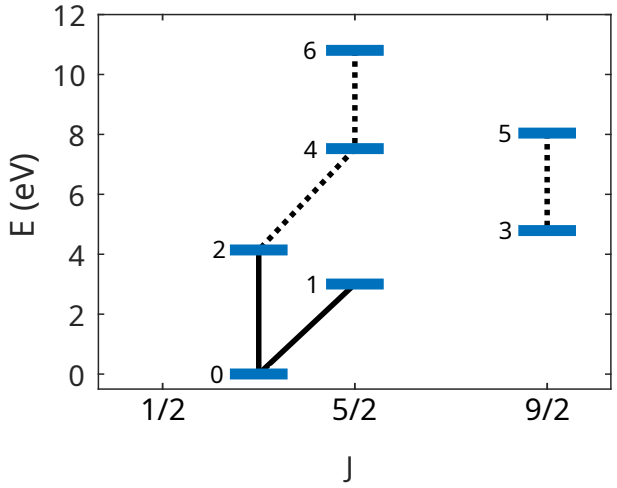

Figure 7.24: Partial Grotrian diagram showing transitions and energy levels of interest in Bi XIII. Black lines mark measurements, preliminary identifications are dotted. The energy levels linked by observed transitions are shown in blue over their total angular momentum J. The lower energy level for the transitions not linked to the ground state is taken from AMBiT calculations. Reprinted from ref. [97].

AMBiT Ground state configuration

$[\mathrm{Xe}]\,4f^{14} : 5\bar{d}^{1.6}5d^{2.4}$

Leading configurations

$5d^4$

Number of considered electron excitations: 2

Number of considered hole excitation: 0

The three identified transitions in Bi XII take place inside the $[\mathrm{Xe}]4f^{14}5d^4$ configuration. One is a ground state transition, and they are not connected, as seen in fig. 7.23. The transition details are listed in table 7.16. Further measurements might yield an interesting optical clock candidate, $3 \rightarrow 0$. This, however, requires extensive work in VUV spectroscopy, which is out of the scope of this work.

Lu-like Bi XIII The NIST data states $[\mathrm{Xe}]4f^{14}5d^3$ as the electronic ground state configuration of Bi XIII [83]. This was confirmed with both, `FAC` and AMBiT.

Table 7.17: Observed wavelength λ of optical, magnetic dipole (M1) transitions in Bi XIII. Continuation of table 7.14, reprinted from ref. [97].

$L_i \rightarrow L_f$	$J_i \rightarrow J_f$	$\lambda(\Delta\lambda_{stat})(\Delta\lambda_{sys})$(nm)	λ_A(nm)	$A_{ki}(\frac{1}{s})$	g_{Ai}	g_{Af}
$2 \rightarrow 0$	$^3/_2 \rightarrow {}^3/_2$	298.5070(14)(1)	292.9	391.5	1.298	0.595
$4 \rightarrow 2$ p	$^5/_2 \rightarrow {}^3/_2$	365.893(38)(41)	376.4	143.9	1.471	1.298
$6 \rightarrow 4$ p	$^5/_2 \rightarrow {}^5/_2$	376.54(5)(11)	371.1	194.1	1.060	1.471
$5 \rightarrow 3$ p	$^9/_2 \rightarrow {}^9/_2$	379.40(6)(12)	368.9	337.9	1.133	1.100
$1 \rightarrow 0$	$^5/_2 \rightarrow {}^3/_2$	411.56092(35)(6)	420.9	414.9	1.046	0.595

p: preliminary identification

Accordingly, the following parameters were used in our calculations:

`FAC`

Core configuration

$[Xe]4f^{14}$

Configuration used for radial optimisation

$5d^3$

Shell configurations used for CI

$5d^3$
$5d^2\ 5f^1$
$5d^2\ 5g^1$
$5d^2\ 6s^1$
$5d^2\ 6p^1$
$5d^2\ 7s^1$
$5d^2\ 7p^1$

AMBiT

Ground state configuration

$[Xe]\ 4f^{14} : 5\bar{d}^{1.2}5d^{1.8}$

Leading configurations

$5d^3$

Number of considered electron excitations: 2

Number of considered hole excitation: 0

The five transitions found in Bi XIII take place inside the $[Xe]4f^{14}5d^3$ configuration. The identifications are only preliminary, except for the two ground state transitions. Four of the involved energy levels can be connected to the ground state, as seen in fig. 7.24. The transition details are listed in table 7.17. Finding a link between the $5 \rightarrow 3$ transition using VUV spectroscopy and confirming the involved preliminarily identifications may give the $3 \rightarrow 0$ ground state transition as a clock candidate, featuring $\Delta J = 3$.

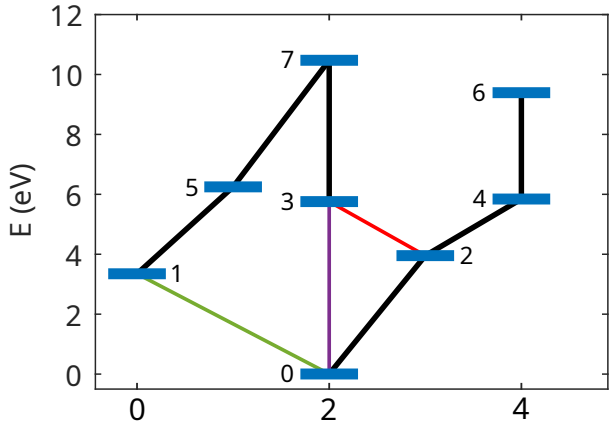

Figure 7.25: Partial Grotrian diagram showing transitions and energy levels of interest in Bi XIV. Black lines mark measurements, preliminary identifications are dotted. The energy levels linked by observed transitions are shown in blue over their total angular momentum J. The lower energy level for the transitions not linked to the ground state is taken from AMBiT calculations. Possible connections out of range of our setup are shown in red ($\lambda > 800\,\mathrm{nm}$) and purple ($\lambda < 200\,\mathrm{nm}$). A possible candidate for an optical clock transition is shown in green. Reprinted from ref. [97].

Yb-like Bi XIV The NIST data states $[\mathrm{Xe}]4f^{14}5d^2$ as the electronic ground state configuration of Bi XIV [83]. This was confirmed with both, `FAC` and AMBiT.

Table 7.18: Observed wavelength λ of optical, magnetic dipole (M1) transitions in Bi XIV. Continuation of table 7.14, reprinted from ref. [97].

$L_i \rightarrow L_f$	$J_i \rightarrow J_f$	$\lambda(\Delta\lambda_{stat})(\Delta\lambda_{sys})$(nm)	λ_A(nm)	$A_{ki}(\frac{1}{s})$	g_{Ai}	g_{Af}
$7 \rightarrow 3$	$2 \rightarrow 2$	263.0410(61)(8)	261.0	669.7	1.231	1.197
$7 \rightarrow 5$	$2 \rightarrow 1$	292.43047(83)(37)	288.6	274.4	1.231	1.500
$2 \rightarrow 0$	$3 \rightarrow 2$	312.8075(21)(2)	313.6	674.5	1.083	0.738
$6 \rightarrow 4$	$4 \rightarrow 4$	348.058773(101)(50)	345.3	202.2	1.112	1.138
$5 \rightarrow 1$	$1 \rightarrow 0$	425.91653(50)(1)	436.7	178.9	1.500	0
$4 \rightarrow 2$	$4 \rightarrow 3$	653.87821(34)(3)	627.8	44.9	1.214	1.273

Accordingly, the following parameters were used in our calculations:

`FAC`

Core configuration

$[Xe]4f^{14}$

Configuration used for radial optimisation

$5d^2$

Shell configurations used for CI

$5d^2$
$5d^1\ 5f^1$
$5d^1\ 5g^1$
$5d^1\ 6s^1$
$5d^1\ 6p^1$
$5d^1\ 7s^1$
$5d^1\ 7p^1$

AMBiT

Ground state configuration

$[Xe]\ 4f^{14} : 5\bar{d}^{0.8}5d^{1.2}$

Leading configurations

$5d^2$

Number of considered electron excitations: 2

Number of considered hole excitation: 0

The five transitions identified in Bi XIV take place inside the $[Xe]4f^{14}5d^2$ configuration. three of the involved energy levels can be connected to the ground state, and the other four form a second separate cluster, as seen in fig. 7.25. The transition details are listed in table 7.18. Connecting the two

branches may yield an optical clock candidate by the higher order optical ground state transition $1 \rightarrow 0$, featuring $\Delta J = 2$. Two possible links are just out of range for our setup, $3 \rightarrow 2$ most likely has a wavelength $\lambda > 800\,\mathrm{nm}$, $3 \rightarrow 0$, on the other hand, most likely has a wavelength $\lambda < 200\,\mathrm{nm}$. Modifying the setup may make those transitions accessible. Connecting both branches via VUV spectroscopy is an alternative possibility.

Table 7.19: Observed wavelength λ of an optical, magnetic dipole (M1) transition in Bi XV. Wavelength uncertainties are given as statistical uncertainty ($\Delta\lambda_{\mathrm{stat}}$) and a systematic uncertainty ($\Delta\lambda_{\mathrm{sys}}$). The initial ($\mathrm{L_i}$) and final ($\mathrm{L_f}$) levels are given, as well as the initial (J_i) and final (J_f) total angular momenta. Calculations with AMBiT include the calculated wavelength λ_A, the g factor of the initial (g_Ai) and final (g_Af) level, as well as transition rates A_{ki}. Reprinted from ref. [97].

$\mathrm{L_i} \rightarrow \mathrm{L_f}$	$J_\mathrm{i} \rightarrow J_\mathrm{f}$	$\lambda(\Delta\lambda_{\mathrm{stat}})(\Delta\lambda_{\mathrm{sys}})(\mathrm{nm})$	$\lambda_\mathrm{A}(\mathrm{nm})$	$A_{ki}(\frac{1}{\mathrm{s}})$	g_Ai	g_Af
$1 \rightarrow 0$	$^5/_2 \rightarrow {}^3/_2$	267.663420(53)(26)	265.9	572.1	1.200	0.800

Tm-like Bi XV The NIST data states $[\mathrm{Xe}]4\mathrm{f}^{14}5\mathrm{d}^2$ as the electronic ground state configuration of Bi XV [83]. This was confirmed with both, `FAC` and AMBiT.

Accordingly, the following parameters were used in our calculations:

`FAC`

Core configuration

$[\mathrm{Xe}]4\mathrm{f}^{14}$

Configuration used for radial optimisation

$5\mathrm{d}^1$

Shell configurations used for CI

$5\mathrm{d}^1$
$5\mathrm{f}^1$
$5\mathrm{g}^1$
$6\mathrm{s}^1$
$6\mathrm{p}^1$
$7\mathrm{s}^1$
$7\mathrm{p}^1$

AMBiT

Ground state configuration

$[\mathrm{Xe}]\,4f^{14} : 5\bar{d}^{0.4}5d^{0.6}$

Leading configurations

$5d^{1}$

Number of considered electron excitations: 2

Number of considered hole excitation: 0

A single transitions has been found in Bi XV, taking place inside the $[\mathrm{Xe}]4f^{14}5d^{1}$ configuration. It is a ground state transition with more details listed in table 7.14. No interesting optical ground state transitions are anticipated for this ion, calling for more precision measurements.

Chapter 8

Conclusion

"nec me pudet ut istos fateri nescire quod nesciam"
"And I am not ashamed, like they are, to admit that I do not know what I do not know"

—*Marcus Tullius Cicero* [98]

The current boundaries of high precision optical clock experiments concerning Physics Beyond the Standard Model (BSM) can be pushed further by utilising highly charged ions (HCIs) as clock ion in a quantum logic spectroscopy (QLS) scheme [42, 50, 51]. Numerous candidates, spanning many elements, are proposed for this purpose, particularly in the search for BSM [52, 56–58]. An extraordinary candidate for HCI experiments is $^{299}Th^{35+}$, whose low energetic nuclear transition may be leveraged by the so-called electronic bridge mechanism [54]. To do so, an electronic level determination of Th^{35+} akin to those featured in this work is necessary.

Laboratory developments At the time of the execution of the experiments for this thesis, however, thorium was not available for HCI spectroscopy. To lift this restriction, two laser injection (LI) systems and two optical paths to combine a spectrometer with different electron beam ion traps (EBITs) have been designed in the course of this work. Unfortunately, they could not be deployed for the data taken for this work, primarily due to time restrictions. The LI system designed for the Heidelberg compact EBITs (HC-EBITs) is established in the setup at the physikalische technische Bundesanstalt in Braunschweig [85]. The instance in Heidelberg is deployed at

the extreme ultraviolet EBIT (XUV-EBIT), which is thereby capable of supplying HCI from rare elements or isotopes to other experiments. The LI system designed for the free electron laser Hamburg EBITs (FLASH-EBITs), on the other hand, got altered slightly to accommodate the Heidelberg EBIT (HD-EBIT) and is currently implemented to perform spectroscopy on californium and thorium. The optical setup for the XUV-EBIT is defunct, as key parts will be repurposed for the setup at FLASH-EBIT. There, the components are waiting to be employed once the experimental schedule allows for it.

Progress of evaluation procedure To further prepare for the spectroscopy of Cs-like thorium Th^{35+}, Cs-like lead Pb^{27+} was chosen for the present work. To unambiguously determine the charge state, a line separation system based on non-negative matrix factorisation (NNMF) has been implemented on the convoluted and intricate spectra of 4f-subshells. No indications are preventing the application for similar-natured spectra, e.g. in the case of Th^{35+} and its neighbouring charge states.

Beyond that, an algorithm for correcting the thermal shift during the day cycle has been conceptualised, implemented and tested. It has proven robust and advantageous, reducing the uncertainty from a $0.069\,75(41)\,\mathrm{px\,h^{-1}}$ [91] uncompensated shift included in the measurements error budget to a typical statistical uncertainty between $\approx 0.025\,\mathrm{px\,h^{-1}}$ and $\approx 0.007\,\mathrm{px\,h^{-1}}$ on the determination of the shift for the present data. This variation is mainly caused by the diverse quality and quantity of available calibration lines on which the algorithm is based. This correction was implemented after the fact and is expected to yield even better results when taken into consideration while deciding on measurement sequences. This can be achieved, foremost but not limited to, by including additional calibration images between the ion and "dark" images to provide more data points to the fitting function and by choosing a low enough acquisition time.

Direct scientific contributions Multiple optical, magnetic dipole transitions, with their associated electronic levels, have been recorded during the course of this work. For lead, charge states from 21+ to 33+ were examined, covering the 4f-subshell from $4f^3$ in In-like Pb XXXIV to $4f^{13}$ in Pm-like Pb XXII, with the 5s-subshell filling up along the way. For bismuth, charge states from 9+ to 14+ were examined, covering the 5d-subshell from $5d^1$ in TM-like Bi XV to $5d^6$ in W-like Bi X.

Ground-state transitions have been found for ten of the twelve investigated lead ions and for all five investigated bismuth ions. An extensive

level structure reconstruction was possible for Pb XXXI and Pb XXXII. For Pb XXIX, Pb XXXIII, Bi XII, Bi XIII and Bi XIV, a partial reconstruction was possible, forming the groundwork for future analysis with the aid of vacuum ultraviolet (VUV) spectroscopy. Additionally, for Pb XXIX, Pb XXXIII and Bi XIV such transitions are predicted, requiring VUV spectra. For Bi XII and Bi XIII, further optical analysis in combination with VUV spectroscopy is necessary to determine whether suitable transitions are present.

Outlook The developed and mostly integrated changes to the laboratory setup introduced in this work mark important milestones in the spectroscopy of rare HCI, first and foremost, californium and thorium. Additionally, the algorithms newly implemented into the evaluation process both simplify the procedure and improve its outcome by reducing its uncertainty. The data contained in this work is a comprehensive assortment of intra-configuration hyperfine transitions in the 4f- and 5d-subshell of HCI, i.a., beneficial as an atomic structure calculation benchmark. Extending the recorded data by VUV not only increases this benefit immensely but also yields optical clock candidates, in all probability, potentially useful in the search for BSM.

Bibliography

[1] T. W. Hänsch, "Nobel Lecture: Passion for precision", Rev. Mod. Phys. **78**, 1297–1309 (2006) 10.1103/RevModPhys.78.1297.

[2] S. M. Faber and J. S. Gallagher, "Masses and mass-to-light ratios of galaxies", Annu. Rev. Astron. Astrophys. **17**, 135–187 (1979) 10.1146/annurev.aa.17.090179.001031.

[3] J. D. Bekenstein, "Fine-structure constant: Is it really a constant?", Phys. Rev. D **25**, 1527–1539 (1982) 10.1103/PhysRevD.25.1527.

[4] J. K. Webb, V. V. Flambaum, C. W. Churchill, M. J. Drinkwater, and J. D. Barrow, "Search for time variation of the fine structure constant", Phys. Rev. Lett. **82**, 884–887 (1999) 10.1103/PhysRevLett.82.884.

[5] J.-P. Uzan, "Varying Constants, Gravitation and Cosmology", Living Reviews in Relativity **14**, 2 (2011) 10.12942/lrr-2011-2.

[6] J. K. Webb et al., "Indications of a spatial variation of the fine structure constant", Phys. Rev. Lett. **107**, 191101 (2011) 10.1103/PhysRevLett.107.191101.

[7] J. C. Berengut, V. A. Dzuba, V. V. Flambaum, and A. Ong, "Highly charged ions with E1, M1, and E2 transitions within laser range", Phys. Rev. A **86**, 022517 (2012) 10.1103/PhysRevA.86.022517.

[8] M. S. Safronova et al., "Search for new physics with atoms and molecules", Rev. Mod. Phys. **90**, 025008 (2018) 10.1103/RevModPhys.90.025008.

[9] Y. Fukuda et al., "Evidence for oscillation of atmospheric neutrinos", Phys. Rev. Lett. **81**, 1562–1567 (1998) 10.1103/PhysRevLett.81.1562.

[10] H. Murayama, "The origin of neutrino mass", Phys. World **15**, 35–39 (2002) 10.1088/2058-7058/15/5/36.

[11] C. Weinheimer and K. Zuber, "Neutrino masses", Annalen der Physik **525**, 565–575 (2013) 10.1002/andp.201300063.

[12] N. F. Ramsey, "History of early atomic clocks", Metrologia **42**, S1 (2005) 10.1088/0026-1394/42/3/S01.

[13] A. Bauch, "The PTB primary clocks CS1 and CS2", Metrologia **42**, S43 (2005) 10.1088/0026-1394/42/3/S06.

[14] M. Lombardi, T. P. Heavner, and S. Jefferts, "NIST Primary frequency standards and the realization of the SI second", NCSLI Measure J. Meas. Sci. **2**, 74–89 (2007) 10.1080/19315775.2007.11721402.

[15] S. Weyers et al., "Advances in the accuracy, stability, and reliability of the PTB primary fountain clocks", Metrologia **55**, 789–805 (2018) 10.1088/1681-7575/aae008.

[16] T. P. Heavner et al., "First accuracy evaluation of NIST-F2", Metrologia **51**, 174–182 (2014) 10.1088/0026-1394/51/3/174.

[17] J. Guéna et al., "First international comparison of fountain primary frequency standards via a long distance optical fiber link", Metrologia **54**, 348 (2017) 10.1088/1681-7575/aa65fe.

[18] G. Santarelli et al., "Quantum Projection Noise in an atomic fountain: A high stability Cesium frequency standard", Phys. Rev. Lett. **82**, 4619–4622 (1999) 10.1103/PhysRevLett.82.4619.

[19] S. A. Diddams et al., "An optical clock based on a single trapped $^{199}Hg^{+}$ ion", Science **293**, 825–828 (2001) 10.1126/science.1061171.

[20] N. Huntemann, C. Sanner, B. Lipphardt, C. Tamm, and E. Peik, "Single-ion atomic clock with 3×10^{-18} systematic uncertainty", Phys. Rev. Lett. **116**, 063001 (2016) 10.1103/PhysRevLett.116.063001.

[21] S. L. Campbell et al., "A Fermi-degenerate three-dimensional optical lattice clock", Science **358**, 90–94 (2017) 10.1126/science.aam5538.

[22] S. M. Brewer et al., "$^{27}Al^{+}$ quantum-logic clock with a systematic uncertainty below 1×10^{-18}", Phys. Rev. Lett. **123**, 033201 (2019) 10.1103/PhysRevLett.123.033201.

[23] W. M. Itano et al., "Quantum projection noise: Population fluctuations in two-level systems", Phys. Rev. A **47**, 3554–3570 (1993) 10.1103/PhysRevA.47.3554.

[24] S. A. Diddams, J. C. Bergquist, S. R. Jefferts, and C. W. Oates, "Standards of time and frequency at the outset of the 21st century", Science **306**, 1318–1324 (2004) 10.1126/science.1102330.

[25] E. Peik, T. Schneider, and C. Tamm, "Laser frequency stabilization to a single ion", J. Phys. B **39**, 145 (2006) 10.1088/0953-4075/39/1/012.

[26] R. J. Rafac et al., "Sub-dekahertz ultraviolet spectroscopy of $^{199}Hg^{+}$", Phys. Rev. Lett. **85**, 2462–2465 (2000) 10.1103/PhysRevLett.85.2462.

[27] C. J. Sansonetti and J. Reader, "Spectrum and energy levels of singly-ionized Mercury (Hg II)", Phys. Scr. **63**, 219 (2001) 10.1238/Physica.Regular.063a00219.

[28] F. Diedrich and H. Walther, "Nonclassical radiation of a single stored ion", Phys. Rev. Lett. **58**, 203–206 (1987) 10.1103/PhysRevLett.58.203.

[29] W. H. Oskay et al., "Single-atom optical clock with high accuracy", Phys. Rev. Lett. **97**, 020801 (2006) 10.1103/PhysRevLett.97.020801.

[30] M. Chwalla et al., "Absolute frequency measurement of the $^{40}Ca^{+}$ $4s^2S_{1/2}-3d^2D_{5/2}$ clock transition", Phys. Rev. Lett. **102**, 023002 (2009) 10.1103/PhysRevLett.102.023002.

[31] N. Huntemann et al., "High-accuracy optical clock based on the octupole transition in $^{171}Yb^{+}$", Phys. Rev. Lett. **108**, 090801 (2012) 10.1103/PhysRevLett.108.090801.

[32] P. Dubé, A. A. Madej, Z. Zhou, and J. E. Bernard, "Evaluation of systematic shifts of the $^{88}Sr^{+}$ single-ion optical frequency standard at the 10^{-17} level", Phys. Rev. A **87**, 023806 (2013) 10.1103/PhysRevA.87.023806.

[33] N. Ohtsubo et al., "Optical clock based on a sympathetically-cooled indium ion", Hyperfine Interact. **240**, 10.1007/s10751-019-1585-8 (2019) 10.1007/s10751-019-1585-8.

[34] S. Friebel, C. D'Andrea, J. Walz, M. Weitz, and T. W. Hänsch, "CO_2 -laser optical lattice with cold Rubidium atoms", Phys. Rev. A **57**, R20–R23 (1998) 10.1103/PhysRevA.57.R20.

[35] H. Katori, "Spectroscopy of Strontium atoms in the Lamb-Dicke confinement", in Frequency Standards and Metrology, edited by P. Gill (2002), pp. 323–330, ISBN: 978-981-02-4911-3, 10.1142/9789812777713_0036.

[36] H. Katori, M. Takamoto, V. G. Pal'chikov, and V. D. Ovsiannikov, "Ultrastable optical clock with neutral atoms in an engineered light shift trap", Phys. Rev. Lett. **91**, 173005 (2003) 10.1103/PhysRevLett.91.173005.

[37] N. Hinkley et al., "An atomic clock with 10×10^{-18} instability", Science **341**, 1215–1218 (2013) 10.1126/science.1240420.

[38] S. Falke et al., "A Strontium lattice clock with 3×10^{-17} inaccuracy and its frequency", New J. Phys. **16**, 073023 (2014) 10.1088/1367-2630/16/7/073023.

[39] J. I. Cirac and P. Zoller, "Quantum computations with cold trapped ions", Phys. Rev. Lett. **74**, 4091–4094 (1995) 10.1103/PhysRevLett.74.4091.

[40] P. O. Schmidt et al., "Spectroscopy using quantum logic", Science **309**, 749–752 (2005) 10.1126/science.1114375.

[41] F. Wolf et al., "Non-destructive state detection for quantum logic spectroscopy of molecular ions", Nature **530**, 457–460 (2016) 10.1038/nature16513.

[42] P. Micke, "Quantum logic spectroscopy of highly charged ions", PhD Thesis (Gottfried Wilhelm Leibniz Universität, Hannover, 2020).

[43] J. Reichert et al., "Phase coherent vacuum-ultraviolet to radio frequency comparison with a mode-locked laser", Phys. Rev. Lett. **84**, 3232–3235 (2000) 10.1103/PhysRevLett.84.3232.

[44] S. A. Diddams et al., "Direct link between microwave and optical frequencies with a 300 THz femtosecond laser comb", Phys. Rev. Lett. **84**, 5102–5105 (2000) 10.1103/PhysRevLett.84.5102.

[45] E. Peik et al., "Limit on the present temporal variation of the fine structure constant", Phys. Rev. Lett. **93**, 170801 (2004) 10.1103/PhysRevLett.93.170801.

[46] T. Rosenband et al., "Frequency ratio of Al^+ and Hg^+ single-ion optical clocks, Metrology at the 17^{th} decimal place", Science **319**, 1808–1812 (2008) 10.1126/science.1154622.

[47] P. Wcisło et al., "Experimental constraint on dark matter detection with optical atomic clocks", Nat. Astron. **1**, 0009 (2016) 10.1038/s41550-016-0009.

[48] P. Wcisło et al., "New bounds on dark matter coupling from a global network of optical atomic clocks", Sci. Adv. **4**, eaau4869 (2018) 10.1126/sciadv.aau4869.

[49] N. Huntemann et al., "Improved limit on a temporal variation of m_p/m_e from comparisons of Yb^+ and Cs atomic clocks", Phys. Rev. Lett. **113**, 210802 (2014) 10.1103/PhysRevLett.113.210802.

[50] P. Micke et al., "Coherent laser spectroscopy of highly charged ions using quantum logic", Nature **578**, 60–65 (2020) 10.1038/s41586-020-1959-8.

[51] S. A. King et al., "An optical atomic clock based on a highly charged ion", Nature **611**, 43–47 (2022) 10.1038/s41586-022-05245-4.

[52] M. G. Kozlov, M. S. Safronova, J. R. Crespo López-Urrutia, and P. O. Schmidt, "Highly charged ions: Optical clocks and applications in fundamental physics", Rev. Mod. Phys. **90**, 045005 (2018) 10.1103/RevModPhys.90.045005.

[53] B. Seiferle et al., "Energy of the ^{229}Th nuclear clock transition", Nature **573**, 243–246 (2019) 10.1038/s41586-019-1533-4.

[54] P. V. Bilous et al., "Electronic bridge excitation in highly charged ^{229}Th ions", Phys. Rev. Lett. **124**, 192502 (2020) 10.1103/PhysRevLett.124.192502.

[55] K. Chabuda, I. D. Leroux, and R. Demkowicz-Dobrzański, "The quantum Allan variance", New J. Phys. **18**, 083035 (2016) 10.1088/1367-2630/18/8/083035.

[56] J. C. Berengut, V. A. Dzuba, and V. V. Flambaum, "Enhanced laboratory sensitivity to variation of the fine-structure constant using highly charged ions", Phys. Rev. Lett. **105**, 120801 (2010) 10.1103/PhysRevLett.105.120801.

[57] M. S. Safronova et al., "Atomic properties of Cd-like and Sn-like ions for the development of frequency standards and search for the variation of the fine-structure constant", Phys. Rev. A **90**, 052509 (2014) 10.1103/PhysRevA.90.052509.

[58] V. V. Flambaum, A. J. Geddes, and A. V. Viatkina, "Isotope shift, nonlinearity of King plots, and the search for new particles", Phys. Rev. A **97**, 032510 (2018) 10.1103/PhysRevA.97.032510.

[59] H. Bekker et al., "Detection of the 5p – 4f orbital crossing and its optical clock transition in Pr^{9+}", Nat. Commun. **10**, 5651 (2019) 10.1038/s41467-019-13406-9.

[60] N.-H. Rehbehn et al., "Narrow and ultranarrow transitions in highly charged Xe ions as probes of Fifth Forces", Phys. Rev. Lett. **131**, 161803 (2023) 10.1103/PhysRevLett.131.161803.

[61] J. C. Berengut, V. A. Dzuba, V. V. Flambaum, and A. Ong, "Optical transitions in highly charged californium ions with high sensitivity to variation of the fine-structure constant", Phys. Rev. Lett. **109**, 070802 (2012) 10.1103/PhysRevLett.109.070802.

[62] J. C. Berengut, C. Delaunay, A. Geddes, and Y. Soreq, "Generalized King linearity and new physics searches with isotope shifts", Phys. Rev. Res. **2**, 043444 (2020) 10.1103/PhysRevResearch.2.043444.

[63] M. Tanaka and Y. Yamamoto, "Relativistic effects in the search for new intra-atomic force with isotope shifts", Prog. Theor. Exp. Phys. **2020**, 10.1093/ptep/ptaa121 (2020) 10.1093/ptep/ptaa121.

[64] H. S. Dhindsa, V. J. Marton, and G. W. F. Drake, "Search for Light Bosons with King and Second-King Plots Optimized for Lithium Ions", Phys. Part. Nuclei **53**, 800–804 (2022) 10.1134/S1063779622040037.

[65] N.-H. Rehbehn et al., "Sensitivity to new physics of isotope-shift studies using the coronal lines of highly charged calcium ions", Phys. Rev. A **103**, L040801 (2021) 10.1103/PhysRevA.103.L040801.

[66] D. Greenwood, *The nature of science and other essays*, Essay and general literature index reprint series (Kennikat Press, Port Washington N.Y., 1971, 1959), xii, 95, ISBN: 9780804614085.

[67] S. Kühn et al., "New measurement resolves key astrophysical Fe XVII oscillator strength problem", Phys. Rev. Lett. **129**, 245001 (2022) 10.1103/PhysRevLett.129.245001.

[68] C. Shah et al., "Natural-linewidth measurements of the 3C and 3D soft-x-ray transitions in Ni XIX", Phys. Rev. A **109**, 063108 (2024) 10.1103/PhysRevA.109.063108.

[69] J. C. Berengut, V. A. Dzuba, V. V. Flambaum, and A. Ong, "Electron-hole transitions in multiply charged ions for precision laser spectroscopy and searching for variations in α", Phys. Rev. Lett. **106**, 210802 (2011) 10.1103/PhysRevLett.106.210802.

[70] W. Lotz, "Electron-impact ionization cross-sections and ionization rate coefficients for atoms and ions from hydrogen to calcium", Z. Phys. **216**, 241–247 (1968) 10.1007/BF01392963.

[71] A. K. F. Haque et al., "Generalized Kolbenstvedt model for electron impact ionization of the K-, L- and M-shell ions", Phys. Scr. **81**, 045301 (2010) 10.1088/0031-8949/81/04/045301.

[72] Y. S. Kim and R. H. Pratt, "Direct radiative recombination of electrons with atomic ions: Cross sections and rate coefficients", Phys. Rev. A **27**, 2913–2924 (1983) 10.1103/PhysRevA.27.2913.

[73] A. Müller and E. Salzborn, "Scaling of cross sections for multiple electron transfer to highly charged ions colliding with atoms and molecules", Phys. Lett. B **62**, 391–394 (1977) 10.1016/0375-9601(77)90672-7.

[74] V. I. Fisher et al., "Electron-impact-excitation cross sections of hydrogenlike ions", Phys. Rev. A **55**, 329–334 (1997) 10.1103/PhysRevA.55.329.

[75] B. M. Penetrante, J. N. Bardsley, D. DeWitt, M. Clark, and D. Schneider, "Evolution of ion-charge-state distributions in an electron-beam ion trap", Phys. Rev. A **43**, 4861–4872 (1991) 10.1103/PhysRevA.43.4861.

[76] M. K. Rosner, "Production and preparation of highly charged ions for re-trapping in ultra-cold environments", Master Thesis (Ruprecht-Karls-Universität, Heidelberg, 2019).

[77] M. F. Gu, "The flexible atomic code", Can. J. Phys. **86**, 675–689 (2008) 10.1139/p07-197.

[78] E. V. Kahl and J. C. Berengut, "Ambit: a programme for high-precision relativistic atomic structure calculations", Comput. Phys. Commun. **238**, 232–243 (2019) 10.1016/j.cpc.2018.12.014.

[79] S. Borowski, *The origin and popular use of Occam's razor*, edited by American Association for the Advancement of Science, (2012) https://www.aaas.org/taxonomy/term/10/origin-and-popular-use-occams-razor (visited on 08/08/2024).

[80] P. Micke et al., "The Heidelberg compact electron beam ion traps", Rev. Sci. Instrum. **89**, 063109 (2018) 10.1063/1.5026961.

[81] Bundesrat, *Bericht über die 112. Sitzung des Deutschen Bundestages*, edited by Bonner Universitäts-Buchdruckerei, 1974.

[82] C. Schweiger et al., "Production of highly charged ions of rare species by laser-induced desorption inside an electron beam ion trap", Rev. Sci. Instrum. **90**, 123201 (2019) 10.1063/1.5128331.

[83] A. Kramida, Y. Ralchenko, and R. Joseph, *NIST Atomic Spectra Database (version 5.11)*, (2024) 10.18434/T4W30F, https://physics.nist.gov/asd (visited on 02/12/2024).

[84] M. A. Levine, R. E. Marrs, J. R. Henderson, D. A. Knapp, and M. B. Schneider, "The Electron Beam Ion Trap: A New Instrument for Atomic Physics Measurements", Phys. Scr. **1988**, 157 (1988) 10.1088/0031-8949/1988/T22/024.

[85] A. Wilzewski, "Isotope shift measurements of highly charged calcium", PhD Thesis (Gottfried Wilhelm Leibniz Universität, Hannover, 2024).

[86] T. M. Martin, *The end games* (Harper 360, New York, 2014), 15 pp., ISBN: 978-0062201812.

[87] M. A. Blessenohl, "Fine-structure investigations in highly charged ions using spectroscopy in the vacuum ultraviolet regime", Phd Thesis (Ruprecht-Karls-Universität, Heidelberg, 2020).

[88] H. Bekker, "Optical and EUV spectroscopy of highly charged ions near the 4f – 5s level crossing", PhD Thesis (Ruprecht-Karls-Universität, Heidelberg, 2016).

[89] McPherson, *Model 2062, High resolution spectrometer*, (2024) https://www.mcphersoninc.com/pdf/2062.pdf (visited on 08/04/2021).

[90] Thorlabs, *Reflective holographic gratings*, (2024) https://www.thorlabs.com/newgrouppage9.cfm?objectgroup_id=25 (visited on 08/05/2024).

[91] N.-H. Rehbehn, "Measurement of highly charged Ca and Xe ions and their sensitivity to a hypothetical fifth force beyond the Standard Model", PhD Thesis (Ruprecht-Karls-Universität, Heidelberg, 2023).

[92] Oxford Instruments, *Newton CCD, Spectroscopy at pace*, (2024) https://andor.oxinst.com/assets/uploads/products/andor/documents/andor-newton-ccd-specifications.pdf (visited on 08/04/2024).

[93] N. Bohr, "The unity of human knowledge", Am. J. Health-Syst. Pharm. **17**, 694–697 (1960) 10.1093/ajhp/17.11.694.

[94] W. Pych, "A fast algorithm for cosmic–ray removal from single images", Publ. Astron. Soc. Pac. **116**, 148–153 (2004) 10.1086/381786.

[95] MathWorks, *Nonnegative matrix factorization, Matlab documentation*, (2024) https://de.mathworks.com/help/stats/nnmf.html (visited on 08/08/2024).

[96] J. W. von Goethe and C. T. Brooks, *Faust: a tragedy [part 1], Translated from the German of Goethe* (Juliet Sutherland, Charles Bidwell and the PG Online Distributed Proofreading Team, 1808).

[97] M. K. Rosner, N.-H. Rehbehn, and J. R. Crespo López-Urrutia, "Experimental and theoretical Ritz-Rydberg analysis of the electronic structure ofhighly charged ions of lead and bismuth by optical spectroscopy", J. Phys. B **57**, 055001 (2024) 10.1088/1361-6455/ad285f.

[98] M. T. Cicero, *Tusculanae disputationes* (45 BC).

Appendix A

Acknowledgements

Lieselotte Rosner, my wife, for tolerating the stressful periods during my doctorate, encouraging and guiding me most patiently

Ferdinand Rosner, my son, for all the exhilarant disruptions after long days of high-focused work

José Crespo, my supervisor, for seven years of guidance and support that enabled my advancement from student towards doctoral candidate

Hendrik Bekker & Nils Rehbehn, my colleagues, whose support, especially with the optical spectroscopy, has proven invaluable

Christoph Schweiger & Alexander Wilzewski, external collaborators, for the crucial cooperation at the laser ablation systems

Alexander Ryabtsev for our scientific exchange, including preliminary `COWAN` calculations

Maximilian Winterer, our bachelor student, for helping to set up the old spectrometer

The EBIT-Group, whose fruitful discussions and delightful cake breaks progressed my research immensely

Bettina Mörk, the designer for transforming new experimental ideas into a tangible blueprint

The workshops, without whom only thought experiments could have been conducted

The Kaiser workshop in particular, for creatively solving last-minute problems on experimental assemblies

Presentation of the measurement data

In this section, the data files saved for the measurements are presented. For this purpose, the text, as occurring in a file name or as text in a file, is stylised in a `monospaced font`. Place-holder variables in file names, giving more information about the individual file, are additionally formatted as SMALL CAPS, and explained afterwards.

On each measurement day, a `YYMMDD_TIMEData.dat` is created, where `YY` indicates the year 20`YY`, `MM` the month and `DD` the day the file refers to. An example can be found in appendix A.1. After the header, it contains a new line for every measurement taken on that day. A number `#Meas` is assigned to each measurement. Timestamps for the beginning `t_ebit` and end `t_data` of the acquisition are given. The `HHMMSS` format is used to indicate `HH:MM:SS` in the 24-hour notation. These timestamps are also used in the associated image data (`t_data`) and EBIT (`t_ebit`) setting files. And obsolete `t_wave` used to point to another obsolete file; it now gives `0` but is retained so old code is still compatible with newer files. Next, the settings of the spectrometer are given. `wavelength` is the set wavelength, `acqu_time` the acquisition time in s, `lens_pos` the position of the moveable lens inside the periscope in mm and `grating` is the grove density of the installed grating in mm^{-1}. The main EBIT parameters follow. `Cathode`, `Anode`, `Focus`, `ALLDTS`, `DT9` give the voltage of the corresponding power supply in V. `ALLDTS` raises the reference ground of all drift tube (DT) power supplies, the others are directly connected to the electrode. `CollCurrent` is the collector current measured at `t_ebit` in mA. `FileComments` are user notes as given in the spectrometer control program.

More detailed information on the experimental parameters is found in the `YYMMDD_HHMMSS_EBITSettings.dat` file, where `YYMMDD` is the day as above and `HHMMSS` the time given in the `t_ebit` column. It features a list of parameters and the corresponding values. An example can be found in appendix A.2, explaining the values in table A.1. These values are taken before

the acquisitions are started.

Once the acquisition is finished, the corresponding new line in the TIMEData file is added, and the spectroscopic image is saved. These images are named YYMMDD_HHMMSS_[calib_]GRATINGgrating_FILECOMMENTS.dat. YYMMDD is the day and HHMMSS the time given in the t_data column. [calib_] indicates that the token calib_ is added for calibration images, and omitted otherwise. GRATING is the grove density and FILECOMMENTS are the user notes, as in the TIMEData file. It contains the pixels counts as numerical values, columns separated by spaces, rows in new lines. Examples of a raw image can be seen in figs. 6.1 and 6.3.

Table A.1: Content of a EBIT settings file. Identifier as given in the file. The quantities are a mix of measured (pressures p, current I, temperature t) and set values (voltage U, position x). The "allDT" value raises the floating ground of the DTs power supplies, i.e. $\varphi_{\mathrm{DT}x} = U_{\mathrm{DT}x} + U_{\mathrm{allDT}}, x \in \mathbb{N}, 1 \geq x \geq 9$. DT9 is the central drift tube. Injection 1 is the reservoir away from the EBIT; at injection 2, the injection beam forms. Exemplary values can be found in appendix A.2.

Identifier	quantity	unit
`HDEBIT:PRESSURE:MAG.VAL`	p_{magnet}	mbar
`HDEBIT:PRESSURE:GUN.VAL`	p_{gun}	mbar
`HDEBIT:PRESSURE:COLL.VAL`	$p_{\mathrm{collector}}$	mbar
`HDEBIT:PRESSURE:INJ1.VAL`	$p_{\mathrm{injection1}}$	mbar
`HDEBIT:PRESSURE:INJ2.VAL`	$p_{\mathrm{injection2}}$	mbar
`HDEBIT:GUN:CATHODE:VOLTAGE.VAL`	U_{cathode}	V
`HDEBIT:GUN:ANODE:VOLTAGE.VAL`	U_{anode}	V
`HDEBIT:GUN:FOCUS:VOLTAGE.VAL`	U_{focus}	V
`HDEBIT:GUN:SUPPRESSOR:VOLTAGE.VAL`	$U_{\mathrm{suppressor}}$	V
`HDEBIT:GUN:EXTRACTOR:VOLTAGE.VAL`	$U_{\mathrm{extractor}}$	V
`HDEBIT:DT:DT1.VAL`	U_{DT1}	V
`HDEBIT:DT:DT2.VAL`	U_{DT2}	V
`HDEBIT:DT:DT3.VAL`	U_{DT3}	V
`HDEBIT:DT:DT4.VAL`	U_{DT4}	V
`HDEBIT:DT:DT9.VAL`	U_{DT9}	V
`HDEBIT:DT:DT5.VAL`	U_{DT5}	V
`HDEBIT:DT:DT6.VAL`	U_{DT6}	V
`HDEBIT:DT:DT7.VAL`	U_{DT7}	V
`HDEBIT:DT:DT8.VAL`	U_{DT8}	V
`HDEBIT:DT:TRUMPET.VAL`	U_{trumpet}	V
`HDEBIT:DT:ALLDTS.VAL`	U_{allDT}	V
`HDEBIT:GUN:COLLECTOR:CURRENT:MON.VAL`	$I_{\mathrm{collector}}$	mA
`HDEBIT:GUN:ANODE:CURRENT:MON.VAL`	I_{anode}	µA
`HDEBIT:GUN:SUPRESSOR:CURRENT:MON.VAL`	$I_{\mathrm{suppressor}}$	µA
`HDEBIT:GUN:EXTRACTOR:CURRENT:MON.VAL`	$I_{\mathrm{extractor}}$	µA
`Lens position:`	x_{lens}	mm
`Camera Temperature:`	t_{CCD}	°C

A.1 TIMEData

```
#Meas t_data t_ebit t_wave wavelength acqu_time lens_pos grating Cathode Anode Focus ALLDTS DT9 CollCurrent FileComments
1 144653 143151 0 282.75 900.0 3.63 3600 -1335.0 400.0 -3007.0 0.0 25.0 0.2509022881873535
2 154017 153835 0 343.40 100.0 17.94 3600 -1335.0 400.0 -500.0 0.0 25.0 51.7403916591106
3 161114 154111 0 343.40 1800.0 17.94 3600 -1335.0 400.0 -500.0 0.0 25.0 51.82147746598296
4 161713 161531 0 343.40 100.0 17.94 3600 -1335.0 400.0 -500.0 0.0 25.0 52.32420946840558
5 162244 162102 0 343.40 100.0 17.95 3600 -1335.0 400.0 -6.8246973956592 0.0 25.0 87.53166624272149
6 165257 162255 0 343.40 1800.0 17.95 3600 -1335.0 400.0 -6.8246973956592 0.0 25.0 87.75870649575926
7 173402 173220 0 343.40 100.0 17.95 3600 -1335.0 400.0 0.0 0.0 25.0 88.42361009382806 energy_optim
8 174017 173514 0 343.40 300.0 17.94 3600 -1305.0 400.0 1.2989477775868892 0.0 25.0 85.94238447088816 energy_optim
9 174522 174020 0 343.40 300.0 17.94 3600 -1315.0 400.0 -1.3813447474757368 0.0 25.0 86.78567683974457 energy_optim
10 175027 174525 0 343.40 300.0 17.94 3600 -1325.0 400.0 -4.089226471891095 0.0 25.0 87.49923192085734 energy_optim
11 175532 175030 0 343.40 300.0 17.94 3600 -1335.0 400.0 -6.8246973956592 0.0 25.0 88.13170119713159 energy_optim
12 180037 175535 0 343.40 300.0 17.94 3600 -1345.0 400.0 -9.587757518780066 0.0 25.0 88.65065034678172 energy_optim
13 180542 180040 0 343.40 300.0 17.94 3600 -1355.0 400.0 -12.378406841253693 0.0 25.0 89.49394271478404 energy_optim
14 183806 180804 0 343.40 1800.0 17.94 3600 -1335.0 400.0 -6.8246973956592 0.0 25.0 88.3749586110486 half_hour_test
15 185416 183914 0 282.75 900.0 3.61 3600 -1335.0 400.0 -6.8246973956592 0.0 25.0 87.90466094413003 half_hour_test
16 212421 185419 0 282.75 9000.0 3.61 3600 -1335.0 400.0 -6.8246973956592 0.0 25.0 88.73173615141587 half_hour_test
17 235431 212429 0 282.75 9000.0 3.61 3600 -1335.0 400.0 -6.8246973956592 0.0 225.0 88.82903911696765 half_hour_test
```

A.2 EBITSettings

```
HDEBIT:PRESSURE:MAG.VAL 5.912e-10
HDEBIT:PRESSURE:GUN.VAL 1.203e-10
HDEBIT:PRESSURE:COLL.VAL 3.056e-10
HDEBIT:PRESSURE:INJ1.VAL 3.41e-08
HDEBIT:PRESSURE:INJ2.VAL 2.051e-09
HDEBIT:GUN:CATHODE:VOLTAGE.VAL -1335.0
HDEBIT:GUN:ANODE:VOLTAGE.VAL 400.0
HDEBIT:GUN:FOCUS:VOLTAGE.VAL -6.8246973956592
HDEBIT:GUN:SUPPRESSOR:VOLTAGE.VAL -200.0
HDEBIT:GUN:EXTRACTOR:VOLTAGE.VAL -2000.0
HDEBIT:DT:DT1.VAL 10.0
HDEBIT:DT:DT2.VAL 25.0
HDEBIT:DT:DT3.VAL 50.0
HDEBIT:DT:DT4.VAL 75.0
HDEBIT:DT:DT9.VAL 25.0
HDEBIT:DT:DT5.VAL 75.0
HDEBIT:DT:DT6.VAL 50.0
HDEBIT:DT:DT7.VAL 25.0
HDEBIT:DT:DT8.VAL 10.0
HDEBIT:DT:TRUMPET.VAL -200.0
HDEBIT:DT:ALLDTS.VAL 0.0
HDEBIT:GUN:COLLECTOR:CURRENT:MON.VAL 88.68308466864185
HDEBIT:GUN:ANODE:CURRENT:MON.VAL 0.20727679584105294
HDEBIT:GUN:SUPRESSOR:CURRENT:MON.VAL 0.031862087439280234
HDEBIT:GUN:EXTRACTOR:CURRENT:MON.VAL 0.006109098204831729
Lens position: 15.84
Camera Temperature: -78
```

A.3 Measured line overview

All lines measured in the course of this work are listed here:

- Table A.2: Pb XXII to Pb XXXI
- Table A.3: Pb XXXII to Pb XXXIV
- Table A.4: Bi X to Bi XV

Table A.2: Observed wavelength λ of a optical, magnetic dipole (M1) transition in Pb XXII to Pb XXXI. Wavelength uncertainties are given as statistical uncertainty ($\Delta\lambda_{\mathrm{stat}}$) and a systematic uncertainty ($\Delta\lambda_{\mathrm{sys}}$). The initial ($\mathrm{L_i}$) and final ($\mathrm{L_f}$) levels are given, as well as the initial (J_i) and final (J_f) total angular momenta. Calculations with AMBiT include the calculated wavelength λ_A, the g factor of the initial (g_Ai) and final (g_Af) level. Relative intensities I_F from the CRM are given. Reprinted from ref. [97]

Ion	$\mathrm{L_i} \to \mathrm{L_f}$	$J_\mathrm{i} \to J_\mathrm{f}$	$\lambda(\Delta\lambda_{\mathrm{stat}})(\Delta\lambda_{\mathrm{sys}})$(nm)	λ_A(nm)	I_F	g_Ai	g_Af
Pb XXII	$1 \to 0$	$^5/_2 \to {}^7/_2$	243.64949(154)(8)	244	3.18	0.86	1.14
Pb XXIII p	$1 \to 0$	$3 \to 4$	256.86064(107)(8)	214	1.13	1.04	1.25
Pb XXIV	$1 \to 0$	$^5/_2 \to {}^7/_2$	239.70162(150)(8)	242	1.55	0.86	1.14
Pb XXV	$3 \to 1$	$4 \to 4$	252.17575(25)(8)	258	0.91	1.01	1.14
Pb XXV	$2 \to 0$	$5 \to 6$	252.77713(23)(8)	256	1.62	1.03	1.16
Pb XXVI	$1 \to 0$	$^{13}/_2 \to {}^{15}/_2$	264.88477(147)(8)	269	2.86	1.10	1.19
Pb XXVII	$1 \to 0$	$7 \to 8$	271.54179(13)(8)	277	5.39	1.16	1.22
Pb XXVIII	$1 \to 0$	$^{13}/_2 \to {}^{15}/_2$	309.92900(56)(7)	318	5.38	1.25	1.28
Pb XXIX	$3 \to 0$	$5 \to 6$	413.96783(45)(17)	433	4.68	1.45	1.43
Pb XXIX	$4 \to 2$	$3 \to 4$	523.48424(47)(16)	578	1.26	1.44	1.41
Pb XXIX	$6 \to 5$	$9 \to 10$	733.89990(124)(13)	689	1.89	1.13	1.15
Pb XXXI	$1 \to 0$	$1 \to 0$	392.65739(26)(6)	427	18.73	1.50	0
Pb XXXI	$2 \to 1$	$2 \to 1$	524.68818(101)(16)	543	10.42	1.47	1.50
Pb XXXI	$3 \to 2$	$3 \to 2$	737.13765(31)(13)	736	3.74	1.45	1.47

p: preliminary identification

Table A.3: Observed wavelength λ of a optical, magnetic dipole (M1) transition in Pb XXXII to Pb XXXIV. Wavelength uncertainties are given as statistical uncertainty ($\Delta\lambda_{\mathrm{stat}}$) and a systematic uncertainty ($\Delta\lambda_{\mathrm{sys}}$). The initial ($\mathrm{L_i}$) and final ($\mathrm{L_f}$) levels are given, as well as the initial (J_i) and final (J_f) total angular momenta. Calculations with AMBiT include the calculated wavelength λ_A, the g factor of the initial (g_{Ai}) and final (g_{Af}) level. Relative intensities I_F from the CRM are given. Reprinted from ref. [97]

Ion	$\mathrm{L_i} \to \mathrm{L_f}$	$J_\mathrm{i} \to J_\mathrm{f}$	$\lambda(\Delta\lambda_{\mathrm{stat}})(\Delta\lambda_{\mathrm{sys}})$(nm)	λ_A(nm)	I_F	g_{Ai}	g_{Af}
Pb XXXII	$1 \to 0$	$^7/_2 \to {}^5/_2$	343.16795(78)(7)	364	7.10	0.89	0.53
Pb XXXII	$3 \to 1$	$^9/_2 \to {}^7/_2$	490.49287(18)(16)	496	2.22	1.06	0.89
Pb XXXII	$5 \to 1$	$^7/_2 \to {}^7/_2$	283.75284(55)(8)	272	0.87	1.27	0.89
Pb XXXII	$5 \to 2$	$^7/_2 \to {}^5/_2$	434.81120(60)(17)	443	1.64	1.27	1.02
Pb XXXII	$4 \to 3$	$^{11}/_2 \to {}^9/_2$	771.89599(157)(13)	741	0.64	1.13	1.06
Pb XXXII	$6 \to 5$	$^9/_2 \to {}^7/_2$	626.21185(87)(15)	597	0.59	1.30	1.27
Pb XXXIII	$1 \to 0$	$5 \to 4$	284.88000(61)(8)	296	2.55	0.92	0.68
Pb XXXIII	$3 \to 1$	$6 \to 5$	442.31591(51)(17)	437	0.78	1.03	0.92
Pb XXXIII	$4 \to 2$	$1 \to 2$	381.97750(24)(6)	425	2.21	0.17	0.91
Pb XXXIII	$6 \to 2$	$3 \to 2$	277.931099(36)(8)	296	1.14	1.07	0.91
Pb XXXIII	$7 \to 2$	$2 \to 2$	258.09230(49)(8)	264	2.17	0.66	0.91
Pb XXXIII	$8 \to 5$	$5 \to 4$	301.21601(51)(8)	292	0.33	1.16	1.00
Pb XXXIV	$3 \to 2$	$^5/_2 \to {}^3/_2$	409.47995(59)(17)	396	5.94	0.82	0.71

p: preliminary identification

Table A.4: Observed wavelength λ of optical, magnetic dipole (M1) transitions in Bi X to Bi XV. Wavelength uncertainties are given as statistical uncertainty ($\Delta\lambda_{\mathrm{stat}}$) and a systematic uncertainty ($\Delta\lambda_{\mathrm{sys}}$). The initial ($\mathrm{L_i}$) and final ($\mathrm{L_f}$) levels are given, as well as the initial (J_i) and final (J_f) total angular momenta. Calculations with AMBiT include the calculated wavelength λ_A, the g factor of the initial (g_Ai) and final (g_Af) level, as well as transition rates $A_{ki}(\mathrm{s}^{-1})$. Reprinted from ref. [97]

Ion	$\mathrm{L_i} \to \mathrm{L_f}$	$J_\mathrm{i} \to J_\mathrm{f}$	$\lambda(\Delta\lambda_{\mathrm{stat}})(\Delta\lambda_{\mathrm{sys}})$(nm)	λ_A(nm)	$A_{ki}(\mathrm{s}^{-1})$	g_Ai	g_Af
Bi X	$2 \to 0$ p	$4 \to 4$	356.18(8)(12)	349.5	364.7	1.104	1.377
Bi X	$1 \to 0$ p	$3 \to 4$	491.93805(92)(4)	503.7	211.0	1.439	1.377
Bi XI	$1 \to 0$	$5/2 \to 5/2$	455.8462(13)(3)	435.7	307.8	1.145	1.733
Bi XI	$2 \to 0$ p	$3/2 \to 5/2$	253.071(69)(26)	258.1	625.8	1.280	1.733
Bi XII	$5 \to 3$	$3 \to 3$	433.40007(43)(24)	425.0	237.9	1.010	1.320
Bi XII	$1 \to 0$	$1 \to 0$	469.91626(17)(3)	489.6	271.8	1.498	0
Bi XII	$4 \to 2$	$4 \to 4$	474.4117(24)(5)	490.2	265.2	1.143	1.162
Bi XIII	$2 \to 0$	$3/2 \to 3/2$	298.5070(14)(1)	292.9	391.5	1.298	0.595
Bi XIII	$4 \to 2$ p	$5/2 \to 3/2$	365.893(38)(41)	376.4	143.9	1.471	1.298
Bi XIII	$6 \to 4$ p	$5/2 \to 5/2$	376.54(5)(11)	371.1	194.1	1.060	1.471
Bi XIII	$5 \to 3$ p	$9/2 \to 9/2$	379.40(6)(12)	368.9	337.9	1.133	1.100
Bi XIII	$1 \to 0$	$5/2 \to 3/2$	411.56092(35)(6)	420.9	414.9	1.046	0.595
Bi XIV	$7 \to 3$	$2 \to 2$	263.0410(61)(8)	261.0	669.7	1.231	1.197
Bi XIV	$7 \to 5$	$2 \to 1$	292.43047(83)(37)	288.6	274.4	1.231	1.500
Bi XIV	$2 \to 0$	$3 \to 2$	312.8075(21)(2)	313.6	674.5	1.083	0.738
Bi XIV	$6 \to 4$	$4 \to 4$	348.058773(101)(50)	345.3	202.2	1.112	1.138
Bi XIV	$5 \to 1$	$1 \to 0$	425.91653(50)(1)	436.7	178.9	1.500	0
Bi XIV	$4 \to 2$	$4 \to 3$	653.87821(34)(3)	627.8	44.9	1.214	1.273
Bi XV	$1 \to 0$	$5/2 \to 3/2$	267.663420(53)(26)	265.9	572.1	1.200	0.800

p: preliminary identification